Exploring Neural Cell Isolation Techniques in Neuroscience Research: Methods and Applications

Article Collection

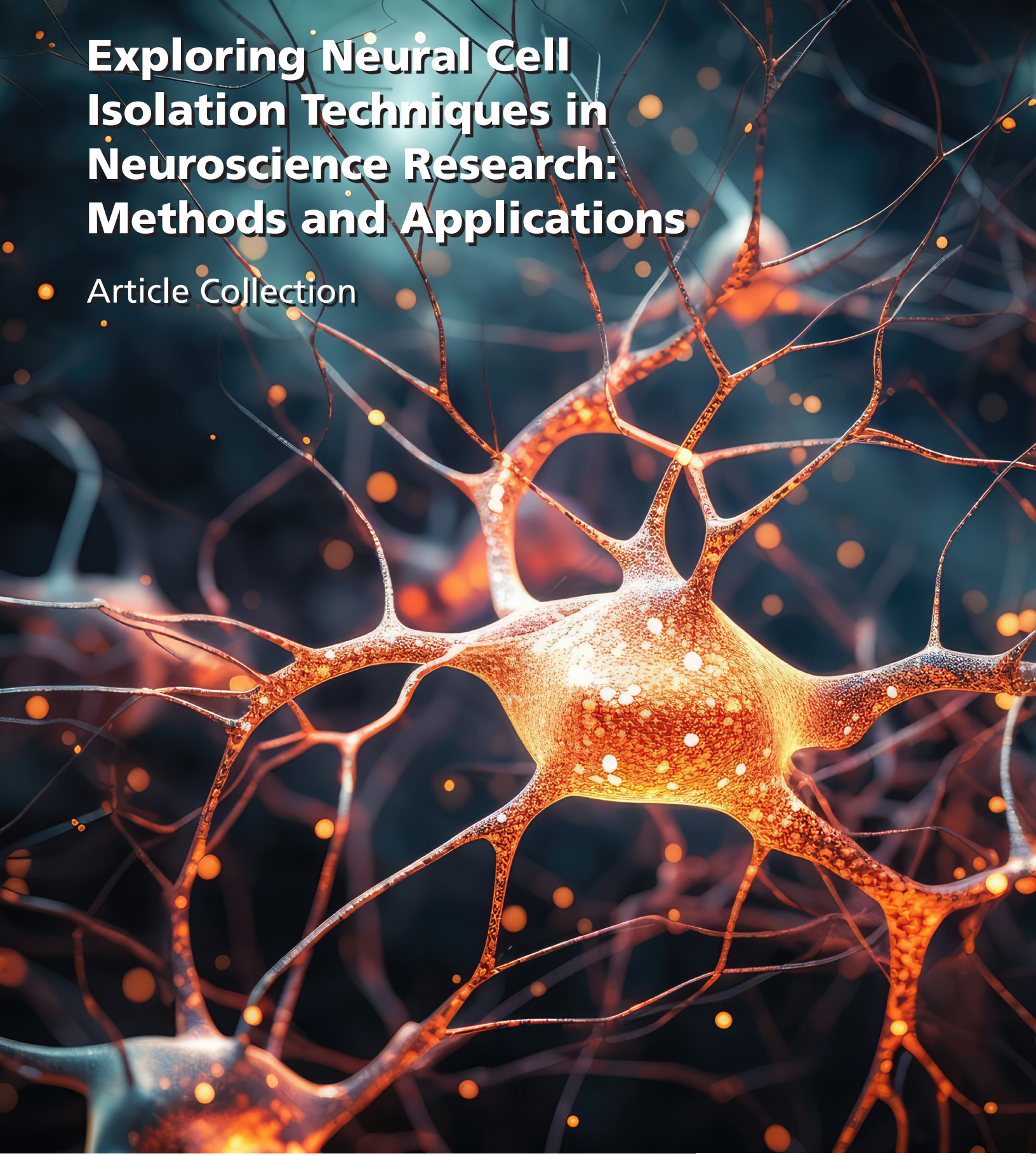

Sponsored by:

Miltenyi Biotec

WILEY

Gentle cell sorting of neural cells

Microchip-based cell sorting in a closed system: MACSQuant® Tyto® Cell Sorter

- **Microchip-based gentle cell sorting safeguards cell viability and functionality**
- **Cell sorting takes place exclusively in a single-use and closed cartridge**
- **Fast and easy sort setup coupled with an intuitive software facilitate daily operation**
- **Engineered for operator and sample safety with no aerosol or droplet formation**

▸ **miltenyibiotec.com/tyto**

Miltenyi Biotec B.V. & Co. KG | Friedrich-Ebert-Straße 68 | 51429 Bergisch Gladbach | Germany
Phone +49 2204 8306-0 | Fax +49 2204 85197 | macsde@miltenyi.com | **www.miltenyibiotec.com**

Miltenyi Biotec provides products and services worldwide.
Visit **www.miltenyibiotec.com/local** to find your nearest Miltenyi Biotec contact.

Miltenyi Biotec

Contents

Imprint

©John Wiley & Sons, Inc.
111 River Street,
Hoboken, NJ 07030-5774
USA
Contact: Customer Service

Editor:
Róisín Murtagh

Senior Account Manager:
Stefanie Krauth

Miltenyi Biotec
https://www.miltenylbiotec.com/

Cover: ©2023 Adobe Stock

Introduction

Neural cell isolation, the process of selectively extracting neurons or neural cells from a mixed cell population, is an important technique in neuroscience research as it allows scientists to study and analyze specific cell types in the nervous system.

Various methods exist for isolating neural cells, each with its advantages and limitations. One commonly used method is enzymatic dissociation, which involves treating the neural tissue with enzymes like trypsin or papain to break down the extracellular matrix and dissociate the cells. This method is useful for obtaining a single-cell suspension from brain or spinal cord tissues.

Magnetic-activated cell sorting (MACS) is a popular method for neural cell isolation. This technique involves attaching magnetic beads to specific cell surface markers or antibodies and then using a magnetic field to separate the labeled cells from the rest of the sample. MACS is relatively simple and efficient, making it a preferred method for isolating neural cells in large quantities.

Another technique is fluorescence-activated cell sorting (FACS), which utilizes fluorescently labeled antibodies or dyes to tag specific cell types. The labeled cells can then be sorted and collected using a flow cytometer based on their fluorescence properties. FACS provides high specificity and purity in isolating neural cells, but it requires prior knowledge of specific markers for the targeted cell type.

In addition to FACS, researchers may also utilize microfluidic devices for neural cell isolation. Compared to conventional droplet cell sorting devices, microfluidic-based cell sorters with gentle sorting technology can yield the highest number of viable and functional cells. These devices utilize a combination of physical and chemical methods to isolate and manipulate cells at a microscopic level. These devices offer precise control over flow rates, cell trapping, and sorting, making them a promising technique for high-throughput and single-cell analysis.

The isolated neural cells can be used for various downstream applications, including gene expression analysis, electrophysiology studies, and cell culture experiments. By studying specific populations of neural cells, researchers can gain insights into the functions, properties, and interactions of different cell types within the nervous system.

Neural cell isolation is particularly crucial in the field of stem cell research. Neural stem cells (NSCs) are multipotent cells that can differentiate into different neural

cell types, including neurons, astrocytes, and oligodendrocytes. By isolating and culturing NSCs, researchers can study their differentiation potential and use them to generate specific neural cell types for transplantation or drug screening purposes.

Overall, the ability to isolate and study neural cells individually opens new avenues for understanding the complex mechanisms of the nervous system and developing potential therapies for neurological disorders.

This article collection begins with a study by Holt, L.M. *et al.* [1] on the development of a cost-effective method to isolate specific cell types, such as neurons, astrocytes, and microglia, from a mixed sample using magnetic beads attached to cell-type specific antibodies. This technique has been used to isolate astrocytes at different stages of development and in mature adults. Additionally, the article highlights the application of this method in novel astrocyte and astrocyte/neuron co-culture experiments.

Next, Vana, N.S. *et al.* [2] aimed to investigate the role of synaptic signaling in oligodendrocyte precursor cells (OPCs) during development. The researchers compared the functional and molecular characteristics of highly proliferative and migratory OPCs in the embryonic brain in mice at E18.5 with postnatal OPCs. They found that embryonic OPCs shared certain characteristics, such as expression of voltage-gated ion channels and dendritic morphology, with postnatal OPCs, but did not exhibit functional synaptic currents. Transcriptomic profiling revealed a limited presence of genes related to postsynaptic signaling and synaptogenic cell adhesion molecules in embryonic OPCs compared to postnatal OPCs. Single-cell transcriptomics further demonstrated that embryonic OPCs without synaptic input formed distinct clusters separate from postnatal OPCs, resembling early progenitors. Additionally, synaptic genes were transiently expressed only by postnatal OPCs until they began differentiating. These findings suggest that embryonic OPCs represent a developmental stage similar to postnatal OPCs, but without synaptic input, indicating a unique transcriptional signature between OPCs and neural precursors.

Finally, research by Sun, Q. *et al.* [3] focused on the role of miR-181a-5p in hippocampal neural stem cell (NSC) proliferation and its impact on learning and memory impairments associated with aging. The researchers discovered that the expression of miR-181a-5p was reduced in the NSCs of aged mice. They found that increasing the level of miR-181a-5p promoted NSC proliferation without affecting the

differentiation of NSCs into neurons and astrocytes. Further investigation revealed that miR-181a-5p targeted and regulated phosphatase and tensin homolog (PTEN), a negative regulator of the AKT signaling pathway. Knocking down PTEN rescued impaired NSC proliferation caused by low miR-181a-5p levels. Importantly, over-expressing miR-181a-5p in the dentate gyrus region of the brain enhanced NSC proliferation and improved learning and memory impairments in aged mice. These findings highlight the functional role of miR-181a-5p in NSC proliferation and its implications for aging-related learning and memory impairments in the hippocampus.

Through the methods and applications presented in this article collection, we hope to educate researchers on new technologies and methodologies for the isolation and separation of neural cells. To gain a deeper understanding of available options for improving your research, we encourage you to visit Miltenyi Biotec. We also invite you to delve into the intriguing world of adult brain dissociation and neural cell isolation through engaging webinars on this webpage.

Róisín Murtagh
Editor at *Wiley Analytical Science*

References

[1] Holt, L.M. et al. (2019). Magnetic Cell Sorting for In Vivo and In Vitro Astrocyte, Neuron, and Microglia Analysis. *Current Protocols in Neuroscience.* DOI: 10.1002/cpns.71.

[2] Vana, N.S. et al. (2023). Early cortical oligodendrocyte precursor cells are transcriptionally distinct and lack synaptic connections. *GLIA.* DOI: 10.1002/glia.24388.

[3] Sun, Q. et al. (2023). MiR-181a-5p promotes neural stem cell proliferation and enhances the learning and memory of aged mice. *Aging Cell.* DOI: 10.1111/acel.13794.

Magnetic Cell Sorting for In Vivo and In Vitro Astrocyte, Neuron, and Microglia Analysis

Leanne M. Holt,[1,2] S. Tristan Stoyanof,[2] and Michelle L. Olsen[2,3]

[1]Department of Cell, Developmental, and Integrative Biology, University of Alabama at Birmingham, Birmingham, Alabama
[2]School of Neuroscience, Virginia Polytechnic and State University, Blacksburg, Virginia
[3]Corresponding author: *molsen1@vt.edu*

Interest in evaluating individual cellular populations in the central nervous system has prompted the development of several techniques enabling the enrichment of single-cell populations. Herein we detail a relatively inexpensive method to specifically isolate neurons, astrocytes, and microglia from a mixed homogenate utilizing magnetic beads conjugated to cell-type specific antibodies. We have used this technique to isolate astrocytes across development and into late adulthood. Finally, we detail the utilization of this technique in novel astrocyte and astrocyte/neuron co-culture paradigms. © 2019 by John Wiley & Sons, Inc.

Keywords: astrocyte • cell isolation • co-culture • magnetic cell separation • microglia • neuron

How to cite this article:
Holt, L. M., Stoyanof, S. T., & Olsen, M. L. (2019). Magnetic cell sorting for in vivo and in vitro astrocyte, neuron, and microglia analysis. *Current Protocols in Neuroscience*, *88,* e71.
doi: 10.1002/cpns.71

INTRODUCTION

Cell-type specific examination in the central nervous system (CNS) has been of interest for many years. Recent research highlights the specific contributions of different cellular populations to normal and abnormal CNS development, aging, and disease (Hansen, Hanson, & Sheng, 2018; Hoye et al., 2018; Kopec, Smith, Ayre, Sweat, & Bilbo, 2018; Lioy et al., 2011; Peferoen, Kipp, van der Valk, van Noort, & Amor, 2014; Yu et al., 2018). To address cell-type specific contributions, several techniques have been developed, including magnetic-activated cell sorting (MACS). Herein we describe the sequential isolation of CNS cell types via MACS. We find that MAC sorting of neural cells is relatively gentle, resulting in cells that retain processes. The retention of cellular processes is important when experiments aim to examine molecular signals important in activity-dependent processes. The collected cells can be used for downstream experiments such as western immunoblotting, quantitative PCR, RNA sequencing, and proteomics. MAC sorting additionally allows for the investigation of cell-cell communication with direct co-culturing of mixed cellular populations. Directly targeting these populations of interest allows for the isolation and co-culture of mixed cellular populations without the need for passaging and re-plating of cells. The co-culture of different cell types or mixed genotypes can potentially give researchers greater insight into disease progression.

CURRENT PROTOCOLS
A Wiley Brand

Current Protocols in Neuroscience e71, Volume 88
Published in Wiley Online Library (wileyonlinelibrary.com).
doi: 10.1002/cpns.71

Within this article, we detail protocol steps to isolate major CNS cell populations from a whole brain homogenate via magnetic cell separation. Brain regions of interest are enzymatically digested into a single-cell suspension and incubated with antibodies against an extracellular protein on the population of interest. These antibodies are conjugated to magnetic beads. When the suspension is passed through a column placed within a strong magnetic field, the targeted, labeled cells remain on the column while the non-targeted population flows through. Targeting one cellular population at a time allows for the sequential isolation of individual CNS cell types. We additionally detail methodology for the isolation and subsequent culture of astrocytes, neurons, and astrocyte/neuron co-cultures from the isolated populations.

NOTE: Protocols using live animals must first be reviewed and approved by an Institutional Animal Care and Use Committee (IACUC) or must conform to governmental regulations regarding the care and use of laboratory animals.

BASIC PROTOCOL 1

SEQUENTIAL ISOLATION OF MICROGLIA, ASTROCYTES, AND NEURONS

Within this protocol, we detail the isolation and collection of cellular populations for RNA isolation. For those interested in MACS for protein isolation, simply substitute snap-freezing the fractions at the steps where addition of RNA*later* is indicated.

NOTE: Unless otherwise indicated, it is best to keep all solutions at 4°C for the duration of the protocol. This will help prevent activation of detrimental cellular pathways.

Materials

Experimental animals (sex, age, or strain depend on researcher's needs; we use 20- to 30-day-old, male and female wildtype C57BL/6 mice)
Artificial cerebrospinal fluid (ACSF; see recipe)
0.5% BSA in PBS (see recipe):
  PBS (Biorad, cat. no. 161-0780)
  BSA, fatty acid free (MilliporeSigma, cat. no. A7030)
Carbogen (95% O_2/5% CO_2 gas tank, Praxair, cat. no. MM OXCD5-K)
Carbon dioxide (Praxair, cat. no. CD M-50)
Worthington Papain Dissociation Kit (Worthington, cat. no. LK003178)
RNA*later* Stabilization Solution (Thermo Fisher Scientific, cat. no. AM7021)
MACS Myelin Beads, human, mouse, rat (Miltenyi Biotec, cat. no. 130-104-253)
MACS Cd11b$^+$ Microbeads, mouse (Miltenyi Biotec, cat. no. 130-093-634)
MACS ACSA-2 MicroBead Kit, mouse (Miltenyi Biotec, cat. no. 130-097-678)
MACS Neuron Isolation Kit, mouse (Miltenyi Biotec, cat. no. 130-115-389)

Sealed induction chamber (Scivena Scientific, cat. no. RES643)
10-ml serological pipets (Thermo Fisher Scientific, cat. no. 02-707-155)
Water bath (Thermo Fisher Scientific, cat. no. FSGPD05)
Auto-pipet (Waverly, cat. no. YF184AE0001107)
Centrifuge (Eppendorf 5804R, Rotor A-4-44)
50-ml Falcon conical tubes (Thermo Fisher Scientific, cat. no. 14-432-22)
70-µm Falcon Cell Strainer (Thermo Fisher Scientific, cat. no. 08-771-2)
MidiMACS Separator or QuadroMACS Separator (Miltenyi Biotec, cat. no. 130-042-302 and cat. no. 130-090-976)
LS columns (Miltenyi Biotec, cat. no. 130-042-401)

Prepare Worthington papain dissociation kit

1. Add 32 ml Earle's balanced salt solution (EBSS) to the albumin-ovomucoid inhibitor and allow the contents to dissolve.

Perform this step only when first opening the Worthington papain dissociation kit. Once prepared, the solutions are stable for up to 1 month.

2. Add 5 ml EBSS to the papain vial. Mix gently to dissolve the powder.
3. Add 500 µl EBSS to a DNase vial. Mix gently and allow powder to fully dissolve. Transfer 250 µl of this solution to the vial containing papain. Store the rest of the DNase solution on ice until needed.
4. Equilibrate papain solution by exposure to 95% O_2/5% CO_2 without directly bubbling gas through the papain solution.

   In order to do so, secure the tubing that is supplying the gas just above the surface of the papain solution. Having the gas disturb the surface of the papain solution is more than sufficient for equilibration. We find direct bubbling of the papain results in loss of solution volume. While you perform the tissue microdissections, keep the solution at room temperature.

Dissociate mouse cortex into single-cell suspension

5. Equilibrate prepared ACSF by exposure to 95% O_2/5% CO_2 for at least 15 min. For this step, directly bubble gas through the solution.
6. Anesthetize animal with CO_2 1 min and rapidly decapitate. Remove brain and dissect brain region of interest.

   It is not necessary to remove the meninges for this protocol.

   Mince microdissected tissue into 100-mm^3 sections using scissors; for animals younger than 15 days old, forceps can also be used.
7. Transfer carbogenated papain into a 50-ml conical tube. Use a modified cap to allow for continuous bubbling of the solution with 95% O_2/5% CO_2 during incubation.

   Use a pair of scissors or strong forceps to cut or drill a small hole into the conical tube cap that is equal to the size of the tubing. See Figure 1 for visual guide to construction.
8. Slowly draw up minced tissue using a 10-ml serological pipet. Allow tissue to separate from the solution and settle at the bottom of the pipet. Release only the settled tissue into the prepared papain.
9. Incubate tissue/papain mixture 15 to 20 min in a water bath set to 37°C. Swirl conical tube every 5 min to maximize the tissue's exposure to the papain. Keep solution equilibrated with exposure to 95% O_2/5% CO_2, however do not directly bubble gas into the papain solution during this step.
10. Gently triturate tissue with a 10-ml serological pipet (using an auto-pipet set to Slow or Medium) up and down 12 to 15 times until the solution is homogenous; the solution should be cloudy and light pink in appearance.

    The speed of trituration may require optimization for different experimental designs. A fast trituration will result in better dissociation of the tissue but will also give rise to processes that can shear cells. A slower trituration will be less efficient in dissociation of tissue but will be gentler on the cells.
11. Centrifuge homogenized solution at 300 × *g* for 3 min at room temperature.

    Use a centrifuge that can hold 50- and 15-ml conical tubes; our centrifuge can hold 2 × 50-ml and 8 × 15-ml tubes simultaneously. The centrifuge also needs to spin at 300 × g at a controlled temperature.

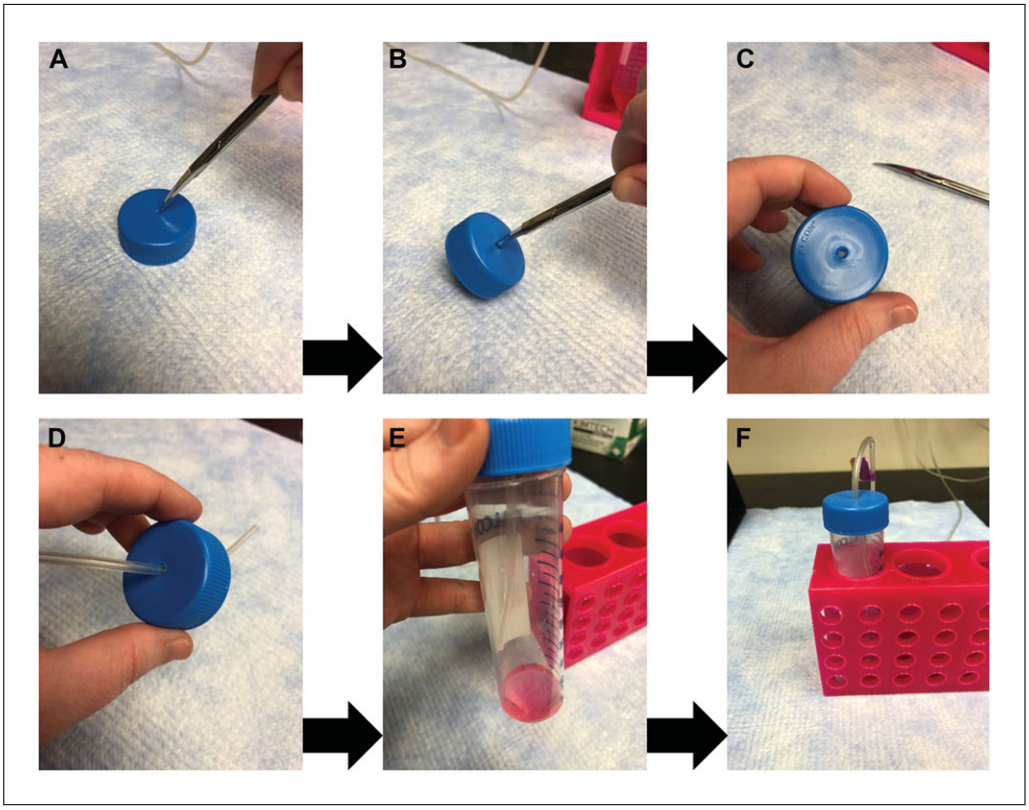

Figure 1 Creation of the modified conical tube cap for bubbling solutions. Sharp scissors (**A**) or forceps can be used to drill a small hole in the cap of a conical tube (**B**, **C**) to fit the size of tubing. The tubing can be fed through the cap to allow for constant oxygenation of the solutions during papain dissociation (**D**, **E**). Note that as demonstrated in **E** and **F**, direct bubbling of the papain solution should be avoided during incubations.

12. Prepare resuspension buffer as directed in the Worthington papain dissociation kit by mixing 2.7 ml EBSS, 300 µl albumin-ovomucoid inhibitor, and remaining 150 µl DNase.

13. Discard supernatant and immediately resuspend cell pellet in the resuspension buffer prepared in step 12 and mix well.

14. Prepare a discontinuous density gradient by adding 5 ml albumin-inhibitor solution to a new conical tube. Carefully layer cell suspension from step 13 on top of the albumin solution. Centrifuge at 300 × *g* for 5 min at room temperature.

15. Discard supernatant and immediately suspend pelleted cells in 8 ml PBS/BSA solution. To ensure a single-cell suspension, filter solution using a 70-µm BD Falcon filter to remove any non-dissociated tissue.

    The filter should be wetted prior to applying the cells. We typically use 2 ml to wet the filter for a total volume of 10 ml.

16. Remove 1 ml filtered solution as the whole cortex fraction.

    This fraction is 10% of total dissociated cells. The mixed-cellular population, whole cortex fraction can then be used as an input control for subsequent analyses.

17. Centrifuge whole cortex fraction at 300 × *g* for 3 min at 4°C and discard supernatant. Add 150 µl RNA*later* to the whole cortex fraction and set aside.

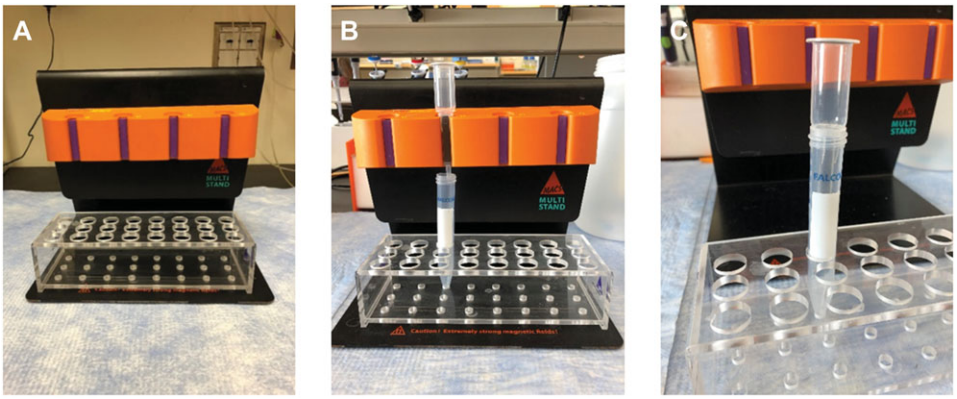

Figure 2 Images of MACS separators and columns. (**A**) The QuadroMACS is placed on the magnetic stand. (**B**) To separate cellular populations, a column is placed in the individual slots with a conical tube underneath to collect the flow-through. (**C**) To elute specific cellular populations, remove the column from the separator and use the supplied plunger. MACS, magnetic-activated cell sorting.

Remove myelin debris

18. Centrifuge remaining 9-ml single-cell suspension fraction at 300 × *g* for 3 min at 4°C and discard supernatant.

19. Resuspend pelleted cells in 150 µl PBS/BSA solution. Add 15 to 20 µl anti-myelin microbeads. Incubate mixture at 4°C for 10 min with a gentle mix every 5 min.

    These microbeads target myelin basic protein and therefore will remove myelin debris and mature oligodendrocytes.

20. Add 1 ml PBS/BSA solution to the conical tube and centrifuge at 300 × *g* for 3 min at 4°C to pellet the cells; this will remove any excess beads from the solution.

21. Place LS column into the MidiMACS or QuadroMACS (Fig. 2). Place a fresh 15- or 50-ml conical tube at the bottom.

    This will be used to collect the non-targeted cells.

    Apply 2 ml PBS/BSA to the column; pre-wetting the column will prevent any non-labeled cells from becoming stuck in the dry column.

22. Remove and discard resulting supernatant from step 20. Resuspend pellet in 500 µl PBS/BSA solution and apply directly to the prepared LS column. Collect flow-through into the 50-ml conical tube.

    The flow-through contains the microglia, astrocytes, and neurons.

23. Add 3 ml PBS/BSA to the column. Continue to collect the flow-through. Repeat this step one more time for a total of two 3 ml solution applications.

Isolate Microglia Fraction

24. Centrifuge collected flow-through from step 23 at 300 × *g* for 3 min at 4°C and discard supernatant. Resuspend pelleted cells in 150 µl PBS/BSA solution.

25. Add 10 to 15 µl $Cd11b^+$ microbeads.

    These microbeads will target microglia populations.

    Incubate mixture at 4°C for 10 min with a gentle mix every 5 min.

26. Add 1 ml PBS/BSA solution to the conical tube and centrifuge at 300 × *g* for 3 min at 4°C to pellet the cells.

    This will remove any excess beads from the solution.

27. Place LS column into the MidiMACS or QuadroMACS. Place a fresh 50-ml conical tube at the bottom.

    This will be used to collect the non-targeted cells.

    Apply 2 ml PBS/BSA to the column; pre-wetting the column will prevent any non-labeled cells from becoming stuck in the dry column.

28. Remove and discard resulting supernatant from step 26. Resuspend pellet in 500 µl PBS/BSA solution and apply directly to the LS column. Collect flow-through into the 50-ml conical tube.

    The flow-through contains the astrocytes and neurons while the microglia will remain on the LS column.

29. Add 3 ml PBS/BSA to the column. Continue to collect the flow-through. Repeat this step one more time for a total of two 3 ml solution applications.

30. Remove LS column from the magnetic holder and place into a fresh 15-ml conical tube. Elute targeted microglial population by adding 5 ml PBS/BSA solution. Use the supplied plunger to push the solution through the LS column.

    This will apply gentle pressure to remove the microglia from the column and result in a Microglia Fraction.

31. Centrifuge Microglia Fraction at 300 × *g* for 3 min at 4°C and discard supernatant. Add 150 µl RNA*later* to the Microglia Fraction and set aside.

Isolate Astrocyte Fraction

32. Centrifuge collected flow-through at 300 × *g* for 3 min at 4°C and discard supernatant. Resuspend pelleted flow-through cells in 150 µl PBS/BSA solution.

33. Add 10 to 15 µl FcR blocking cocktail microbeads from the ACSA-2 MicroBead kit.

    This cocktail will prevent non-specific binding for the ACSA-2 microbeads.

    Incubate mixture at 4°C for 10 min with a gentle mix every 5 min.

34. Add 10 to 15 µl anti-ACSA-2 from the kit. Incubate mixture at 4°C for 10 min with a gentle mix every 5 min.

    These microbeads target an extracellular protein on astrocytes.

35. Add 1 ml PBS/BSA solution to the conical tube and centrifuge at 300 × *g* for 3 min at 4°C to pellet the cells.

    This will remove any excess beads from the solution.

36. Place LS column into the MidiMACS or QuadroMACS. Place a fresh 50-ml conical tube at the bottom.

    This will be used to collect the non-targeted cells.

    Apply 2 ml PBS/BSA to the column; pre-wetting the column will prevent any non-labeled cells from becoming stuck in the dry column.

37. Remove and discard resulting supernatant from step 35. Resuspend pellet in 500 µl PBS/BSA solution and apply directly to the LS column. Collect flow-through into a new, fresh 50-ml conical tube.

    The flow-through contains the neurons while the astrocytes will remain on the LS column.

38. Add 3 ml PBS/BSA to the column. Continue to collect the flow-through. Repeat this step one more time for a total of two 3 ml solution applications.

39. Remove LS column from the magnetic holder and place into a fresh 15-ml conical tube. Elute targeted astrocyte population by adding 5 ml PBS/BSA solution. Use the supplied plunger to push the solution through the LS column.

    This will apply gentle pressure to remove the astrocytes from the column and result in an Astrocyte Fraction.

40. Centrifuge Astrocyte Fraction at 300 × *g* for 3 min at 4°C and discard supernatant. Add 150 µl RNA*later* and set aside.

Isolate Neuron Fraction

41. Centrifuge collected flow-through at 300 × *g* for 3 min at 4°C and discard supernatant. Resuspend pelleted cells in 150 µl PBS/BSA solution.

42. Add 10 to 15 µl anti-biotin blocking cocktail microbeads from the Neuron Isolation kit.

    This cocktail will target non-neuronal cellular populations.

    Incubate mixture at 4°C for 10 min with a gentle mix every 5 min.

43. Add 10 to 15 µl anti-biotin antibodies from the kit. Incubate mixture at 4°C for 10 min with a gentle mix every 5 min.

44. Add 1 ml PBS/BSA solution to the conical tube and centrifuge at 300 × *g* for 3 min at 4°C to pellet the cells.

    This will remove any excess beads from the solution.

45. Place LS column into the MidiMACS or QuadroMACS. Place a fresh 50-ml conical tube at the bottom.

    This will be used to collect the non-targeted cells.

    Apply 2 ml PBS/BSA to the column; pre-wetting the column will prevent any non-labeled cells from becoming stuck in the dry column.

46. Remove and discard resulting supernatant from step 44. Resuspend pellet in 500 µl PBS/BSA solution and apply directly to the LS column. Collect flow-through into a new, fresh 50-ml conical tube.

    The flow-through contains the Neuron Fraction while the target, non-neuronal cell types will remain on the LS column.

47. Add 3 ml PBS/BSA to the column. Continue to collect the flow-through (Neuron Fraction). Repeat this step one more time for a total of two 3 ml solution applications.

48. Centrifuge collected flow-through at 300 × *g* for 3 min at 4°C and discard supernatant. Add 150 µl RNA*later* to the Neuron Fraction and set aside.

49. Store all fractions in RNA*later* according to the manufacturer's instructions.

We have found that pelleted samples can be kept at 4°C in RNAlater for up to 3 weeks. It is recommended that these samples be moved to either −20°C or −80°C for long-term storage.

BASIC PROTOCOL 2

ISOLATION AND CO-CULTURE OF NEURONS AND ASTROCYTES

Within this protocol, we detail the isolation and collection of neurons and astrocytes for co-culture. Previous techniques for co-culture require utilization of embryonic pups for culturing neurons onto an astrocyte feeder layer. In the protocol below, we detail methodology that circumvents this and allows for direct co-culture of astrocytes and neurons. In our experience, these cultures are stable up to 14 to 20 days post plating.

NOTE: Unless otherwise indicated, it is best to keep all solutions at 4°C for the duration of the protocol. This will help prevent activation of detrimental cellular pathways.

Materials

Experimental animals (sex, age, or strain depend on researcher's needs; we use 0- to 5-day-old, male and female wildtype C57BL/6 mice)
Neuron medium (see recipe)
Artificial cerebrospinal fluid (ACSF; see recipe)
0.5% BSA in PBS (see recipe):
  PBS (Biorad, cat. no. 161-0780)
  BSA, fatty acid free (MilliporeSigma, cat. no. A7030)
100% ethanol (EtOH; Thermo Fisher Scientific, cat. no. A405P4)
Carbogen (95% O_2 /5% CO_2 gas tank, Praxair, cat. no. MM OXCD5-K)
Poly-L-lysine hydrobromide (0.1 mg/ml in sterile water; MilliporeSigma, cat. no. P2636)
Laminin (MilliporeSigma, cat. no. L2020)
Cytosine arabinoside (araC; 1-β-D-arabinofuranosylcytosine; MilliporeSigma, cat. no. C1768)
Worthington Papain Dissociation Kit (Worthington, cat. no. LK003178)
MACS Myelin Beads, human, mouse, rat (Miltenyi Biotec, cat. no. 130-104-253)
MACS Cd11b$^+$ Microbeads, mouse (Miltenyi Biotec, cat. no. 130-093-634)
MACS ACSA-2 MicroBead Kit, mouse (Miltenyi Biotec, cat. no. 130-097-678)
MACS Neuron Isolation Kit, mouse (Miltenyi Biotec, cat. no. 130-115-389)

Bunsen burner (Humboldt, cat. no. 6200.1)
10-ml serological pipets (Thermo Fisher Scientific, cat. no. 02-707-155)
Water bath (Thermo Fisher Scientific, cat. no. FSGPD05)
Centrifuge (Eppendorf 5804R, Rotor A-4-44)
24-well tissue culture plate (Thermo Fisher Scientific, cat. no. 353047)
Microscope cover glass (Thermo Fisher Scientific, cat. no. 12-545-M)
Nalgene Rapid-Flow sterile disposable filter units with PES membrane (Thermo Fisher Scientific, cat. no. 565-0020)
Lab forceps (World Precision Instruments, cat. no. 504506)
Lab scissors (Thermo Fisher Scientific, cat. no. 731210)
5-ml Luer centric syringe (Thermo Fisher Scientific, cat. no. 14-817-53)
0.2-µm syringe filter, sterile (Thermo Fisher Scientific, cat. no. 726-2520)
50-ml Falcon conical tubes (Thermo Fisher Scientific, cat. no. 14-432-22)
Pasteur pipets (Thermo Fisher Scientific, cat. no. 13-678-20D)
70-µm Falcon cell strainer (Thermo Fisher Scientific, cat. no. 08-771-2)
MidiMACS Separator or QuadroMACS Separator (Miltenyi Biotec, cat. no. 130-042-302 and cat. no. 130-090-976)
LS columns (Miltenyi Biotec, cat. no. 130-042-401)

Prepare culture plates

1. Sterilize glass coverslips prior to placing into individual wells in a 24-well plate.

   We store our coverslips in 100% EtOH. Prior to plating, each coverglass is briefly exposed to a Bunsen burner. If the biosafety cabinet (BSC) is not equipped with a gas line, leave the filled culture plate open and allow the EtOH to evaporate.

2. Add 500 µl 0.1 mg/ml poly-L-lysine to each well. Incubate overnight at room temperature. Following incubation, wash glass coverslips three times with sterile water.

3. Expose a 200-µl pipet tip to a Bunsen burner set to a low flame. Once warm, gently press tip to an inverted culture plate lid such that the tip now has a flat, circular end. Add 1 µl laminin to a coverslip and use the flattened pipet tip to swirl the laminin to ensure coating of the entire coverslip. Repeat for all glass coverslips.

Prepare Worthington papain dissociation kit

4. Add 32 ml EBSS to the albumin-ovomucoid inhibitor and allow contents to dissolve.

   Perform this step only when first opening the Worthington papain dissociation kit. Once prepared, the solutions are stable for up to 1 month.

5. Add 5 ml EBSS to the papain vial. Mix gently to dissolve the powder.

6. Add 500 µl EBSS to a DNase vial. Mix gently and allow powder to fully dissolve. Transfer 250 µl of this solution to the vial containing the papain. Store the rest of the DNase solution on ice until needed.

7. Equilibrate papain solution by exposure to 95% O_2/5% CO_2. While you perform the tissue microdissections, keep solution at room temperature.

Dissociate mouse cortex into single-cell suspension

8. Rapidly decapitate the postnatal day 0 to 1 animal. Remove brain; dissect brain region of interest in gas-treated ACSF and remove meninges. Mince microdissected tissue into 100-mm^3 sections using scissors or forceps.

   The use of CO_2 in animals younger than 12 days is not recommended. Therefore, rapid decapitation is used for euthanasia.

9. Sterile-filter the carbogenated papain into a 50-ml conical tube. Slowly draw up minced tissue using a 10-ml serological pipet. Allow tissue to separate from the solution and settle at the bottom of the pipet. Release only settled tissue into the prepared papain.

   To sterile-filter the papain, draw up the solution into a 5-ml syringe. Apply the sterile-filter to the end and release the papain into the 50-ml conical tube.

10. Incubate tissue/papain mixture 15 to 20 min in a water bath set to 37°C. Swirl conical tube every 5 min to maximize the tissue's exposure to the papain.

11. Gently triturate tissue with the 10-ml serological pipet five times up and down with setting turned to Slow. Do not over triturate the tissue at this step.

12. Centrifuge homogenized solution at 300 × *g* for 3 min at room temperature.

13. Prepare resuspension buffer by mixing 2.7 ml EBSS, 300 µl albumin-ovomucoid inhibitor, and the remaining 150 µl DNase.

14. Discard supernatant and immediately resuspend cell pellet in 1 ml resuspension buffer prepared in the step above.

15. Fire-polish a glass Pasteur pipet.

The Bunsen burner should be set to a low flame. Expose only the tip while rotating the pipet. A correctly fire-polished pipet should have a smooth, rounded tip that is slightly smaller than an unpolished pipet.

16. Triturate tissue using the fire-polished pipet up and down five times with setting turned to Slow.

    The solution should now be homogenous with a cloudy, light pink appearance.

    Centrifuge at 300 × *g* for 5 min at room temperature.

17. Discard supernatant and immediately suspend pelleted cells in 4 ml PBS/BSA solution. To ensure that you have a single-cell suspension, filter solution using a 70-µm BD Falcon filter to remove any non-dissociated tissue.

    The filter should be wetted prior to applying the cells. We typically use 1 ml to wet the filter for a total volume of 5 ml

Remove myelin debris and microglia

18. Centrifuge single-cell suspension at 300 × *g* for 3 min at 4°C and discard supernatant. Resuspend pelleted cells in 150 µl PBS/BSA solution.

19. Add 10 to 15 µl anti-myelin and 10 to 15 µl anti-Cd11b^{+} MicroBeads. Incubate mixture at 4°C for 10 min with a gentle mix every 5 min.

20. Add 1 ml PBS/BSA solution to the conical tube and centrifuge at 300 × *g* for 3 min at 4°C to pellet the cells.

    This will remove any excess beads from the solution.

21. Place LS column into the MidiMACS or QuadroMACS. Place a fresh 50-ml conical tube at the bottom.

    This will be used to collect the non-targeted cells.

    Apply 2 ml PBS/BSA to the column; pre-wetting the column will prevent any non-labeled cells from becoming stuck in the dry column.

22. Remove and discard supernatant from step 20. Resuspend pellet in 500 µl PBS/BSA solution and apply directly to the LS column. Collect flow-through into a new, fresh 50-ml conical tube.

    The flow-through contains the astrocytes and neurons.

23. Add 3 ml PBS/BSA to the column. Continue to collect the flow-through. Repeat this step one more time for a total of two 3 ml solution applications.

Isolate and plate Neuron Fraction

24. Centrifuge collected flow-through at 300 × *g* for 3 min at 4°C and discard supernatant. Resuspend pelleted cells in 150 µl PBS/BSA solution.

25. Add 10 to 15 µl anti-biotin blocking cocktail microbeads from the neuron isolation kit.

    This cocktail will target non-neuronal cellular populations.

    Incubate mixture at 4°C for 10 min with a gentle mix every 5 min.

26. Add 10 to 15 µl anti-biotin antibodies from the kit. Incubate mixture at 4°C for 10 min with a gentle mix every 5 min.

27. Add 1 ml PBS/BSA solution to the conical tube and centrifuge at 300 × *g* for 3 min at 4°C to pellet the cells.

    This will remove any excess beads from the solution.

28. Place LS column into the MidiMACS or QuadroMACS. Place a fresh 50-ml conical tube at the bottom.

    This will be used to collect the non-targeted cells.

    Apply 2 ml PBS/BSA to the column; pre-wetting the column will prevent any non-labeled cells from becoming stuck in the dry column.

29. Remove and discard resulting supernatant from step 27. Resuspend pellet in 500 µl neuron medium and apply directly to the LS column. Collect flow-through into a new, fresh 50-ml conical tube.

    The flow-through contains the Neuron Fraction while the targeted, non-neuronal cell types will remain on the LS column.

30. Add 3 ml neuron medium to the column. Continue to collect the flow-through (Neuron Fraction). Repeat this step one more time for a total of two 3 ml medium applications.

31. Determine the number of neurons collected using a hemacytometer and plate the neurons at 75–300 $\times$ 10^4 plating density in prepared 24-well plates (Current Protocols article: Phelan, 2007).

32. One day post-plating, add 2.5 µM araC (anti-mitotic cytarabine) to each well. Two days post-plating (1 day following araC treatment), perform a full medium change.

    Subsequent medium changes should be performed every 3 to 4 days at half-medium changes. In our experience, these cells are viable for 14 to 20 days post-plating. See Current Protocols article: Phelan, 2007 for information on culture techniques.

Isolate and plate astrocytes

33. Five days post-initial plating of neurons and when pups are 5 to 7 postnatal days in age, follow steps 1 through 17 to dissociate into a single-cell suspension and remove myelin debris and microglia.

34. Centrifuge collected flow-through at 300 $\times$ *g* for 3 min at 4°C and discard supernatant. Resuspend pelleted cells in 150 µl PBS/BSA solution.

35. Add 10 to 15 µl FcR blocking cocktail microbeads from the ACSA-2 kit.

    This cocktail will prevent non-specific binding for the ACSA-2 microbeads.

    Incubate mixture at 4°C for 10 min with a gentle mix every 5 min.

36. Add 10 to 15 µl anti-ACSA-2 from the kit. Incubate mixture at 4°C for 10 min with a gentle mix every 5 min.

    These microbeads target an extracellular protein on astrocytes.

37. Add 1 ml PBS/BSA solution to the conical tube and centrifuge at 300 $\times$ *g* for 3 min at 4°C to pellet the cells.

    This will remove any excess beads from the solution.

38. Place LS column into the MidiMACS or QuadroMACS. Place a fresh 50-ml conical tube at the bottom. This will be used to collect the non-targeted cells. Apply 2 ml PBS/BSA to the column.

    Pre-wetting the column will prevent any non-labeled cells from becoming stuck in the dry column.

39. Remove and discard resulting supernatant from step 37. Resuspend pellet in 500 µl PBS/BSA solution and apply directly to the LS column. Collect flow-through into a new, fresh 50-ml conical tube.

The flow-through contains the neurons while the astrocytes will remain on the LS column.

40. Add 3 ml PBS/BSA to the column. Continue to collect the flow-through. Repeat this step one more time for a total of two 3 ml solution applications.

41. Remove LS column from the magnetic holder and place into a fresh 15-ml conical tube. Elute targeted astrocyte population by adding 5 ml neuron medium. Use the supplied plunger to push the solution through the LS column.

    This will apply gentle pressure to remove the astrocytes from the column and results in an Astrocyte Fraction.

42. Determine the number of astrocytes collected using a hemacytometer and plate on top of the neurons at 75–300 $\times$ 10^4 plating density.

    Any remaining astrocytes may be plated as described in the Alternate Protocol.

ALTERNATE PROTOCOL

ISOLATION AND CULTURE OF ASTROCYTES

In addition to co-culture of neurons and astrocytes, MACS sorting can be utilized to culture astrocytes alone in serum-free conditions. Traditional astrocyte cultures are maintained in serum-containing medium. However, recent research has highlighted the experimental limitations to this in vitro technique. Here we detail methodology to culture astrocytes that bypasses the need for serum-containing medium.

Materials

Experimental animals (sex, age, or strain depend on researcher's needs; we use 0- to 5-day-old, male and female wildtype C57BL/6 mice)
Astrocyte medium (see recipe)
Artificial cerebrospinal fluid (ACSF; see recipe)
0.5% BSA in PBS (see recipe):
  PBS (Biorad, cat. no. 161-0780)
  BSA, fatty acid free (MilliporeSigma, cat. no. A7030)
100% ethanol (EtOH; Thermo Fisher Scientific, cat. no. A405P4)
Carbogen (95% O_2/5% CO_2 gas tank; Praxair, cat. no. MM OXCD5-K)
0.1 mg/ml poly-L-ornithine hydrobromide in sterile water (MilliporeSigma, cat. no. P3655)
Laminin (MilliporeSigma, cat. no. L2020)
Worthington Papain Dissociation Kit (Worthington, cat. no. LK003178)
MACS Myelin Beads, human, mouse, rat (Miltenyi Biotec, cat. no. 130-104-253)
MACS Cd11b$^+$ Microbeads, mouse (Miltenyi Biotec, cat. no. 130-093-634)
MACS ACSA-2 MicroBead Kit, mouse (Miltenyi Biotec, cat. no. 130-097-678)

Bunsen burner (Humboldt, cat. no. 6200.1)
Water bath (Thermo Fisher Scientific, cat. no. FSGPD05)
10-ml serological pipet (Thermo Fisher Scientific, cat. no. 02-707-155)
Centrifuge (Eppendorf 5804R, Rotor A-4-44)
24-well tissue culture plate (Thermo Fisher Scientific, cat. no. 353047)
Microscope cover glass (Thermo Fisher Scientific, cat. no. 12-545-M)
Lab forceps (World Precision Instruments, cat. no. 504506)
Lab scissors (Thermo Fisher Scientific, cat. no. 731210)
5-ml Luer centric syringe (Thermo Fisher Scientific, cat. no. 14-817-53)
0.2-µm syringe filter, sterile (Thermo Fisher Scientific, cat. no. 726-2520)
Pasteur pipets (Thermo Fisher Scientific, cat. no. 13-678-20D)
50-ml Falcon conical tubes (Thermo Fisher Scientific, cat. no. 14-432-22)
70-µm Falcon Cell Strainer (Thermo Fisher Scientific, cat. no. 08-771-2)

MidiMACS Separator or QuadroMACS Separator (Miltenyi Biotec, cat. no. 130-042-302 and cat. no. 130-090-976)
LS columns (Miltenyi Biotec, cat. no. 130-042-401)

NOTE: All steps should be performed in a biosafety cabinet using aseptic technique.

Prepare culture plates

1. Sterilize glass coverslips prior to placing into individual wells in a 24-well plate.

   We store our coverslips in 100% EtOH. Prior to plating, each coverglass is briefly exposed to a Bunsen burner. If the biosafety cabinet is not equipped with a gas line, leave the filled culture plate open to allow the EtOH to evaporate.

2. Add 500 µl poly-L-ornithine to each well. Incubate overnight at room temperature. Following incubation, wash glass coverslips three times with sterile water.

3. Expose a 200-µl pipet tip to a Bunsen burner set to a low flame. Once warm, gently press the tip to an inverted culture plate lid such that the tip now has a flat, circular end.

4. Add 1 µl laminin to a coverslip and use the flattened pipet tip to swirl the laminin to ensure coating of the entire coverslip. Repeat on all glass coverslips.

Prepare Worthington papain dissociation kit

5. Add 32 ml EBSS to the albumin-ovomucoid inhibitor in a biosafety cabinet and allow the contents to dissolve.

   Perform this step only when first opening the Worthington papain dissociation kit. Once prepared, the solutions are stable for up to 1 month.

6. Add 5 ml EBSS to the papain vial. Mix gently to dissolve the powder.

7. Add 500 µl EBSS to a DNase vial. Mix gently and allow powder to fully dissolve. Transfer 250 µl of this solution to the vial containing the papain. Store the rest of the DNase solution on ice until needed.

8. Equilibrate papain solution by exposure to 95% O_2/5% CO_2. While you perform the tissue microdissections, keep solution at room temperature.

Dissociate mouse cortex into single-cell suspension

9. Rapidly decapitate the postnatal day 3 to 5 animal. Remove brain; dissect brain region of interest in gas-treated ACSF and remove meninges. Mince microdissected tissue into 100-mm^3 sections using scissors or forceps.

   The use of CO_2 in animals younger than 12 days is not recommended. Therefore, rapid decapitation is used for euthanasia.

10. Sterile-filter carbogenated papain into a 50-ml conical tube. Slowly draw up minced tissue using a 10-ml serological pipet. Allow tissue to separate from the solution and settle at the bottom of the pipet. Release only the settled tissue into the prepared papain.

    To sterile-filter the papain, draw up the solution into a 5-ml syringe. Apply the sterile-filter to the end and release the papain into the 50-ml conical tube.

11. Incubate tissue/papain mixture 15 to 20 min in a water bath set to 37°C. Swirl conical tube every 5 min to maximize the tissue's exposure to the papain.

12. Gently triturate tissue with a 10-ml serological pipet (using an auto-pipet) up and down five times with setting turned to Slow. Do not over triturate the tissue at this step.

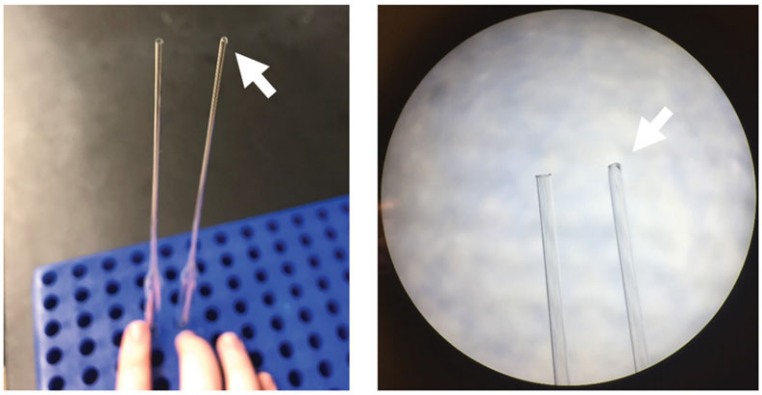

Figure 3 Comparison of Pasteur and fire-polished Pasteur pipets. Fire-polished pipets (arrows) are rounded and have a smaller opening.

13. Centrifuge homogenized solution at 300 × *g* for 3 min at room temperature.
14. Prepare resuspension buffer by mixing 2.7 ml EBSS, 300 µl albumin-ovomucoid inhibitor, and remaining 150 µl DNase.
15. Discard supernatant and immediately resuspend cell pellet in 1 ml resuspension buffer prepared in the step above.
16. Fire-polish a glass Pasteur pipet.

    The Bunsen burner should be set to a low flame. Expose only the tip while rotating the pipet. A correctly fire-polished pipet should have a smooth, rounded tip that is slightly smaller than an unpolished pipet (see Fig. 3 for reference).

17. Triturate tissue using the fire-polished pipet up and down five times with setting turned to Slow; the solution should now be homogenous with a cloudy, light pink appearance. Centrifuge at 300 × *g* for 5 min at room temperature.
18. Discard supernatant and immediately suspend pelleted cells in 4 ml PBS/BSA solution. To ensure a single-cell suspension, filter solution using a 70-µm BD Falcon filter to remove any non-dissociated tissue.

    The filter should be wetted prior to applying the cells. We typically use 1 ml to wet the filter for a total volume of 5 ml.

Remove myelin debris and microglia

19. Centrifuge single-cell suspension at 300 × *g* for 3 min at 4°C and discard the supernatant. Resuspend pelleted cells in 150 µl PBS/BSA solution.
20. Add 15 to 20 µl anti-myelin and anti-Cd11b$^+$ MicroBeads. Incubate mixture at 4°C for 10 min, with a gentle mix every 5 min.
21. Add 1ml PBS/BSA solution to the conical tube and centrifuge at 300 × *g* for 3 min at 4°C to pellet the cells; this will remove any excess beads from the solution.
22. Place the LS column into the MidiMACS or QuadroMACS. Place a fresh 50-ml conical tube at the bottom; this will be used to collect the non-targeted cells. Apply 2 ml PBS/BSA to the column.

    Pre-wetting the column will prevent any non-labeled cells from becoming stuck in the dry column.

23. Remove and discard the supernatant from step 21. Resuspend the pellet in 500 µl PBS/BSA solution and apply directly to the LS column. Collect flow-through into a new, fresh 50-ml conical tube.

The flow-through contains the astrocytes and neurons.

24. Add 3 ml PBS/BSA to the column. Continue to collect the flow-through. Repeat this step one more time for a total of two 3 ml solution applications.

Isolate and plate astrocytes

25. Centrifuge collected flow-through at 300 × *g* for 3 min at 4°C and discard supernatant. Resuspend pelleted cells in 150 µl PBS/BSA solution.

26. Add 10 to 15 µl FcR blocking cocktail microbeads from the ACSA-2 microbead kit.

    This cocktail will prevent non-specific binding for the ACSA-2 microbeads.

    Incubate mixture at 4°C 10 min with a gentle mix every 5 min.

27. Add 10 to 15 µl anti-ACSA-2 from the kit. Incubate mixture at 4°C 10 min with a gentle mix every 5 min.

    These microbeads target an extracellular protein on astrocytes.

28. Add 1 ml PBS/BSA solution to the conical tube and centrifuge at 300 × *g* for 3 minutes at 4°C to pellet the cells; this will remove any excess beads from the solution.

29. Place the LS column into the MidiMACS or QuadroMACS. Place a fresh 50-ml conical tube at the bottom; this will be used to collect the non-targeted cells. Apply 2 ml PBS/BSA to the column.

    Pre-wetting the column will prevent any non-labeled cells from becoming stuck in the dry column.

30. Remove and discard resulting supernatant from step 26. Resuspend pellet in 500 µl PBS/BSA solution and apply directly to the LS column. Collect flow-through into a new, fresh 50-ml conical tube.

    The flow-through contains the neurons while the astrocytes will remain on the LS column.

31. Add 3 ml PBS/BSA to the column. Continue to collect the flow-through. Repeat this step one more time for a total of two 3 ml solution applications.

32. Remove LS column from the magnetic holder and place into a fresh 15-ml conical tube. Elute targeted astrocyte population by adding 5 ml astrocyte medium. Use the supplied plunger to push the solution through the LS column.

    This will apply gentle pressure to remove the astrocytes from the column and results in an Astrocyte Fraction.

33. Determine the number of astrocytes collected using a hemacytometer and plate at 75–300 × 10^4 plating density.

REAGENTS AND SOLUTIONS

Artificial cerebrospinal fluid (ACSF)

For 50 ml ACSF:

50 µl 1 M $MgCl_2$ (0.95 g in 10 ml; MilliporeSigma, cat. no. M8266)
10 µl 1 M $CaCl_2$ (1.11 g in 10 ml; MilliporeSigma, cat. no. C1016)
50 µl 20 mM AP5 (10 mg AP5 in 2.6 ml water; Tocris, cat. no. 0106)
50 µl 20 mM CNQX (50 mg CNQX [Tocris, cat. no. 0910] in 10.76 ml DMSO [MilliporeSigma, cat. no. D5879])

Bring up to 50 ml with stock ACSF (see recipe). Make fresh daily.

ACSF must be carbogenated for at least 15 min before use.

Final concentrations: 2 mM $MgCl_2$, 0.2 mM $CaCl_2$, 20 nM AP5, and 20 mM CNQX.

Astrocyte medium

Prepare in a biosafety cabinet. For 500 ml:

10 ml 50× B27 (Thermo Fisher Scientific, cat. no. 17504-044)
2.5 ml 100 mM sodium pyruvate (Thermo Fisher Scientific, cat. no. 11360070)
2.5 ml 2 M glutamine (2.92 g in 100 ml water; Gibco brand, Thermo Fisher Scientific, cat. no. 21051-024)
500 µl penicillin/streptomycin (Thermo Fisher Scientific, cat. no. 15140122)
Bring up to 500 ml with equal parts minimal Earl's medium (MEM; Thermo Fisher Scientific, cat. no. 51200038) and neurobasal medium (Thermo Fisher Scientific, cat. no. 21103049). Store at room temperature for 2 to 3 weeks. Sterile-filter and warm to 37°C prior to use.

Final composition: 50% minimal Earl's medium, 50% neurobasal medium, 1 mM sodium pyruvate, 2 mM glutamine, 1× B27, and 500 U penicillin/streptomycin.

BSA in PBS, 0.5%

For 500 ml:

2.5 g BSA (fatty acid free; MilliporeSigma, cat. no. A7030) to 500 ml 1× PBS (Biorad, cat. no. 161-0780).

Store at 4°C for 3 to 4 weeks.

Neuron medium

Prepare in a biosafety cabinet. For 500 ml:

10 ml 50× B27 (Thermo Fisher Scientific, cat. no. 17504-044)
2.5 ml 2 M glutamine
500 µl penicillin/streptomycin
Bring up to 500 ml with neurobasal medium (Thermo Fisher Scientific, cat. no. 21103049).
Store at room temperature for 2 to 3 weeks. Sterile-filter and warm to 37°C prior to use.

Final composition: 1× B27, 2 mM glutamine, and 500 U penicillin/streptomycin.

Stock artificial cerebrospinal fluid (ACSF)

For 1 liter stock ACSF:

7 g NaCl (Thermo Fisher Scientific, cat. no. S671)
0.223 g KCl (Thermo Fisher Scientific, cat. no. BP366)
2.2 g $NaHCO_3$ (MilliporeSigma, cat. no. S6014)
2 g glucose (MilliporeSigma, cat. no. G8270)
Bring up to 1 liter with water.
Store at 4°C for up to 1 month.

Final concentrations: 120 mM NaCl, 3 mM KCl, 26.2 mM $NaHCO_3$, and 11.1 mM glucose.

COMMENTARY

Background Information

Several techniques have been developed to 'capture' unique cell populations from neural tissue. These include laser-capture microdissection (LCM), fluorescent activated sorting (FACS), and more recently translation ribosomal affinity purification (TRAP). Each technique offers unique advantages and limitations. To date, FACS is the method most frequently utilized. FACS is regularly performed

in fluorescent cell populations driven by cell-type specific fluorescent reporter genes but can also be performed in immunolabeled fresh or fixed tissue (Cahoy et al., 2008; Guez-Barber et al., 2012). One drawback to FACS is that cellular processes are shorn off in the flow cytometer as cells move through a rapidly flowing stream of fluid during the separation process. This limits the utility of this technique if total cell protein is the final outcome measure. Additionally, this technique requires a flow activated cell sorter, an expensive piece of equipment that not all researchers may access.

LCM is commonly used in fixed tissue to capture cellular populations of interest. The user "traces" the cells, which are dissected with a laser and subsequently collected (Decarlo, Emley, Dadzie, & Mahalingam, 2011). The specific isolation of the chosen cells gives researchers high specificity in cellular population and brain regions. This technique is particularly useful in human post-mortem tissue, where tissue is limited in quantity. However, similar to FACS, this technique requires specialized equipment. Additionally, this technique requires extensive training and expertise, as the individual user identifies cells for tracing and microdissection based on their morphological appearance, a limitation that may be circumvented by immunolabeling cells prior to LCM (Chabrat, Doucet-Beaupre, & Levesque, 2015).

Recently TRAP has become an attractive option (Ayata et al., 2018; Doyle et al., 2008; Heiman et al., 2008; Hoye et al., 2018; Yu et al., 2018). Fluorescently tagged ribosomes are expressed in a single-cell population using a cell-type specific promoter. The ribosomes are immunoprecipitated along with mRNA that is actively translated. While this technique has the major advantage of negating the need for enzymatic digestion to create a single-cell suspension, limitations include a 'snap shot' of the RNA pool that is undergoing active translation rather than the total RNA pool. To evaluate different cell types, multiple mouse lines driving cell-type specific fluorescently tagged ribosomes must be generated (Hoye et al., 2018). In contrast, the MACS technique is relatively fast and inexpensive, allowing for the isolation of multiple cellular populations from a single brain. The development of commercially available kits has increased the popularity of this technique. Limitations to this particular technique are similar to those we have already discussed, in that enzymatic digestion is utilized to generate single-cell suspensions, which causes cellular stress and may alter gene and protein expression. MACS, thus far, has not be performed in fixed tissue and requires an antibody targeted to extracellular proteins. Furthermore, depending on the desired downstream application, MACS may require larger inputs to capture an adequate number of cells. Simple pooling of animals may overcome this limitation. Overall, we find this technique to be relatively gentle in allowing for the retention of cellular processes important for some downstream applications, including evaluation of extra somatic proteins and 'capturing' cell populations for cell culture.

Within this article we also detail protocols for the culture of astrocytes alone and co-culture of astrocytes and neurons. The traditional, most commonly used astrocyte culture technique was initially reported in the 1980s (McCarthy & de Vellis, 1980). While this system has garnered a wealth of information for the field, drawbacks have been highlighted (for a review see Lange, Bak, Waagepetersen, Schousboe, & Norenberg, 2012).

The most prominent includes the lack of translation from cultured astrocytes to their in vivo counterparts, with different gene and protein expression (Cahoy et al., 2008; Doyle et al., 2008), biophysical properties, and a distinct lack of morphological complexity (Cahoy et al., 2008; Doyle et al., 2008; Foo et al., 2011). Many of these features have been attributed to the presence of serum in the culture medium (Foo et al., 2011). Serum contains high levels of glutamate, which is excitotoxic to neurons and results in their death within the culture dish (Ye & Sontheimer, 1998). Astrocytes and microglia remain, and microglia are shaken off prior to performing experiments on the astrocytes. Immunopanning of astrocytes has, to date, been the only proposed alternative (Foo et al., 2011). Immunopanning is performed by plating a dissociated cell suspension onto antibody-coated plates (Foo et al., 2011). Following a period of recovery, the cells are enzymatically lifted off the plate. The targeted cell populations bound to the antibodies remain on the plate, while non-targeted cell populations are removed. Typically, a series of plates is necessary to remove non-astrocytic cells such as microglia, oligodendrocytes, and neurons with a final plate targeting astrocytes.

Herein, we detail an alternative method for obtaining pure astrocyte cultures without the need for serum, resulting in astrocytes

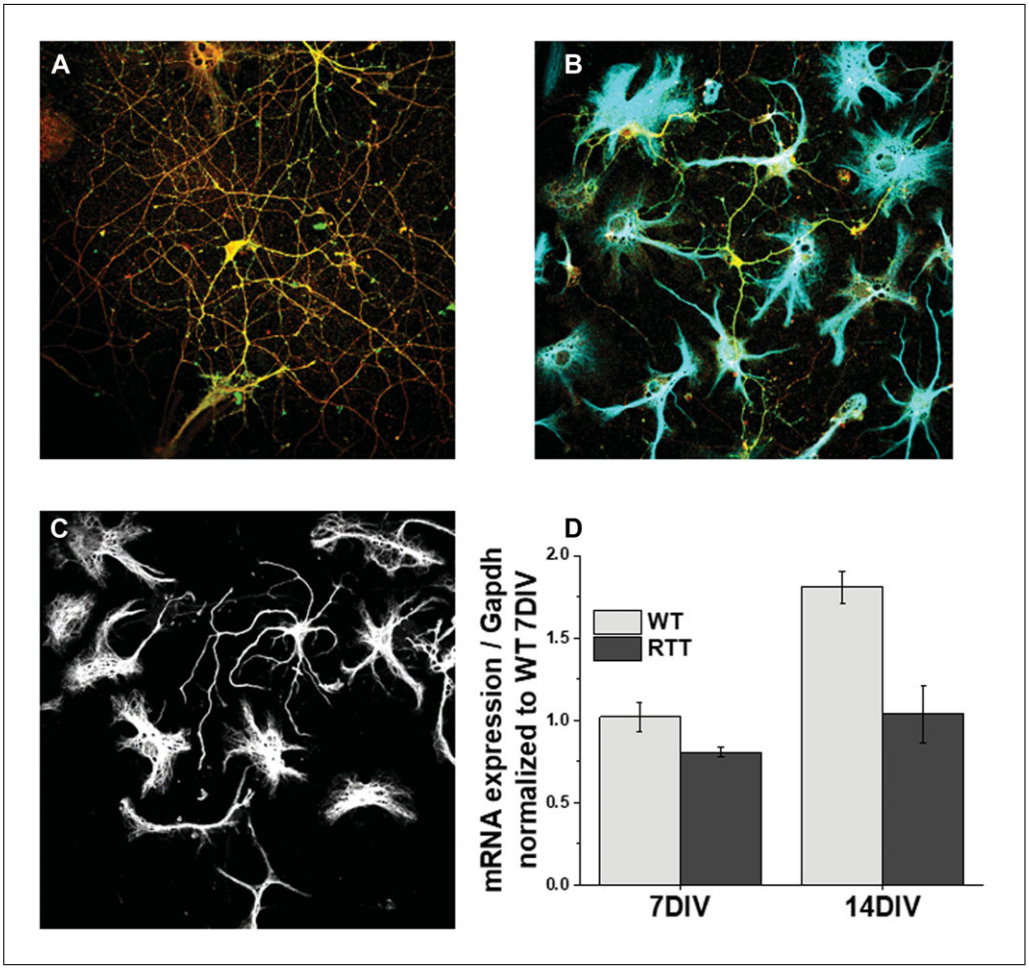

Figure 4 Representative images of (**A**) neurons alone, (**B**) neuron/astrocyte co-cultures, and (**C**) astrocytes alone. For A, B, and C, the cells were collected at 14DIV, fixed, and immunofluorescence performed. In A, neurons are visualized with presynaptic VGluT1 and postsynaptic marker PSD95 for synaptic quantification. In B, astrocytes visualized with Gfap (blue) are plated on top of neurons (green). In C, astrocytic filaments are visualized with Gfap (white) to demonstrate complex morphology of serum-free astrocyte cultures. (**D**) qPCR analysis of *Kcnj10* expression in wildtype (WT) and Mecp2 deficient (Rett syndrome) astrocytes reveals loss of astrocytic Kir4.1 expression is due to cell-autonomous loss of astrocytic Mecp2. (Reproduced with permission from Kahanovitch et al., 2018.)

with a significantly more complex morphology than traditional astrocyte cultures (Fig. 4C). We additionally detail a novel method to directly co-culture mixed cell populations. Typical co-culture protocols require a series of culturing and passaging of astrocytes prior to plating neurons on top, resulting in co-culture of cells that differ in age. (This negates the ability to culture different cell populations from littermates.) Furthermore, neuronal cultures are often performed in embryonic animals to reduce non-neuronal contamination. This results in the additional loss of the breeding mother. Magnetic separation allows for co-cultures in post-natal littermates, minimizing the number of breeding animals needed. Collectively, we have found that MACS separation is a relatively easy, fast, and inexpensive technique with a wide array of downstream applications.

Critical Parameters

This protocol can be utilized for a variety of experimental designs from brain regions, ages, and genotypes to RNA to protein to culture work. In our experience, a single mouse cortex is sufficient to capture $\sim$1–2 $\times$ 10^6 astrocytes and RNA that is suitable for RNA sequencing analysis. However, experiments designed to isolate cellular populations from a smaller region of interest may require pooling of animals.

Troubleshooting

See Table 1 for a listing of common problems and suggested solutions.

Table 1 Troubleshooting Commonly Encountered Problems

Potential problem	Common cause	Solution
Low yield of targeted population	Incomplete dissociation	Longer incubation with papain Better trituration
	Small brain region of interest	Combine and pool multiple animals
	Magnetic beads	Ensure beads are in-date Increase incubation time Ensure total number of cells is not clogging the LS column
Low cell viability	Dissociation	Decrease time in papain Ensure papain solution is equilibrated Decrease trituration speed/time
Low cell viability (culture specific)	Low plating density	Neurons do not survive on their own well, so ensure the plating density is sufficient
	Medium	Ensure medium is properly made Use fresh medium Ensure proper medium change schedule
	Culture plate	Increase incubation time for poly-lysine or poly-ornithine coating Ensure coverglass was washed 3×
	Incubator	Ensure incubator is set to proper conditions

Understanding Results

Following MACS separation of CNS cell populations, the isolated populations can be used for a variety of downstream applications. We demonstrate in Figure 5 the expected purity of each individual population. To determine the purity of the isolated populations, we use the "whole cortex" fraction as an input control to show enriched or depleted gene expression in purified cell populations (Holt & Olsen, 2016). For example, quantitative PCR (qPCR) analysis of the astrocyte fraction reveals one-fold enriched expression of *Gfap* compared to whole cortex with no expression of microglial (*Tmem119*), oligodendrocytic (*Mbp*), or neuronal (*Rbfox3*) gene expression (Fig. 5A). We can conclude, therefore, that we have specifically isolated only astrocytes in our astrocyte fraction. This holds true for microglia and neuron qPCR analysis as well (Fig. 5B, C). In contrast, we observe equal *Gfap* expression as whole cortex in the oligodendrocyte fraction (from the myelin-removal steps), suggesting astrocyte contamination in this fraction (Fig. 5D). For this reason, our current protocol does not include collecting the myelin-removal fraction. For those interested, however, it is possible to optimize the protocol to isolate pure oligodendrocytes. These isolated populations can then be used to examine cell-type specific gene expression changes in vivo. For example, we have used MACS to examine astrocytic gene expression in a mouse model of Rett syndrome (RTT; Kahanovitch et al., 2018). Examination of isolated astrocytes reveals a roughly 30% decrease in Kir4.1 mRNA expression in Mecp2 deficient astrocytes compared to their wildtype littermates (Fig. 5E).

Similarly, a variety of experimental designs can be implemented using MACS to isolate and culture specific CNS populations. Within this protocol, we detail neuron/astrocyte co-culture and astrocyte-alone culture paradigms. Figure 4 shows representative immunofluorescent images of neurons alone, astrocyte/neuron co-cultures, and astrocytes alone from 14 days in vitro. A higher neuronal plating density (Fig. 4A) results in a greater number of connections for neurons, whereas a lower density (Fig. 4B) may be more suitable for morphology assessments. We have utilized serum-free astrocyte cultures described within this article to demonstrate that the loss of Kir4.1 in RTT astrocytes is due specifically to the loss of MeCP2 in astrocytes (Fig. 4D). Again using MACS to culture astrocytes from wildtype and RTT littermate pups, qPCR

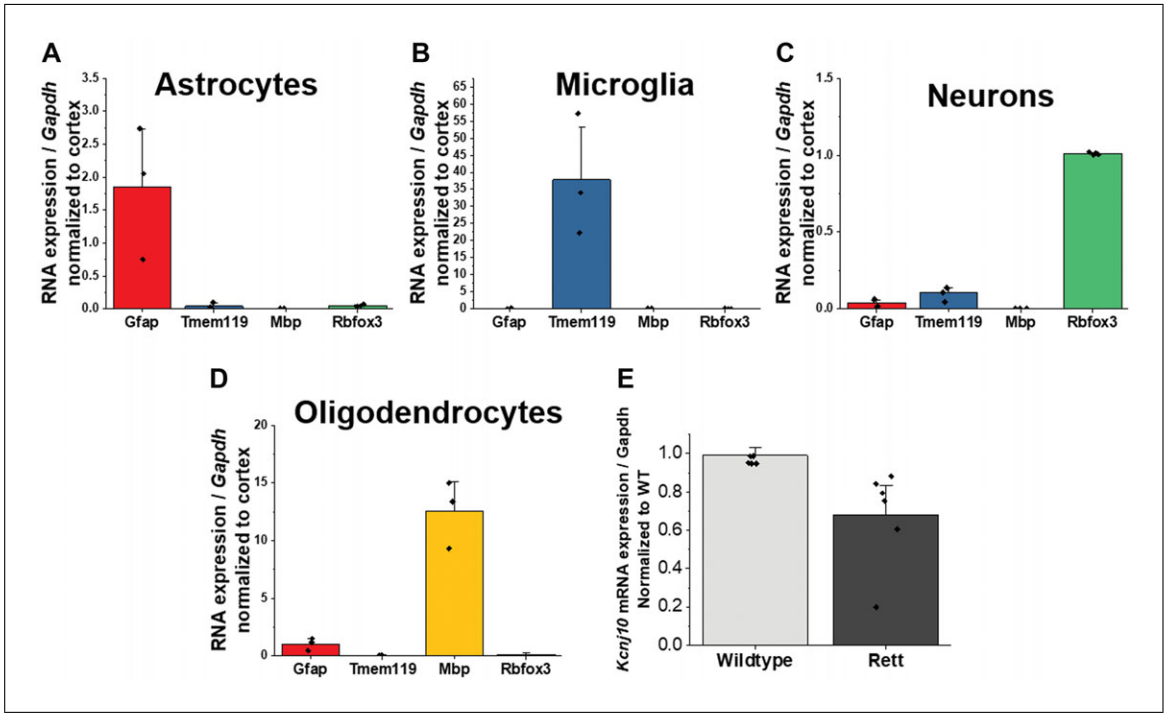

Figure 5 Quantitative PCR demonstrating sequential isolation of (**A**) astrocytes, (**B**) microglia, and (**C**) neuronal populations. Normalization to a mixed cellular population (whole cortex) allows for the examination of enrichment or depletion of cell-type specific gene markers. As demonstrated in **D**, oligodendrocytes display enrichment of *Gfap* and therefore astrocyte contamination. (**E**) MACs-isolated astrocytes from wildtype and Mecp2-deficient animals was utilized to demonstrate that astrocytes exhibit a decrease in *Kcnj10* mRNA expression. (Reproduced with permission from Kahanovitch et al., 2018.)

analysis demonstrated that wildtype astrocytes exhibit an increase in Kir4.1 expression over time, which is lost in Mecp2 deficient astrocytes (Kahanovitch et al., 2018).

Time Considerations

We find that the sequential isolation of CNS populations is easily performed within 3 hr. The addition or subtraction of cellular populations of interest will result in a modification of that timing. In totality, between preparing coverslips to plating of cells also takes 3 hr. We find the best results with overnight incubations of poly-lysine or poly-ornithine.

Acknowledgments

This work was funded by the National Institutes of Health NINDS R01NS075062 (M.L.O.) and F31NS100259 (L.M.H.).

Literature Cited

Ayata, P., Badimon, A., Strasburger, H. J., Duff, M. K., Montgomery, S. E., Loh, Y. E., ... Schaefer, A. (2018). Epigenetic regulation of brain region-specific microglia clearance activity. *Nature Neuroscience*, *21*(8), 1049–1060. doi: 10.1038/s41593-018-0192-3.

Cahoy, J. D., Emery, B., Kaushal, A., Foo, L. C., Zamanian, J. L., Christopherson, K. S., ... Barres, B. A. (2008). A transcriptome database for astrocytes, neurons, and oligodendrocytes: A new resource for understanding brain development and function. *Journal of Neuroscience*, *28*(1), 264–278. doi: 10.1523/JNEUROSCI.4178-07.2008.

Chabrat, A., Doucet-Beaupre, H., & Levesque, M. (2015). RNA isolation from cell specific subpopulations using laser-capture microdissection combined with rapid immunolabeling. *Journal of Visualized Experiments*, *98*, e52510. doi: 10.3791/52510.

Decarlo, K., Emley, A., Dadzie, O. E., & Mahalingam, M. (2011). Laser capture microdissection: Methods and applications. *Methods in Molecular Biology*, *755*, 1–15. doi: 10.1007/978-1-61779-163-5_1.

Doyle, J. P., Dougherty, J. D., Heiman, M., Schmidt, E. F., Stevens, T. R., Ma, G., ... Heintz, N. (2008). Application of a translational profiling approach for the comparative analysis of CNS cell types. *Cell*, *135*(4), 749–762. doi: 10.1016/j.cell.2008.10.029.

Foo, L. C., Allen, N. J., Bushong, E. A., Ventura, P. B., Chung, W. S., Zhou, L., ... Barres, B. A. (2011). Development of a method for the purification and culture of rodent astrocytes. *Neuron*, *71*(5), 799–811. doi: 10.1016/j.neuron.2011.07.022.

Guez-Barber, D., Fanous, S., Harvey, B. K., Zhang, Y., Lehrmann, E., Becker, K. G., ... Hope, B. T. (2012). FACS purification of immunolabeled cell types from adult rat brain. *Journal*

of Neuroscience Methods, *203*(1), 10–18. doi: 10.1016/j.jneumeth.2011.08.045.

Hansen, D. V., Hanson, J. E., & Sheng, M. (2018). Microglia in Alzheimer's disease. *Journal of Cell Biology*, *217*(2), 459–472. doi: 10.1083/jcb.201709069.

Heiman, M., Schaefer, A., Gong, S., Peterson, J. D., Day, M., Ramsey, K. E., … Heintz, N. (2008). A translational profiling approach for the molecular characterization of CNS cell types. *Cell*, *135*(4), 738–748. doi: 10.1016/j.cell.2008.10.028.

Holt, L. M., & Olsen, M. L. (2016). Novel applications of magnetic cell sorting to analyze cell-type specific gene and protein expression in the central nervous system. *PLoS One*, *11*(2), e0150290. doi: 10.1371/journal.pone.0150290.

Hoye, M. L., Regan, M. R., Jensen, L. A., Lake, A. M., Reddy, L. V., Vidensky, S., … Miller, T. M. (2018). Motor neuron-derived microRNAs cause astrocyte dysfunction in amyotrophic lateral sclerosis. *Brain*, *141*(9), 2561–2575. doi: 10.1093/brain/awy182.

Kahanovitch, U., Cuddapah, V. A., Pacheco, N. L., Holt, L. M., Mulkey, D. K., Percy, A. K., & Olsen, M. L. (2018). MeCP2 deficiency leads to loss of glial Kir4.1. *eNeuro*, *5*(1). doi: 10.1523/eneuro.0194-17.2018.

Kopec, A. M., Smith, C. J., Ayre, N. R., Sweat, S. C., & Bilbo, S. D. (2018). Microglial dopamine receptor elimination defines sex-specific nucleus accumbens development and social behavior in adolescent rats. *Nature Communications*, *9*(1), 3769. doi: 10.1038/s41467-018-06118-z.

Lange, S. C., Bak, L. K., Waagepetersen, H. S., Schousboe, A., & Norenberg, M. D. (2012). Primary cultures of astrocytes: Their value in understanding astrocytes in health and disease. *Neurochemical Research*, *37*(11), 2569–2588. doi: 10.1007/s11064-012-0868-0.

Lioy, D. T., Garg, S. K., Monaghan, C. E., Raber, J., Foust, K. D., Kaspar, B. K., … Mandel, G. (2011). A role for glia in the progression of Rett's syndrome. *Nature*, *475*(7357), 497–500. doi: 10.1038/nature10214.

McCarthy, K. D., & de Vellis, J. (1980). Preparation of separate astroglial and oligodendroglial cell cultures from rat cerebral tissue. *Journal of Cell Biology*, *85*(3), 890–902. doi: 10.1083/jcb.85.3.890.

Peferoen, L., Kipp, M., van der Valk, P., van Noort, J. M., & Amor, S. (2014). Oligodendrocyte-microglia cross-talk in the central nervous system. *Immunology*, *141*(3), 302–313. doi: 10.1111/imm.12163.

Phelan, M. C. (2007). Techniques for mammalian cell tissue culture. *Current Protocols in Neuroscience*, *38*(1), A.3B.1–A.3B.19. doi: 10.1002/0471142727.nsa03bs38.

Ye, Z. C., & Sontheimer, H. (1998). Astrocytes protect neurons from neurotoxic injury by serum glutamate. *Glia*, *22*(3), 237–248. doi: 10.1002/(SICI)1098-1136(199803)22:3%3c237::AID-GLIA3%3e3.0.CO;2-2.

Yu, X., Taylor, A. M. W., Nagai, J., Golshani, P., Evans, C. J., Coppola, G., & Khakh, B. S. (2018). Reducing astrocyte calcium signaling in vivo alters striatal microcircuits and causes repetitive behavior. *Neuron*, *99*(6), 1170–1187.e1179. doi: 10.1016/j.neuron.2018.08.015.

Received: 13 October 2022 | Revised: 26 April 2023 | Accepted: 8 May 2023

DOI: 10.1002/glia.24388

GLIA

WILEY

RESEARCH ARTICLE

Early cortical oligodendrocyte precursor cells are transcriptionally distinct and lack synaptic connections

Natascha S. Vana[1,2] | Karen M. J. van Loo[2] | Ashley J. van Waardenberg[3] | Monika Tießen[1] | Silvia Cases-Cunillera[2] | Wenjing Sun[1] | Anne Quatraccioni[2] | Susanne Schoch[2] | Dirk Dietrich[1]

[1]Department of Neurosurgery, University Hospital Bonn, Bonn, Germany

[2]Department of Neuropathology, University Hospital Bonn, Bonn, Germany

[3]i-Synapse, Bioinformatics, Cairns, Australia

Correspondence
Dirk Dietrich, Department of Neurosurgery, University of Bonn Medical Center, Venusberg-Campus 1, D-53127 Bonn, Germany.
Email: dirk.dietrich@uni-bonn.de

Susanne Schoch, Department of Neuropathology, University of Bonn Medical Center, Venusberg-Campus 1, D-53127 Bonn, Germany.
Email: susanne.schoch@uni-bonn.de

Present addresses
Karen M. J. van Loo, Department of Epileptology and Neurology, RWTH Aachen University, Aachen, Germany; and Wenjing Sun, Department of Neuroscience, Wexner Medical Center, The Ohio State University, Columbus, Ohio, USA.

Funding information
Deutsche Forschungsgemeinschaft, Grant/Award Numbers: DI 853/3-5 & 7, SCHO 820/4-7, SPP1757

Abstract

Oligodendrocyte precursor cells (OPCs) generate oligodendrocytes, a process that may be tuned by neuronal activity, possibly via synaptic connections to OPCs. However, a developmental role of synaptic signaling to OPCs has so far not been shown unequivocally. To address this question, we comparatively analyzed functional and molecular characteristics of highly proliferative and migratory OPCs in the embryonic brain. Embryonic OPCs in mice (E18.5) shared the expression of voltage-gated ion channels and their dendritic morphology with postnatal OPCs, but almost completely lacked functional synaptic currents. Transcriptomic profiling of PDGFRα$^+$ OPCs revealed a limited abundance of genes coding for postsynaptic signaling and synaptogenic cell adhesion molecules in the embryonic versus the postnatal period. RNA sequencing of single OPCs showed that embryonic synapse-lacking OPCs are found in clusters distinct from postnatal OPCs and with similarities to early progenitors. Furthermore, single-cell transcriptomics demonstrated that synaptic genes are transiently expressed only by postnatal OPCs until they start to differentiate. Taken together, our results indicate that embryonic OPCs represent a unique developmental stage biologically resembling postnatal OPCs but without synaptic input and a transcriptional signature in the continuum between OPCs and neural precursors.

KEYWORDS
neuron glia synapse, NG2 cells, oligodendroglial lineage, OPC proliferation, transcriptomics

1 | INTRODUCTION

Oligodendrocytes are generated from oligodendrocyte precursor cells (OPCs). Accumulating evidence suggests that the process of oligodendrogenesis and myelination is guided by the electrical activity of neurons (Foster et al., 2019; Káradóttir & Kuo, 2016). It still is a major unresolved question if and how electrical activity of neurons could guide these processes and influence the proliferation of OPCs. In contrast to other glial cell types in the CNS, a unique and remarkable functional connection exists between neurons and OPCs: OPCs receive classical synapses from neurons in gray and white matter (Bergles et al., 2000; Haberlandt et al., 2011; Kukley et al., 2007;

Susanne Schoch and Dirk Dietrich contributed equally to this work

Ziskin et al., 2007) and vesicular release from neurons activates neurotransmitter receptors to depolarize OPCs (glutamate and GABA receptors) (Biase et al., 2010; Kukley et al., 2008; Lin & Bergles, 2003). Those synaptic depolarizations are translated into intracellular calcium signals (Sun et al., 2016) and intracellular calcium levels in turn have been shown to modulate proliferation and migration of OPCs/NG2 cells (Pitman et al., 2020; Zhao et al., 2021). Therefore, activity-dependent synaptic transmitter release is viewed as one candidate to guide the generation of new OPCs (Foster et al., 2019; Káradóttir & Kuo, 2016).

However, recent evidence supporting a role of neuronal activity in controlling the proliferation of OPCs is conflicting. While some studies have reported an increased generation of OPCs in the rodent CNS in response to neuronal activity (Gibson et al., 2014; Mitew et al., 2018), others have not observed this effect (Simon et al., 2011; Xiao et al., 2016).

OPCs (PDGFRα$^+$ and NG2$^+$) begin to appear in the dorsal embryonic forebrain around embryonic day (E) 16/17 (Kessaris et al., 2006; Nishiyama et al., 1996; Tognatta et al., 2017; Winkler et al., 2018). Embryonic OPCs, studied in the spinal cord and optic nerve, show the highest proliferative activity compared to postnatal stages (Calver et al., 1998; Gao & Raff, 1997; Van Heyningen et al., 2001). Therefore, if this strong proliferative activity is dependent on synaptic connections from neurons, synaptic input to embryonic OPCs should also be pronounced. Recently, Spitzer et al. (2019) reported that embryonic OPCs in the forebrain (E18, selected based on NG2-YFP expression) indeed already express functional glutamate receptors. However, it remained open whether embryonic OPCs are contacted by synapses which could activate those receptors.

To define the developmental timing of synaptic input to OPCs and to explore changes in the presence and abundance of synaptic components in OPCs, we performed a combined electrophysiological, morphological and transcriptional analysis of PDGFRα$^+$ and NG2$^+$ OPCs in the dorsal embryonic and postnatal forebrain. Our data show that the phenotype of embryonic OPCs is very closely related to postnatal OPCs in the dorsal cortex except that embryonic OPCs lack synaptic connections from neurons. The transcriptional analysis revealed that many synaptic genes are not yet expressed in embryonic OPCs and that the general transcriptional signature of embryonic OPCs is clearly distinct from their postnatal counterparts.

2 | MATERIALS AND METHODS

2.1 | Animals

NG2DsRedBAC (Tg(Cspg4-DsRed.T1)1Akik/J, kind gift from A. Nishiyama, UConn, USA) mice expressing the red fluorescent protein DsRed.T1 under the control of the NG2 (Cspg4) promoter were used for all analyses (Zhu et al., 2008). All efforts were made to minimize pain and suffering and to reduce the number of animals used, according to the ARRIVE guidelines. Mice were housed under a 12 h light–dark-cycle (light-cycle 7 am/7 pm), in a temperature (22 ± 2°C) and humidity (55 ± 10%) controlled environment with food/water ad libitum. All procedures were planned and performed in accordance with the guidelines of the University of Bonn Medical Centre Animal-Care-Committee as well as the guidelines approved by the European Directive (2010/63/EU) on the protection of animals used for experimental purposes. Embryonic NG2DsRedBAC mice were obtained by timed breeding, whereby mice were housed together for one day. The day of separation was counted as (gestational day) embryonic day (E) 0.5. For bulk and single-cell RNA sequencing of isolated OPCs C57BL/6NCrl (Charles River) mice of three (E16.5, P4, and P12) or two different ages (E16.5 and P5) were used, respectively.

2.2 | Brain slice preparation

NG2DsRedBAC mice were anesthetized using isoflurane and sacrificed by rapid decapitation.

Embryonic (E18.5) and postnatal ("P7", P7-8 and "P12", P12-14) mice of both sexes were used in electrophysiological experiments. The brain was quickly removed from the skull and placed in ice-cold and oxygenated high-sucrose dissection buffer containing (in mM): 87 NaCl, 2.5 KCl, 1.25 NaH_2PO_4, 7 $MgCl_2$, 0.5 $CaCl_2$, 25 $NaHCO_3$, 25 glucose, 75 sucrose (pH 7.4). Acute coronal brain slices of 300 µm (for electrophysiology) or 400 µm (for immunohistochemistry) were cut using a Leica VT 1200S (Leica Microsystems) vibratome while being immersed in the ice-cold dissection solution, transferred to an incubation chamber at 35°C for 25 minutes and subsequently stored at room temperature for at least 40 minutes before recording in the bath solution containing (in mM): 124 NaCl, 3 KCl, 1.25 NaH_2PO_4, 2 $MgCl_2$, 2 $CaCl_2$, 26 $NaHCO_3$, 10 glucose (pH 7.4).

For the preparation of embryonic brain slices pregnant damns were anesthetized and decapitated. Embryos were removed, decapitated and their heads were temporally kept in the ice-cold and oxygenated dissection buffer described above. For better visual guidance the brains of embryonic mice were isolated under a Zeiss Stemi 2000-C (Carl Zeiss Microscopy) stereomicroscope while being submerged in oxygenated dissection buffer. The head was held by a forceps attached to the frontal bone while a second forceps was used to strip the skin off the skull. Once the skull was exposed, the skull was broken open with a forceps and the brain eventually was scooped out with a small spatula. For the preparation of acute brain slices the embryonic brains were embedded in 4% super low melting agarose (Roth). Little agarose cubes each containing one brain were cut out and glued next to each other on the specimen tray of the vibratome where all embryonic brains were cut simultaneously into 300 µm thick slices.

2.3 | Immunohistochemistry

Acute brain slices (400 µm) of NG2DsRedBAC mice belonging to the age groups of P7-14, 4–7 weeks and 4–5 months were fixed in 8% PFA in PBS, pH 7.4, overnight at 4°C. For embryonic brains, the

cerebellum and the very frontal part of the brain were cut off and the remaining tissue was fixed in 4% or 8% PFA in PBS, pH 7.4, overnight. After three PBS washing steps (10 minutes each), the fixed brain tissue was embedded in 3% Agar in PBS, cut into 50 µm thick coronal brain sections and subsequently stored in TBS, pH 7.4. Some of the embryonic brains were cryopreserved in cryostorage glycol solution consisting of 1% Polyvinylpyrrolidone (PVP)-40, 30% sucrose and 30% ethylene glycol in 0.2 M phosphate buffer (pH 7.4) between fixation and re-sectioning. Incubations with primary and secondary antibodies were performed as described below with washing steps (three times TBS for 10 minutes at room temperature) in between. Brain sections were incubated overnight at 4°C with the respective primary antibody (rabbit anti-SV2B (Synaptic Systems, 1:500), rabbit anti-DsRed (Takara Bio, 1:500), rat anti-AN2 (Miltenyi, 1:500), rat anti-PDGFRα (BD Pharmigen, 1:100). Primary antibodies were diluted in TBS containing Triton X-100 at a concentration of 0.3% (SV2B, AN2, PDGFRα) or 0.1% (DsRed). For SV2B detection sections were incubated with the secondary antibody, biotinylated goat anti-rabbit IgG (Vector Laboratories, 1:167), for 3 hours at 35°C and then incubated with Alexa Fluor 488-conjugated Streptavidin (Jackson ImmunoResearch, 1:167) for another 3 hours at 35°C. All other primary antibodies were followed by incubation with either goat anti-rabbit RRX (Jackson Immuno Research, 1:167) or goat anti-rat Alexa Fluor 488 (Thermo Fisher Scientific, 1:167 for AN2 or 1:100 for PDGFRα) for 3 hours at 35°C. Secondary antibodies were diluted in TBS containing 0.3% Triton X-100. Finally, sections were incubated for 20 minutes with Hoechst 33342 (0.02 mg/mL in TBS) at room temperature and mounted on glass slides using Vectashield (Vector Laboratories). For each experiment, 4–6 sections of one animal from every age group were stained in parallel. In addition, negative controls, in which the primary antibody was omitted (2–3 sections per age group), were run for each of the experiment.

2.4 | Analysis of immunohistochemical stainings

SV2B fluorescence intensity in embryonic, postnatal, young adult and adult brain sections was assessed on an inverted epifluorescence microscope (Nikon Eclipse Ti). All samples of one experiment, that is, SV2B staining and negative control for each of the four age groups, were imaged on the same day. Image acquisition settings were kept constant throughout all age groups and all experiments. Three images per hemisphere were taken for all age groups and conditions. For the postnatal to adult age groups, neighboring non-overlapping imaging spots were chosen in the middle layer of the motor cortex (bregma: −1.3 to −2.5 mm) excluding auditory fields. Embryonic images were acquired in corresponding planes along the rostral-caudal axis but in the intermediate zone, where also the electrophysiological recordings were conducted.

The mean fluorescence intensity of all images was assessed using Fiji (Schindelin et al., 2012) and the fluorescence intensity of the negative control was subtracted from the intensity of slices stained with SV2B.

To test for the co-localization between DsRed and AN2 as well as between DsRed and PDGFRα in embryonic NG2DsRedBAC mice, confocal images were acquired on a Nikon A1 confocal microscope and subsequently analyzed in Fiji.

2.5 | Slice electrophysiology

Electrophysiological recordings were performed at room temperature (18°C) on an Olympus BX51WI microscope which is part of a Prairie Technologies Ultima Multiphoton Microscopy System (Bruker) equipped with two Chameleon Vision II lasers (Coherent). OPCs were patch-clamped in whole-cell recording mode using borosilicate glass pipettes (4–6 MΩ, pulled using a Narishige PP-830 puller) filled with an intracellular solution containing (in mM): 125 K-gluconate, 2 $MgCl_2$, 3 NaCl, 20 KCl, 4 Na_2ATP, 10 Hepes, 0.5 EGTA and 0.1% Lucifer Yellow. In brain slices derived from embryonic mice (E18.5), OPCs of the intermediate zone were targeted, while in the two postnatal groups (P7 and P12) OPCs located in the cortex were recorded. mPSCs were recorded at room temperature in voltage-clamp mode in the presence of 1 µM Tetrodotoxin (TTX, for all but two E18.5 OPCs) and 100 µM Ruthenium Red, filtered at 1 kHz and sampled at 20 kHz using a HEKA EPC 10 patch-clamp amplifier (including the Humbug filter). Cells were held at −85 mV and recorded using the Patchmaster software (HEKA Elektronik). mPSCs were recorded between 5 and 12 minutes after Ruthenium Red and TTX application for a total duration of 200–300 s per cell for all age groups, except for two cells within each group which could be recorded only for 120 s and 175 s (E18.5), 95 s and 174 s (P7) and 160 s and 180 s (P14). Analysis of spontaneous vesicle release was conducted in Axograph X (Axon Instruments), which detected mPSCs semi-automatically using a sliding template with the function f(t) = exp (−t/Rise) − exp (−t/Decay) and the following parameters: Rise = 1 ms, Decay = 4 ms, 10 ms pre-event baseline plus 4 ms event duration (total duration of template 14 ms). All other electrophysiological data were analyzed using Igor Pro software (WaveMetrics).

2.6 | OPC isolation via magnetic-activated cell sorting (MACS) and RNA extraction

OPCs were isolated from whole brains of C57BL/6NCrl mice at E16.5, P4 and P12 using a Neural Tissue Dissociation Kit (Miltenyi Biotec). 5 samples per age group were used for RNA analysis, whereby the P12 group consisted of one P11 and four P12 samples. To collect sufficient cells for each of the 5 biological replicates per age group, we pooled multiple mouse brains for each of the time points: 4–6 for E16.5, 2 for P4 and 2 for P12. Brains were collected in Hank's Balanced Salt Solution (HBSS) and tissue was dissociated into cells by using the Neural Tissue Dissociation Kit (following manufacturer's instructions). Briefly, tissue was transferred to a gentleMACS C tube containing pre-heated enzyme mix 1. After an incubation period of 5 minutes at 37°C brains were roughly dissociated using a 5 mL

pipette and enzyme mix 2. Samples were further dissociated using the automated gentleMACS Octo Dissociator (Miltenyi Biotec). The dissociated tissue was filtered with a 70 µm cell strainer first, followed by a second filtration with a 40 µm cell strainer, and washed in between with DMEM. The resulting cell suspension was centrifuged at 1000*g* for 10 minutes, the pellet resuspended in DMEM containing 1% horse serum (DMEM/HS) and centrifuged again. The washed pellet was resuspended in DMEM/HS and OPCs were labeled by incubating the cell suspension with CD140a MicroBeads (Miltenyi Biotec) for 15 minutes at 4°C. The cells were washed with 20 mL DMEM/HS and centrifuged again. Subsequently, the cell pellet was resuspended in DMEM/HS at a ratio of 500 µL buffer per 1×10^7 cells. The cell suspension was then loaded on a MS column (Miltenyi Biotec) and placed in a magnetic cell separator (Miltenyi Biotec). To isolate $CD140a^+$ cells, first unbound cells were removed by 3 washing steps with 500 µL washing buffer and then the $CD140a^+$ cells were eluted with 1 mL elution buffer. All samples were frozen in liquid nitrogen and stored at −80°C before RNA extraction. To verify the specificity of this purification procedure, aliquots of eluted cells derived from a NG2DsRedBAC mouse (P7) were placed on a coverslip and checked in an inverted epifluorescence microscope (Nikon Eclipse Ti) for fluorescence labeling.

2.7 | Library preparation and sequencing using Smart-Seq2 for bulk RNA-sequencing (RNA-seq)

Total RNA was isolated using the miRNeasy mini kit (Qiagen) according to the manufacturer's instructions. RNA integrity and concentration were determined using the RNA assay on a Tapestation 4200 system (Agilent). Library preparation was based on the Smart-Seq2 protocol (Picelli et al., 2014): 5 ng total RNA (in 1 µL) was added to 4.5 µL Guanidine buffer (50 mM Guanidine Hydrochloride, 17.4 mM dNTPs, 2.2 µM SMART dT30VN primer). Smart-Seq2 libraries were generated on a Tecan Freedom EVO and Nanodrop II (BioNex) system. In short, RNA was incubated at 95°C for 3 minutes. 6 µL RT mix containing SuperScript II buffer (Invitrogen), 9.3 mM DTT, 370 mM Betaine, 15 mM $MgCl_2$, 50 U SuperScript II RT (Invitrogen), 10 U recombinant RNase Inhibitor (Takara) and 3.3 µM template-switching oligo was aliquoted to each sample using a Nanodrop II liquid handling system (BioNex) and incubated at 42°C for 90 minutes and 70°C for 15 minutes. 15 µL preamplification mix containing KAPA HiFi HotStart ReadyMix and 0.1 µM ISPCR primers was added to each sample and full-length cDNA was amplified for 12 cycles. cDNA was purified with 1X Agencourt AMPure XP beads (Beckman Coulter) and eluted in 14 µL nuclease-free water. Concentration and cDNA fragment size distribution was determined using a High Sensitivity D5000 assay for the Tapestation 4200 system (Agilent). cDNA was diluted to an average of 200 pg/µl and 100 pg cDNA from each sample was tagmented by adding 2 µL TD and 1 µL ATM from the Nextera XT DNA Library Preparation Kit (Illumina) to 1 µL diluted cDNA. The tagmentation reaction was incubated at 55°C for 8 minutes before removing the Tn5 from the DNA by adding 1 µL NT buffer. 1 µL indexing primer mix from Nextera XT Index Kit v2 Set A and 3 µL NPM was added and the tagmented cDNA was amplified for 14 cycles according to the manufacturer's specifications. PCR products were purified with 1X Agencourt AMPure XP beads (Beckman Coulter). The fragment size distribution was determined using a High Sensitivity D5000 assay for the Tapestation 4200 system (Agilent) and library concentration was determined using a Qubit dsDNA HS assay (Thermo Fischer). Libraries were clustered at 1.4 pM concentration using High Output v2 chemistry and sequenced on a NextSeq500 system (Illumina) SR 75 bp with 2*8 bp index reads.

2.8 | Bioinformatic analysis for bulk RNA-seq

Sequencing data were demultiplexed using bcl2fastq2 v2.20 and aligned to the mouse reference transcriptome mm10 from UCSC by kallisto v0.44.0 using default parameters. Raw counts were imported using tximport function from the tximport package and DESeqDataSetFromTximport function from DEseq2 and rlog transformed according to DEseq2 pipeline. DESeq2 was used to calculate normalized counts for each transcript using default parameters. All normalized transcripts with a maximum over all row mean lower than 10 were excluded resulting in 15,059 present transcripts. Group-wise comparisons of the three different times (E17.5, P4 and P12) were conducted using the Degust: Interactive RNA-seq analysis Version 3.2.0 (v.4.1.4) platform (http://degust.erc.monash.edu/) with voom/limma and adjusted for multiple testing using the Benjamini-Hochberg False Discovery Rate (FDR) method. Volcano plots were generated to visualize the differentially expressed genes of each comparison (FDR <0.05 and fold change >1.5).

2.9 | Deconvolution analysis of bulk RNA-seq with single-cell sequencing data

Deconvolution of our RNA-seq data to infer single-cell (SC) population state (or cell abundances) was performed using the CPM (Cellulation Population Mapping) algorithm (Frishberg et al., 2019) implemented in scBio v0.1.6. Inputs to the CPM function of scBio were as followed: "BulkData" (our RNA-seq data) were the normalized to counts per million (cpm) using the "cpm" function of edgeR v3.32.1 with defaults settings; "SCData" (single-cell input data) were log normalized, scaled and centered counts using the "NormalizeData" and "ScaleData" functions of Seurat v4.0.3 (Hao et al., 2021) with default arguments; "cellSpace," was the tSNE coordinates generated by Marques et al. (2018); "SCLabels," were the names of clusters identified by Marques et al.; and, "calculateCI" was set to "TRUE." Input data were limited to the genes that were present in both the RNA-seq and scRNA-seq data sets. Uniform Manifold Approximation and Projection (UMAP) dimensionality reduction (Marques et al., 2018) was performed using the RunUMAP function from Seurat, with arguments "reduction" set to "pca" and "dims" as 1:20, where the input data was the Principle Component Analysis (PCA) performed using the RunPCA function. Cell trajectory

was inferred using the predicted cell population states returned from scBio for each individual replicate to the mean of the P12 predicted cell population states. Distance was then calculated as 1-correlation, where the correlation method used was "spearman." Single-cell transcriptome counts, metadata and tSNE coordinates were downloaded from the UCSC Cell Browser on 22 July 2021: https://cells.ucsc.edu/?ds=oligo-lineage-dev. All analyses were performed using RStudio Server v1.4.1106, running R v4.0.5.

2.10 | Gene ontology annotation and enrichment analysis

General gene ontology (GO) analysis was performed with GOrilla (Eden et al., 2009) using differentially expressed genes as the target list, which contained up- and down-regulated genes, and the entire list of annotated genes as the background list. Ontology terms were selected based on Cellular Component. GO terms were considered statistically enriched when FDR q-value <0.05.

Synaptic Gene Ontologies were obtained using the SynGO software (Koopmans et al., 2019). Here, the target lists were the differentially up-regulated genes and the background lists the brain expressed genes from the SynGO database. SynGO terms were considered statistically enriched when FDR q-value <0.05. Heatmapper (Babicki et al., 2016) was used to generate heatmaps of the Log_2 median DESeq2 normalized counts of the various subgroups.

2.11 | Neuron isolation and cell sorting

For isolation of cortical pyramidal neurons, mice were in utero electroporated with plasmids expressing hrGFP at E14.5. At P33-35 cortical areas with green fluorescent cells were micro-dissected from 300 µm-thick coronal brain sections under an epifluorescence microscope (Zeiss Axio Observer A1), collected in ice-cold DPBS and dissociated using the Adult Tissue Dissociation Kit (Miltenyi Biotec). Enzymatic cell dissociation by papain was supported by mechanic dissociation using a gentleMACS Octo Dissociator (Miltenyi Biotec). The cell suspension was filtered through a 70 µm cell strainer and washed with DPBS, followed by a debris removal step. After rewashing the cells with DPBS, red blood cells were removed and the final cell pellet was resuspended in 1 mL of HBSS. Prior to fluorescence-activated cell sorting (FACS), 1 µL of 10 µg/mL DAPI was added to the cell suspensions. Cells that were positive for hrGFP and negative for DAPI were sorted using an Aria Cell sorter III (BD Biosciences) and collected in 1 mL of QIAzol. RNA isolation and sequencing was performed as described above.

2.12 | OPC isolation via MACS for single-cell RNA-seq

For scRNA-seq OPCs were isolated from E16.5 and P5 C57BL/6N mice ordered from Charles River as timed breedings. The E16.5 group consisted of the developing neocortices (neopallial cortex, intermediate zone and ventricular zone) (Chen, Chen, et al., 2017) of a total of 10 embryos (5 embryos of 2 dams each), which were dissected out from coronal brain sections using a Leica M165 FC stereomicroscope. For the P5 group isocortices of six mice (three pups of two different dams) were pooled. Brain tissue was collected in HBSS kept on ice until further processed for OPC isolation. Tissue was dissociated into cells by using the Neural Tissue Dissociation Kit (following manufacturer's instructions). Samples were further dissociated using the automated gentleMACS Octo Dissociator (Miltenyi Biotec). The dissociated tissue was filtered using a 70 µm cell strainer and DMEM was used to wash the samples. The obtained cell suspension was centrifuged at 300*g* for 10 minutes and after discarding the supernatant, the pellet was resuspended in DMEM containing 1% horse serum (DMEM/HS) and centrifuged again. The resulting pellet was resuspended in DMEM/HS containing CD140a MicroBeads (Mitenyi Biotec) and incubated for 15 minutes at 4°C. After washing with DMEM/HS, samples were centrifugated again and the pellet was resuspended in DMEM/HS before applying the solution through an MS column (Miltenyi Biotec), placed in a magnetic cell separator (Miltenyi Biotec). The column was washed three times with DMEM/HS to eliminate the unbound cells and $CD140a^+$ cells were eluted with a plunger by placing the MS column (Miltenyi Biotec) in a 15 mL falcon. The samples were finally centrifugated at 300*g* for 10 minutes and resuspended in 100 µL DMEM/HS buffer.

2.13 | Library preparation and single-cell RNA-seq

Upon quality control on the Countess Automated Cell Counter (Thermo Fisher), the resulting cell suspensions ($CD140a^+$) were loaded directly to a Chromium Single-Cell 3´GEM Instrument (Chromium Next GEM Chip G Single-Cell Kit, 10X Genomics). Corresponding libraries were generated with the Chromium Next GEM Single-Cell 3′ GEM Library & Gel Bead Kit v3.1 employing the Dual Index Kit TT Set A (10X Genomics) according to the manufacturer's instructions. Libraries were produced from 1000 cells per sample. Sequencing of the final Single-Cell RNA libraries was performed using an SP 100 flow cell (600-800 M reads) (Illumina Inc) on an Illumina NovaSeq 6000 platform, aiming at a minimum sequencing depth of 150 000 reads per cell.

2.14 | Analysis of single-cell RNA-seq data

Mapping of RAW single-cell RNA sequencing data was performed using Cell Ranger version 6.1.2 (Zheng et al., 2017). The primary DNA assembly sequences and GTF transcriptome was downloaded from Ensembl release 105 (GRCm39) for Mus musculus (http://ftp.ensembl.org/pub/release-105/). The transcriptome GTF file was filtered for protein-coding genes and a reference assembly prepared using the cellranger "mkref" subcommand. Fastq files of the raw sequencing data for each sample were input into the cellranger

"count" subcommand for alignment of RNA-seq reads and assignment of barcodes to cells. Raw feature count matrices generated by Cell Ranger were imported into R (version 4.0.5) as a SeuratObject using the "CreateSeuratObject" function (Seurat version 4.0.2) using default parameters (Hao et al., 2021). DropletUtils (version 1.10.3) (Griffiths et al., 2018; Lun et al., 2019) was used to infer which barcodes belonged to intact cells versus ambient background after reading in 10X count data using the "read10xCounts" function. emptyDroplets "by.rank" parameter was set to 1200 as an approximation of expected input cell counts and "niters," the number of permutations for determining statistical significance was set to 100,000. Cells with an FDR ≤ 0.01 were retained as intact cells for further analysis.

Single cells were then initially retained if the number of genes detected "nFeature_RNA" was ≥ 250 and ≤ 8000, percentage of reads mapped to mitochondria genes ≤ 40, percentage of reads mapped to ribosomal genes ≤ 20. Features retained were required to be detected in at least 3 cells. Mitochondrial and ribosomal read count percentages were calculated using the "PercentageFeatureSet" function of Seurat to determine the percentage of reads that mapped to "MT-*" and "RPS* or RPL*" genes, respectively. Doublet filtering was performed using DoubletFinder version 2.0.3 (McGinnis et al., 2019) on each filtered single-cell data set (E16.5, P5) to remove multiplets, with an expected doublet rate of 0.6% of 1200 cells and parameters pN = 0.25, pK = 0.09, using 30 principal components. Remaining E16.5 and P5 single cells were then merged into a single Seurat object and log-normalized (using the Seurat "NormalizeData" function). The top 2000 most variable features were obtained using the "FindVariableFeatures" function for subsequent Principal Component Analysis (PCA) dimensionality reduction ("RunPCA") on the first 30 principal components, followed by UMAP generation ("RunUMAP") using the prior PCA reductions. Nearest-neighbor graphs were constructed using "FindNeighbors" on the PCA reductions and clusters determined using "FindClusters" at a resolution of 0.6. Four small and far-scattered clusters were then removed from the analysis. Cells retained were then required to have a percentage of mapped reads to mitochondrial genes less than the upper quantile (29.86%) before removal of mitochondrial genes, filtering of features for detection in at least 3 cells and re-normalization as outlined above. For final dimensionality reduction, the top 1000 most variable features were used, 30 principle components used and the neighborhood size parameter of RunUMAP set to 100 ("n. neighbors"). 1548 cells and 13,612 features (genes) remained after the final filtering, comprised of 562 E16.5 and 986 P5 cells.

2.15 | Integration of single-cell RNA-seq data

Marques et al., 2018 single-cell count data and metadata were downloaded as described for single-cell deconvolution. Genes detected in our single-cell data or features detected in at least 3 cells were retained (a total of 1956 cells). Marques and our combined single-Cell data UMI count data (3504 cells) were then normalized together by regularized negative binomial regression to account for differences in UMI depth (implemented in the "SCTransform" method of Seurat) (Hafemeister & Satija, 2019). Integration of our data with Marques followed to approximate our cell neighborhood locations with Marques cells (Stuart et al., 2019). The top 2000 variable features ("SelectIntegrationFeatures") were input to "PrepSCTIntegration," followed by "FindIntegrationAnchors" to identify pairwise cells within each other's neighborhood, followed by "IntegrateData" using the identified anchor cells, with "normalization.method" set to "SCT." PCA ("RunPCA") on the first 30 principal components was followed by UMAP generation ("RunUMAP") using the prior PCA reduction with a neighborhood size set to 200 ("n.neighbors"). Integration with Marques identified multiple E16.5 clusters. To resolve these clusters in our E16.5/P5 data set, shared nearest-neighbor graphs were constructed using the "FindNeighbors" function on the PCA reductions exploiting the additional information in the integrated data for our E16.5/P5 cells only and then clusters determined using "FindClusters" at a resolution of 1.1, identifying a total of 10 clusters. For the analysis of the expression of synaptic proteins integrated data was assessed using 140 curated genes (Supp. Table 3). Of the 140 genes, 138 genes were detected in the integrated single-cell data. "PercentageFeatureSet" function of Seurat (with parameter assay = RNA) was used to determine the percentage of reads that mapped to these 138 genes.

2.16 | Data analysis

Data are shown as means ± standard errors of the mean (SEM) unless stated otherwise, n denotes the number of cells unless stated otherwise. Statistical analyses were performed with GraphPad Prism (GraphPad Software). For comparisons of two groups statistical significance was determined using an unpaired, two-tailed t-test. When there were more than two groups a one-way ANOVA in conjunction with a post-hoc Tukey's test was conducted. Values were considered significant if $p < .05$, indicated by asterisks in the figure.

3 | RESULTS

We and others have shown that daughter OPCs inherit synaptic contacts from the mother cell during cell division in the first postnatal week (Ge et al., 2009; Kukley et al., 2008). However, the time point when OPCs start acquiring functional synaptic contacts during development is still unresolved. In rodents, OPCs emerge within the embryonic dorsal cortical plate around E16-17 (Kessaris et al., 2006; Nishiyama et al., 1996; Tognatta et al., 2017; Winkler et al., 2018). To examine whether OPCs are surrounded by synapses during prenatal development, we first immuno-labeled coronal mouse brain slices with a marker for neuronal glutamatergic synaptic vesicles (SV2B) (Stout et al., 2019) (Figure 1a–c). In E18.5 brains we found the synaptic marker SV2B to be expressed in the intermediate cortical layer where OPCs first appear (Tognatta et al., 2017) (Figure 1a–c, E18.5: 27.9 ± 1.5 a.u. vs. P7-14: 95.4 ± 9.2 a.u. versus 4–7 weeks: 115.5 ± 9.4 a.u. vs. 4–5 months: 121.5 ± 6.1 a.u. [$n = 4$]).

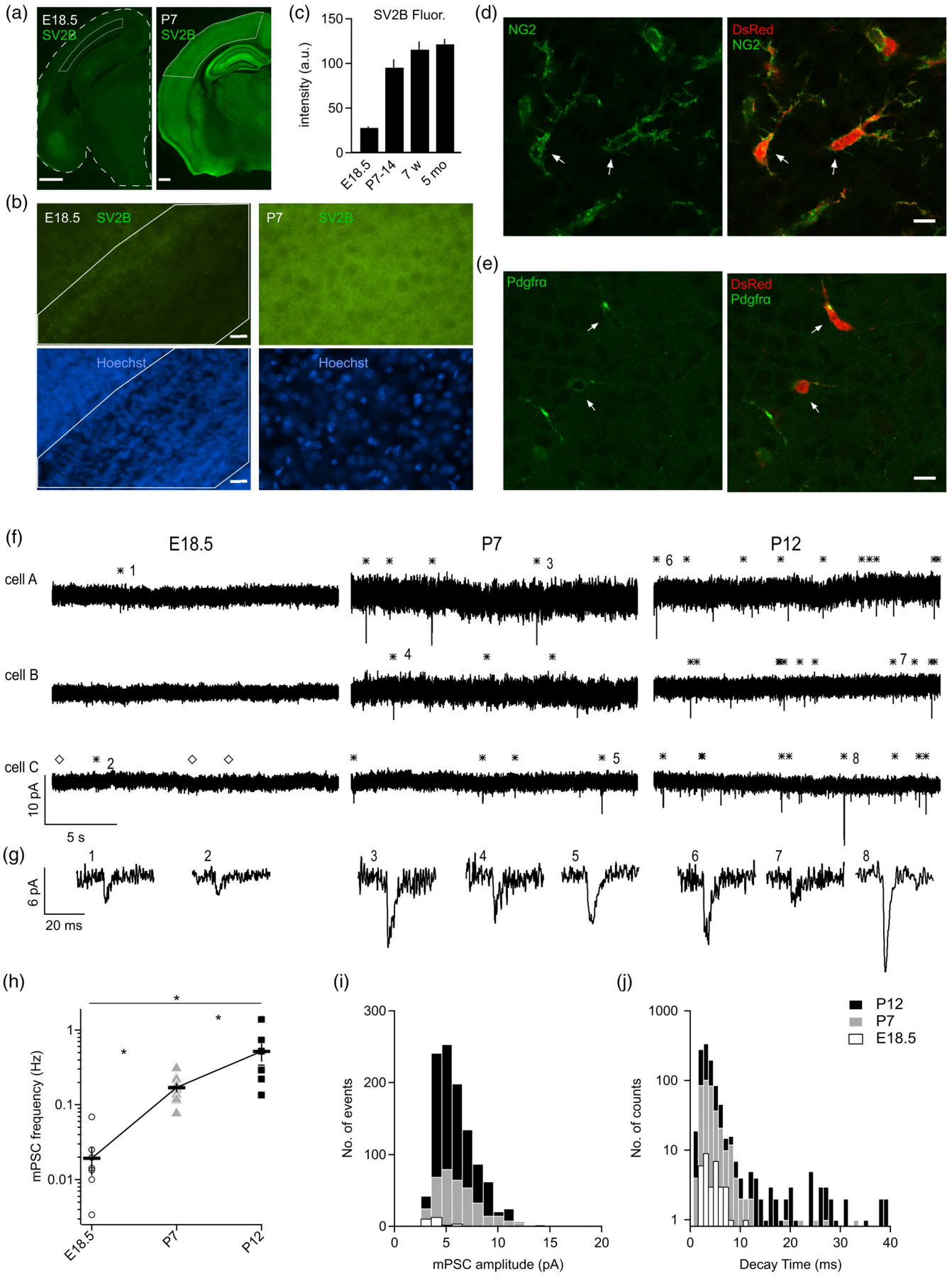

FIGURE 1 Legend on next page.

To investigate whether OPCs form functional synaptic contacts with neurons as early as E18, we patch-clamped DsRed-expressing cells in acute brain slices of NG2DsRedBAC mice which express DsRed solely in OPCs (Biase et al., 2010; Zhu et al., 2008; Ziskin et al., 2007). Co-immunolabeling of E18.5 brain slices with DsRed and NG2 or PDGFRα, the two main marker proteins for OPCs (Nishiyama et al., 1996; Pringle & Richardson, 1993), validated the specific labeling of OPC by DsRed. We found that >95% of parenchymal DsRed+ cells were also positive for NG2 (Figure 1d) and PDGFRα (Figure 1e) and >93% of NG2 cells were marked by the DsRed transgene indicating that E18.5 NG2DsRedBAC mice were well suited to identify embryonic OPCs. Patched cells were held at −85 mV and perfused with 1 μM TTX and 100 μM Ruthenium Red (see methods) to block action potentials and to enhance spontaneous vesicle release downstream of calcium entry (Trudeau et al., 1996), respectively. Using this protocol, we previously measured spontaneously occurring synaptic currents in almost all OPCs tested (Kukley et al., 2007, 2008, 2010). In contrast, OPCs in the intermediate cortical layer at E18.5 appeared virtually silent and no synaptic currents could be detected by eye (Figure 1f, left). Under the same conditions spontaneous synaptic currents were readily observed at postnatal stages, P7-8 (P7) and P12-14 (P12) (Figure 1f, middle and right). With the help of a template-based detection algorithm a low frequency of small miniature postsynaptic currents (mPSCs) could be identified in 9 of 10 cells in the embryonic group (Figure 1f–i, E18.5: 0.02 ± 0.01 Hz [$n = 8$]). The same algorithm detected an order of magnitude more frequent synaptic currents in OPCs of the neocortex of postnatal mice at both P7 and P12 (Figure 1f–i, P7: 0.17 ± 0.02 Hz ($n = 9$); P12: 0.52 ± 0.14 Hz ($n = 8$); E18.5 vs. P7 $p < .05$, E18.5 vs. P12 $p < .05$, P7 vs. P12 $p < .05$, one-way ANOVA with post-hoc Tukey's test). mPSCs in embryonic OPCs were not only very rare but also substantially smaller than in OPCs of both postnatal groups and rarely exceeded 5 pA (Figures 1i and 3.6 ± 0.3 pA for E18, 5.9 ± 0.2 pA and 5.3 ± 0.1 pA at P7 and P12, respectively). In contrast, the decay of mPSCs was comparable in all groups: the largest fraction of currents decayed fast with time constants <10 ms (Figure 1j, E18.5: 3.6 ± 0.3 ms vs. P7: 3.3 ± 0.1 ms and P12: 2.9 ± 0.1 ms). In the P7 and P12 groups smaller fractions of 2%–3% showed decay times longer than 10 ms (P7: 18.8 ± 2.7 ms and P12: 22.6 ± 2.7 ms). In the E18.5 group only one slowly decaying event was recorded (Figure 1j). The fast and slowly decaying currents likely represent glutamatergic and GABA-ergic currents, respectively (Bergles et al., 2000; Kukley et al., 2008; Zonouzi et al., 2015), implying that the depolarizing synaptic input to embryonic and postnatal OPCs arises largely from glutamatergic neurons.

We next asked whether the mPSC frequency correlates with the complexity of the dendritic architecture of OPCs. To compare the morphology of OPCs in the intermediate zone of E18.5 mice and the neocortex of P7-14 mice, we included a tracer in the pipette solution and scanned patched OPCs using two-photon microscopy in acute slices after recording (Figure 2a–f). The dendritic tree of OPCs recorded from E18.5 mice occupied a substantially smaller area than that of postnatal OPCs (Figure 2g, E18.5: 1654 ± 133.66 μm^2 [$n = 10$] vs. P7: 4155 ± 533 μm^2 [$n = 8$] $p < .05$; E18.5 vs. P12: 4829 ± 677 μm^2 [$n = 10$] $p < .05$; P7 vs. P12 $p > .05$, one-way ANOVA with post-hoc Tukey's test). Tracing of individual dendrites in 3D two-photon image stacks showed that in embryonic OPCs also the total dendritic length was profoundly shorter (Figure 2h, E18.5: 527 ± 46 μm vs. P7: 1944 ± 126 μm $p < .05$ and E18.5 vs. P12: 2214 ± 278 μm $p < .05$; P7 vs. P12 $p > .05$, one-way ANOVA with post-hoc Tukey's test) and the branching pattern more simplified (Figure 2i) when compared to postnatal stages. While the mPSC frequency does positively correlate with the size of the dendritic tree (Figure 2j, E18.5 [$n = 8$], P7 [$n = 6$], P12 [$n = 8$], $r = 0.6232$, $r^2 = 0.3884$, $p < .05$, Pearson correlation coefficient), the shorter total dendritic length alone cannot explain the very low frequency of synaptic currents observed in embryonic OPCs as the event rate per mm of dendrite length was also significantly smaller in the embryonic group (Figure 2k, E18.5: 0.04 ± 0.01 events/[s*mm] [$n = 8$] vs. P7: 0.09 ± 0.01 events/[s*mm] [$n = 9$] $p < .05$, E18.5 vs. P12: 0.23 ± 0.06 events/[s*mm] [$n = 8$] $p < .05$, P7 vs. P12 $p < .05$, one-way ANOVA

FIGURE 1 OPCs in the embryonic mouse brain almost lack synaptic input. (a) Representative epifluorescence images of immunohistochemical staining against the synaptic vesicle marker SV2B in coronal brain sections of NG2DsRedBAC mice at E16.5 and P7-14. Regions of interest (outlined by light gray traces) were used for fluorescence intensity measurement, that is, intermediate zone for brain slices from embryonic mice and neocortex for postnatal age groups. Scale bars = 500 μm. (b) Dual channel fluorescence images (SV2B and Hoechst) acquired with a higher power objective illustrating the region (left, white line, right entire image) defined for quantitative analysis. Scale bar = 20 μm. (c) Quantification of the mean SV2B fluorescence intensity of different age groups. $n = 4$ mice for each age group. Error bars represent SEM. (d and e) Colocalization of DsRed and the OPC marker proteins NG2 or PDGFRα in coronal E18.5 NG2DsRedBAC mouse brain slices. DsRed immunoreactive cells (red) in the intermediate zone at E18.5 also expressed the NG2 protein (green). Furthermore, DsRed positive cells (red) were also co-labeled with PDGFRα (green), validating that DsRed marks embryonic OPCs in the NG2DsRedBAC transgenic line. White arrows in each panel indicate OPCs. Scale bars = 10 μm. (f and g) Representative voltage-clamp recordings of OPCs in the mouse cortex from different developmental ages in the presence of 1 μM TTX and 100 μM Ruthenium Red. Asterisks indicate synaptic events; numbers label corresponding events shown in detail in (g). Note that synaptic currents at E18.5 were extremely rare. White diamonds denote positions at which single data points were deleted to remove high-frequency noise in low-frequency recordings. (h) The frequency of spontaneous mPSCs in E18.5 (white circle, $n = 10$) and P7 OPCs (gray triangle, $n = 10$) is lower than in P12 OPCs (black squares, $n = 8$, E18.5 vs. P7 $p < .05$, E18.5 vs. P12 $p < .05$, P7 vs. P12 $p < .05$, one-way ANOVA with post-hoc Tukey's test). (i) Histogram of the mPSC amplitudes recorded in E18.5 (white), P7 (gray) and P12 (black) OPCs. Overall mPSCs from E18.5 OPCs showed much smaller amplitudes than currents recorded postnatally. (j) The histogram of the decay times illustrates a similar distribution between OPCs of embryonic and postnatal mice indicating that the shape of the events is comparable between the three age groups.

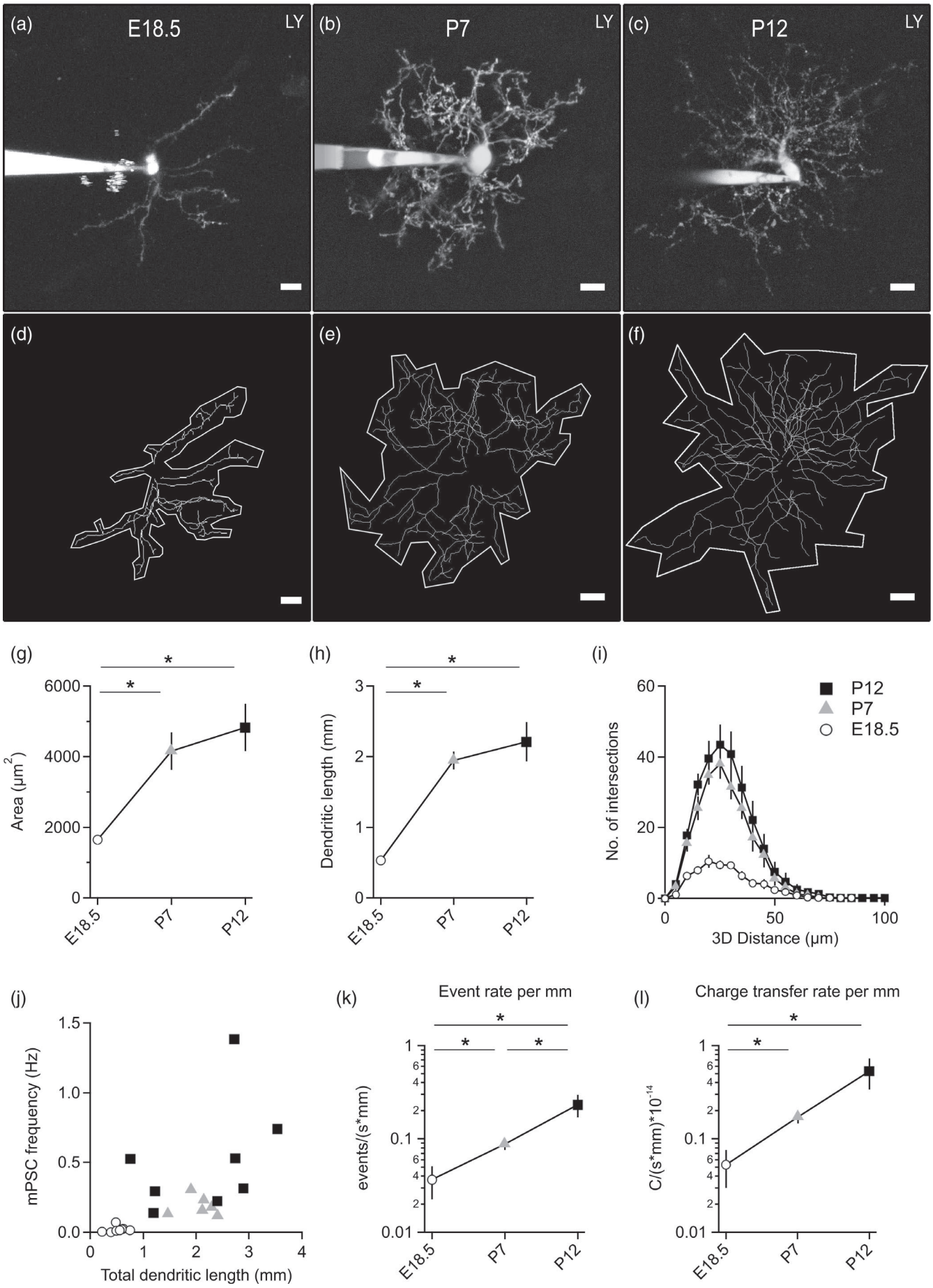

FIGURE 2 Legend on next page.

with post-hoc Tukey's test). This low level of functional synaptic input onto embryonic OPCs becomes most apparent when also taking into account the lower amplitude and the predominantly fast decay of their synaptic currents showing that also the charge transfer rate per mm of dendrite length is significantly smaller (Figure 2l, E18.5: 0.06 ± 0.02 $*10^{-14}$ C/(s*mm) ($n = 8$) vs. P7: 0.17 ± 0.02 $*10^{-14}$ C/(s*mm) ($n = 9$) $p < .05$, E18.5 vs. P12: 0.53 ± 0.19 $*10^{-14}$ C/(s*mm) ($n = 8$) $p < .05$, P7 vs. P12 $p > .05$, one-way ANOVA with post-hoc Tukey's test).

We previously reported that electrical properties of postnatal OPCs play an important role for synaptic signal integration (Sun et al., 2016). Therefore, we next asked what the passive electrical properties of E18.5 OPCs are and whether they might be equipped with a similar set of voltage-gated ion channels or even a more excitable one to compensate for the weak synaptic innervation described above. The resting membrane potential (RMP) in OPCs was measured ~10 mV more depolarized at E18.5 than at P7 implying that the ion permeability ratio at resting potential is shifted toward depolarizing forces in embryonic OPCs (Figure 3a, E18.5: −65.7 ± 4.2 mV [n = 10] vs. P7: −81.5 ± 2.3 mV [$n = 10$] $p > .05$, Student's t-test, P12: −85.4 ± 1.6 mV [$n = 7$]). If passive electrical properties per unit of OPC membrane were similar across age groups, cell capacitance (Cm) and membrane resistance (Rm) would be expected to scale with the size of the dendritic tree and the cell's surface area. This was clearly observed for the Cm where the value of the P7 group similarly exceeded the E18.5 value, as did the total dendritic length (Figure 3b, E18.5: 12 ± 2.6 pF ($n = 10$) vs. P7: 40 ± 3.3 pF ($n = 11$) $p < .05$, Student's t-test, P12: 44.6 ± 3.7 pF ($n = 10$); total dendritic length is roughly proportional to the cell's surface area). In contrast, the Rm was very similar between age groups (Figure 3c, E18.5: 1.40 ± 0.23 GΩ ($n = 10$) vs. P7: 1.23 ± 0.41 GΩ ($n = 11$) $p > .05$, Student's t-test, P12: 49.2 ± 5.3 MΩ ($n = 10$)), indicating that E18.5 OPCs express substantially more un-gated potassium channels per surface area than postnatal ones in order to display the same Rm with a smaller surface area.

Voltage steps applied during voltage clamp recordings activated large transient and persistent outward currents in all age groups (Figure 3d,e), which were previously shown to represent A- and DR-type of potassium channels (Maldonado et al., 2013; Sun et al., 2016; Yuan et al., 2002). At the beginning of the depolarization, we identified a small transient inward current which resembled a TTX-sensitive current as previously described (Figure 3d,e) (Biase et al., 2010; Xie et al., 2007), which usually is too small to generate action potentials (Berret et al., 2017; Biase et al., 2010; Chittajallu et al., 2004; but see Káradóttir et al., 2008; Xie et al., 2007). A-type potassium currents (Figure 3f, at 40 mV E18.5: 1.10 ± 0.13 nA ($n = 8$) vs. P7: 1.79 ± 0.15 nA ($n = 5$) $p < .05$, Student's t-test) appeared reduced in E18.5 OPCs compared to postnatal OPCs, while DR-type potassium channels (Figure 3g, at 40 mV E18.5: 684 ± 63 pA ($n = 8$) vs. P7: 936 ± 146 pA ($n = 5$) $p > .05$, Student's t-test) and voltage-activated sodium currents (Figure 3h, at 0 mV E18.5: −103 ± 17 pA (n = 8) vs. P7: −204 ± 55 pA ($n = 5$) $p > .05$, Student's t-test) were found at similar levels. Whether or not an EPSP or IPSP would be enhanced by activating sodium channels also depends on the strength of rapidly activating potassium currents. To compare the excitability of OPCs across age groups, we calculated a ratio of the amplitudes of sodium and A-type currents recorded between −40 and 0 mV, a potential beyond the threshold for sodium channel activation. E18.5 cells showed a similar excitability index when compared to P7 (Figure 3i, mean I_{Na}/mean Peak I_K between −40 and 0 mV, E18.5: 0.23 ± 0.05 ($n = 8$) vs. P7: 0.24 ± 0.09 ($n = 5$) $p > .05$, Student's t-test).

Our findings so far show that embryonic OPCs display a substantially reduced synaptic input drive although synapses seem to be present in their neighborhood. To assess the possibility that embryonic OPCs may be too immature to receive and establish synaptic connections, we compared the molecular signatures between embryonic and postnatal OPCs. OPCs were immuno-isolated from the whole mouse brain at E16.5, P4, and P12 by anti-PDGFRα-mediated magnetic activated cell sorting (MACS, yielding at least 90% purity of $NG2^+$ cells, see methods) and subjected to bulk RNA sequencing (RNA-seq) (Figure 4). The principal component analysis (PCA) of the data set showed that the biological replicates of the different time points clustered together and that the molecular signatures of all time points were clearly different from each other, indicating pronounced developmental changes (Figure 4a). The expression at P4 of a panel of representative marker genes for different brain cell types was consistent

FIGURE 2 Embryonic OPCs have a reduced morphological size and complexity compared to OPCs in the postnatal mouse brain. (a–c) Representative scans obtained via two-photon imaging of dye-filled OPCs recorded in NG2DsRedBAC mice at E18.5 (a), P7 (b) or P12 (c) respectively. (a: Note that this OPC was dividing at the time of acquisition. Scale bar = 10 µm.) (d–f) The maximum projection of the traced dendrites for the cell shown in (a–c) are displayed in (d–f). Scale bars = 10 µm. The maximum projection of the z-stack of a given OPC was outlined to determine the area the cell is occupying. (g–h) For each cell the outlined territory (g, area) and the summed length of all dendrites traced (h, dendritic length) as indicated in (d–f) was measured. The mean value for the area and the dendritic length of each age group ($n = 10$ [E18.5], $n = 8$ [P7], $n = 10$ [P12]), is shown in (g) (E18.5 vs. P7 $p < .05$ and E18.5 vs. P12 $p < .05$; P7 vs. P12 $p > .05$, one-way ANOVA with post-hoc Tukey's test) and (h) (E18.5 vs. P7 $p < .05$ and E18.5 vs. P12 $p < .05$; P7 vs. P12 $p > .05$, one-way ANOVA with post-hoc Tukey's test) respectively. (i) The 3D-traced dendrites (as shown in [d–f]) were used for a 3D Sholl analysis. OPCs in the embryonic brain only show a third of the number of intersections found in postnatal OPCs. The most distant intersections identified were 85 µm and 100 µm remote from the soma in embryonic and postnatal OPCs, respectively. (j) The summed length of all dendritic paths positively correlated with the mPSC frequency in OPCs, ($r = 0.6232$, $r^2 = 0.3884$, $p < .05$, Pearson correlation coefficient). (k) To account for the reduced size of the embryonic OPCs the frequency of mPSCs was normalized to the mean total length of the OPC dendrites at the respective age (E18.5 vs. P7 $p < .05$, E18.5 vs. P12 $p < .05$, P7 vs. P12 $p < .05$, one-way ANOVA with post-hoc Tukey's test). (l) Charge transfer also takes amplitudes and decay time into account for comparing synaptic drive of OPCs (E18.5 vs. P7 $p < .05$, E18.5 vs. P12 $p < .05$, P7 vs. P12 $p > .05$, one-way ANOVA with post-hoc Tukey's test).

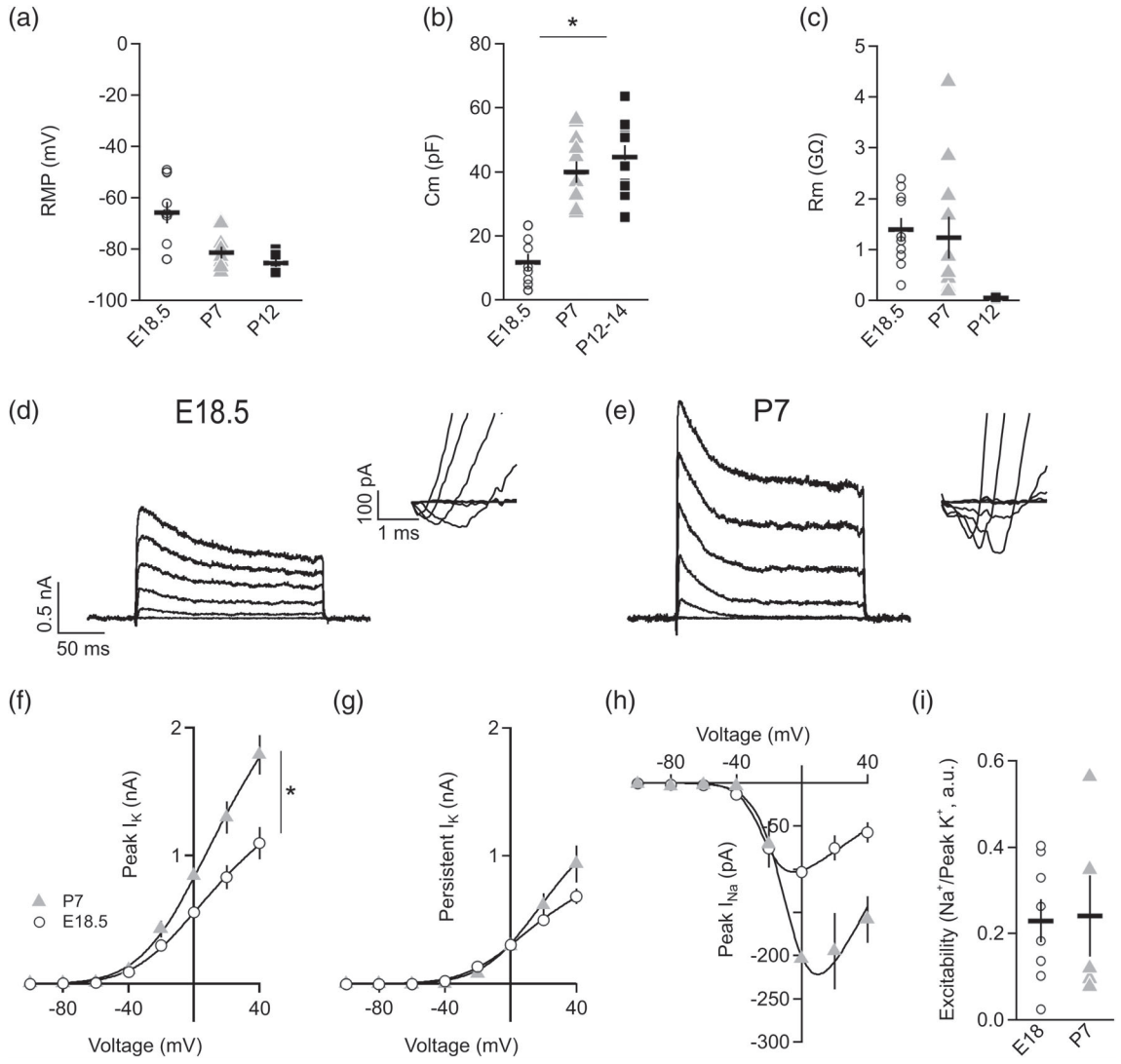

FIGURE 3 Ion channels of OPCs in the embryonic and the postnatal brain. (a and b) OPCs in the embryonic brain tended to show a more depolarized resting membrane potential but the statistical comparison to the postnatal group did not reach the level of significance (RMP; E18.5 [$n = 12$ cells] vs. P7 [$n = 13$ cells] $p > .05$, Unpaired t test). Embryonic OPCs displayed a smaller membrane capacitance (Cm; E18.5 [$n = 12$ cells] vs. P7 [$n = 14$ cells], $p < .05$, Student's t-test) compared to OPCs in postnatal mice. (c) The membrane resistance (Rm) of OPCs at E18.5 was comparable to P7 OPCs (E18.5 ($n = 12$ cells) vs. P7 ($n = 14$ cells) $p > .05$, Student's t-test). Note the significant drop of membrane resistance in the P12 group ($p < .05$, 1-way ANOVA). (d and e) Representative membrane current patterns of OPCs. Membrane currents were obtained by subjecting the cells to hyper- and depolarizing voltage steps ranging between −100 and +40 mV. Original membrane currents were leak current-subtracted to reveal the Na^+ currents at more depolarizing membrane potentials, which are indicated by the rectangular boxes and depicted on a smaller time scale next to each membrane current recording. (f–h) IV curves for the peak K^+ current (f) (peak K^+ current at +40 mV of E18.5 [$n = 9$ cells] vs. P7 [$n = 8$ cells] $p < .05$, Student's t-test), the persistent K^+ current (g) (persistent K^+ current at +40 mV of E18.5 [$n = 9$ cells] vs. P7 [$n = 8$ cells] $p > .05$, Student's t-test) and the peak Na^+ current (h) (peak Na^+ current at 0 mV of E18.5 [$n = 9$ cells] vs. P7 [n = 8 cells] $p > .05$, Student's t-test) were obtained from the leak current-subtracted IV curves shown in e and f. (i) The excitability of OPCs at E18.5 (d) calculated by dividing the Na^+ current by the peak K^+ current recorded between −40 and 0 mV was comparable to P7 OPCs (E18.5 [$n = 9$ cells] vs. P7 [$n = 8$ cells] $p > .05$, Student's t-test).

with the OPC identity of isolated cells (Figure 4b and Supplementary Figure 1a–c).

Our RNA-seq analysis revealed 3265 genes to be differentially expressed between E16.5 and P4 (1922 up- and 1343 down-regulated genes, Supplementary Figure 1d), while 2288 genes were differentially expressed between P4 and P12 (1733 up- and 555 down-regulated genes, Supplementary Figure 1e). All differentially expressed genes (DEGs) of our samples, up- and down-regulated, were further analyzed using the gene ontology enrichment analysis and visualization tool (GOrilla) to determine their potential functions, localizations and pathways. When comparing the DEGs between E16.5 and P4, GO-terms related to the synapse, the plasma membrane, the extracellular region and cell junctions were highly enriched (Supplementary Figure 1f and Supplementary Table 1 for the

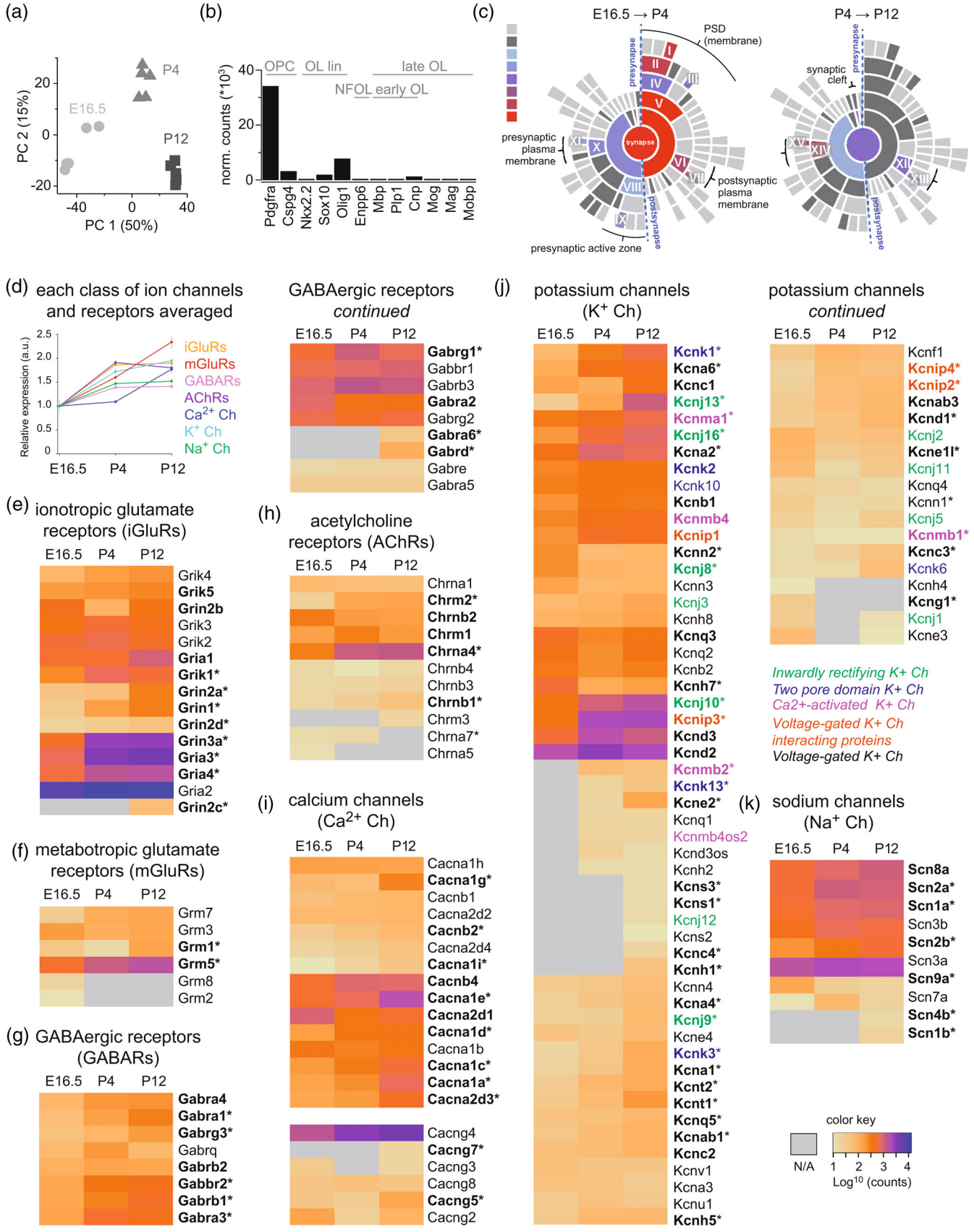

FIGURE 4 Legend on next page.

individual DEGs per GO-term; only GO-terms with a FDR $<10^{-11}$ are listed). Strikingly, when comparing differentially expressed genes between P4 and P12 we found a high association with the same GO-terms (FDR $<10^{-11}$), but the GO-terms synapse and cell junction were not enriched anymore (Supplementary Figure 1g, and Supplementary Table 2 for the individual DEGs per GO-term), indicating, in accordance with our electrophysiological recordings, that the synaptic drive of OPCs by neurons is largely established only early postnatally and then maintained from P4 on at a high level.

To investigate the developmental regulation of synaptic genes in OPCs in more detail, we analyzed genes that exhibited an increase in expression from E16.5 to P4 or from P4 to P12 using a database of curated annotations of synaptic genes, SynGO (Koopmans et al., 2019). As seen with GOrilla, the increase in the expression of synaptic genes was most pronounced between E16.5 and P4 (Figure 4c left) and only few up-regulated genes were found between P4 and P12 (Figure 4c right). Up-regulated synaptic genes found at P4 to the largest extent encoded postsynaptic proteins, but not presynaptic proteins, consistent with the physiological observation that OPCs are postsynaptic partners and not known to synapse onto other cells (Figure 4c).

We performed a single gene-based analysis for proteins important for postsynaptic electrical signal integration, neurotransmitter receptors and ion channels. Overall, mRNA expression levels of those genes were up-regulated during development for all channel and receptor subclasses. Except for metabotropic glutamate receptors and calcium channels, the most pronounced changes were seen between E16.5 and P4 (Figure 4d). This was also evident for a small group of highly abundant genes which exhibited very substantial mRNA levels from P4 onwards: *Gria3* (GluR-3), *Gria4* (GluR-4) and *Grin3a* (GluN3A) (ionotropic glutamate receptor subunits), *Grm5* (mGluR5, metabotropic glutamate receptor), *Gabra3* (GABA(A) receptor subunit beta-3), *Gabbr2* (GABA(B) receptor subunit 2), *Chrna4* (neuronal acetylcholine receptor subunit alpha-4), voltage-gated calcium channel *Cacna1e* ($Ca_V2.3$, Shal-related), *Kcnd2* (Kv4.2, A-type potassium channel), *Kcnd3* (Kv4.3, A-type potassium channel), *Kcnj10* (Kir4.1, background potassium channel), *Kcna2* (Kv1.2, delayed rectifier) and sodium voltage-gated channel alpha subunits (*Scn1a*, *Scn2a*, *Scn3a* and *Scn8a*) (Figure 4e–k). *Gria2*, the subunit limiting the calcium permeability of AMPA receptors, stands out as it is already highly expressed at E16.5 (Figure 4e) and is the most abundant of all receptor genes listed in Figure 4 at all time points.

Recruitment of R−/T-type voltage-gated calcium channels plays an important role for the integration of synaptic input by postnatal OPCs (Sun et al., 2016). This is supported by our transcriptional analyses showing that *Cacna1e* (R-type) and *Cacna1a* (P/Q-type) are the most highly expressed voltage-gated calcium channel alpha subunits in P12 OPCs (Figure 4l).

Even though Acetylcholine (Ach) signaling has been implicated in the regulation of myelination decades ago (Toran-Allerand, 1974), only recently has its direct effect on OPC proliferation and differentiation been investigated (Fields et al., 2017). Strikingly, we find a very strong increase in the levels of *Chrna4* (Neuronal acetylcholine receptor subunit alpha-4) and *Chrm2* (Cholinergic receptor muscarinic 2) from embryonic to postnatal OPCs (Figure 4h).

We next compared the abundance of genes coding for receptors and ion channels in OPCs (P12) and layer 2/3 cortical neurons (P33-35), which had been isolated by FACS and subjected to bulk RNA-seq. To this end, we ranked genes according to their abundance in each cell type and then comparatively analyzed the ranked lists

FIGURE 4 Genes coding for components of the postsynapse are strongly up-regulated in OPCs from E16.5 to P4. (a) Principal component analysis (PCA) of bulk RNA seq data of cells MACS-sorted from the brain of PDGFRα^+ (CD140a+) mice showed clustering of the transcriptional patterns of the samples in the three age groups ($n = 5$ for each group). (b) Mean expression levels of genes coding for cell type-specific markers for OPCs, oligodendrocytes lineage cells (OL lin), newly formed oligodendrocytes (NFOL), oligodendrocyte-specific myelinating markers up-regulated early (early OL) and oligodendrocyte-specific myelinating markers up-regulated later (late OL) in the RNA data set at P4 demonstrate a high grade of purity achieved via MACS isolation of OPCs. Further genes specific for other cell types detected in P4 samples as well as corresponding graphs for E16.5 and P12 can be found in Supplementary Figure 1a–c. (c) SynGO annotations for synaptic genes that are up-regulated in OPCs from E16.5 to P4 (left) and from P4 to P12 (right). Color scale indicates- -log10 Q-value ranging from light blue (2) to bright red (≥7) color. Sectors colored in gray represent SynGO terms holding too few genes (light gray) or being not significantly enriched (dark gray). Note that more synaptic GO-terms, especially postsynaptic GO-terms, are significantly enriched between E16.5 and P4 than between P4 and P12. I (integral component of postsynaptic density membrane), II (postsynaptic density membrane), III (integral component of postsynaptic specialization membrane), IV (postsynaptic density), V (postsynaptic specialization), VI (postsynaptic membrane), VII (integral component of postsynaptic membrane, VIII (presynaptic active zone), IX (integral component of presynaptic active zone membrane), X (presynaptic membrane), XI (integral component of presynaptic membrane), XII (postsynaptic membrane), XIII (integral component of postsynaptic membrane), XIV (presynaptic membrane), XV (integral component of presynaptic membrane). (d–k) Heatmaps plotting the DEseq2 normalized counts for genes encoding different channels and receptors found in OPCs of mice at E18, P4, and P12. Gene expression is color-coded from light yellow (low expression) to dark purple (high expression), apart from genes with count rates below 10, which are depicted In gray (N/A). Genes significantly up- or down-regulated between E16.5 and P12 are shown in bold letters, while asterisks mark genes with a more than 2-fold increase or decrease. (d) Mean expression level of the different channel and receptor families (b–h) per age group normalized to E16.5 levels. (e) ionotropic glutamate receptors. (f) metabotropic glutamate receptors. (g) GABA-ergic receptors. (h) acetylcholine receptors. (i) calcium channels. Genes encoding the calcium channel γ subunit (Cacng) family are plotted separately as Cacng2, 3, 4, 5, 7, and 8 have been identified as auxiliary proteins to AMPARs (Transmembrane AMPAR regulatory proteins, TARPs). (j) potassium channels, including inwardly rectifying potassium channels (green), two pore domain potassium channels (blue), potassium calcium-activated channels (purple), potassium voltage-gated channel interacting proteins (red), voltage-gated potassium channels (black). (k) sodium channels.

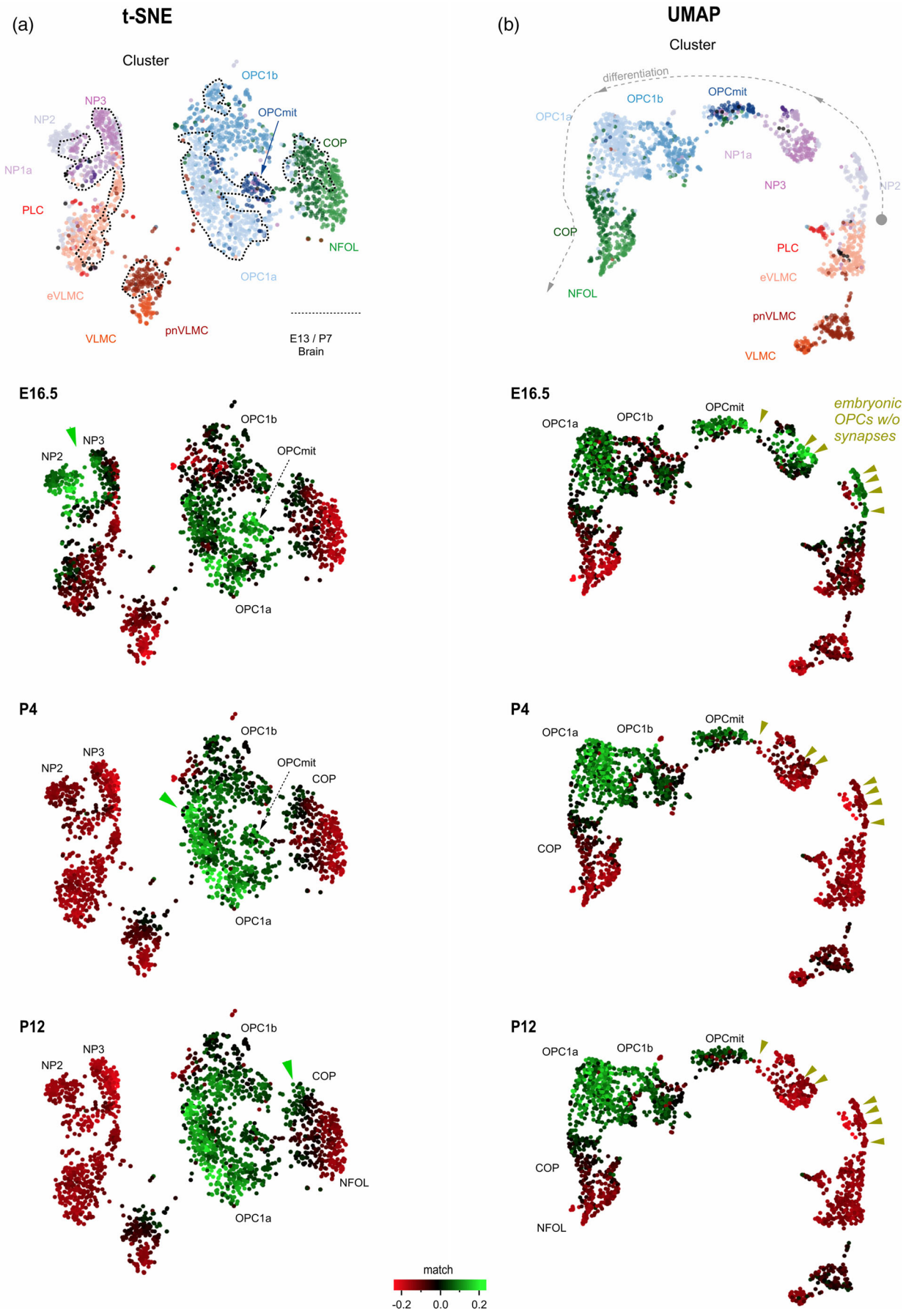

FIGURE 5 Legend on next page.

(Supplementary Figure 2a,b). Approximately half of the top 15 most highly expressed receptor genes were shared by OPCs and neurons whereas the other genes partly showed striking differences in expression. In particular, *Gria3*, *Gria1*, *Grik1*, *Chrna4*, *Gabrb3*, and *Gabrb2* were highly expressed in OPCs but only found in the lower half of all genes expressed in neurons. Conversely, *Grin2c*, *Grm3*, *Grm7*, and *Gabra4* were highly expressed in neurons but only found at lower levels in OPCs. For ion channels the most striking differences were observed for a number of calcium- and voltage-gated potassium channels and *Cacna2d4*, all highly expressed in neurons but not in OPCs whereas *Kcnj13*, *Cacna1a*, and *Kcnd3* were highly ranked in OPCs but not among the 50% most abundant genes in neurons.

The low frequency of synaptic currents in embryonic OPCs might be caused by an inability of those cells to connect to the presynaptic neurons. To investigate this hypothesis, we analyzed the expression of cell-adhesion molecules (CAMs), a broad class of molecules known to be important for synaptogenesis (Südhof, 2018), in our RNA-seq data (Supplementary Figure 3). This analysis revealed 162 DEGs out of 315 genes classified as CAMs, when comparing embryonic to P4 OPCs, levels of 104 genes increased and of 58 went down. We next classified the CAMs according to their localization at the synapse into postsynaptic, presynaptic, pre- and postsynaptic, and secreted and Supplementary Figure 3 shows the expression levels of all 315 genes. Supplementary Figure 4a depicts the regulation at the level of the four classes and demonstrates that all classes apart from presynaptic CAMs exhibited a strong increase in expression from E16.5 to P4 but only a mild or no up-regulation from P4 to P12 indicating that OPCs form functional postsynapses between E16.5 and P4. Panels c-f in Supplementary Figure 4 show the normalized expression for selected genes of each of the four classes. Among the 10 differentially expressed CAM genes showing the strongest developmental increase in abundance were the Glypican 5 (*Gpc5*, Supplementary Figures 3c and 4c), Contactin 6 and 4 (*Cntn6*, *Cntn4*, Supplementary Figures 3b and 4d), four Protocadherins (e.g., *Pcdha12*, *Pcdh20*, *Pcdhb5*, *Pcdh15*, Supplementary Figures 3b and 4d) as well as secreted CAMs, like two members of the Complement C1q Like family (*C1ql1*, *C1ql3*, Supplementary Figures 3a and 4e). In contrast, presynaptically localized CAMs showed little regulation during development (Supplementary Figures 3d and 4f).

We next also compared the abundance of genes coding for CAMs in OPCs (P12) to layer 2/3 cortical neurons (P33-35, Supplementary Figure 4b). In contrast to the receptors and ion channels analyzed above, the 15 most strongly expressed genes coding for CAMs belonged for both OPCs and neurons to the globally most abundant genes (above 95 percentile) and there were only few of the top 15 genes which were only weakly expressed in the other group. *Pcdh15* was the only top 15 OPC gene which showed low levels in neurons and *Sema4d*, *Fgf3*, and *Igsf8* were strongly expressed in neurons but not in OPCs.

Essential components of the postsynaptic signaling complex in neurons are the proteins that form the postsynaptic density (PSD). Throughout the three age groups we detected in OPCs most of the major scaffold and signaling proteins of CNS excitatory PSDs like membrane-associated guanylate kinases MAGUKs (*SAP97/Dlg1*, *PSD-93/Dlg2*, *SAP102/Dlg3*, *Dlg5*), guanylate kinase-associated protein (*GKAP/Dlgap1*), *SH3* and multiple ankyrin repeat domain proteins 1–3 (*Shank1-3*), *Homer1-3*, the Ca^{2+}-regulated serine–threonine Protein kinase *CaMKII*, *SynGAP*, *Anks1b/AIDA-1* and *IRSp53/BAIAP2* (Supplementary Figure 5a,b). The by far two most abundant PSD genes in P12 OPCs were the glycogen synthase kinase 3 beta (*Gsk3b*) and catenin beta (*Ctnnb1*), two proteins with roles in postsynaptic plasticity (Draffin et al., 2021) and transsynaptic signaling (Chen, Morrison, et al., 2017), respectively (Supplementary Figure 5a,b). Surprisingly, PSD95/Dlg4 was not found in OPCs although it represents the major scaffold protein in neuronal glutamatergic postsynapses. A comparison of P12 OPCs to cortical neurons (Supplementary Figure 5b) revealed that all top 15 PSD genes of OPCs were strongly expressed in neurons (above global 80 percentile). On the other hand, *Camk2a*, *Dnm2*, *Akap5*, *Abr*, and *Pak1* seemed to be quite specific for neurons and were found only at low levels in OPCs.

We took advantage of a published Single-Cell RNA sequencing (scRNA-seq) analysis of oligodendroglial and other cells from the brain and spinal cord (re-plotted on the left of Figure 5a, cf. Marques et al., 2018) to explore the likely cellular composition of our

FIGURE 5 Bulk transcriptomics of E16.5 OPCs matches SC clusters previously identified as NPs. Deconvolution of our bulk RNA-seq data using the Marques et al. (2018) scRNA-seq data. In the first row (a and b), each point indicates an individual cell analyzed by Marques et al. (2018) and is colored according to the cell cluster it was assigned to. Clusters are labeled as in Marques et al. (2018): NP (neural progenitor), PLC (pericyte lineage cell), e/pnVLMC (embryonic/postnatal vascular and leptomeningeal cell, OPC (oligodendrocyte precursor cell), OPCmit (mitotic OPC, previously called OPCcyc), COP (committed oligodendrocyte precursor cell) and NFOL (newly formed oligodendrocyte). Black cells labeled "Cycling cells" and intermingled with cells of several clusters in the original plot were omitted due to their small number. (a) tSNE coordinate space is reproduced from Marques et al. (2018) (see methods). Dotted lines demarcate regions containing cells derived from brain (E13/P7) versus spinal cord cells or cells from the juvenile to adult brain (outside dotted line). (b) Same as (a), however here the feature space plot of cells from the Marques et al. (2018) scRNA-seq data was determined using UMAP instead of tSNE. A gray dotted line with arrowheads indicates the starting point and direction of the putative OPC differentiation. Rows two, three and four in (a) and (b) color code for each cell in the Marques data set how well it is aligned to our bulk RNA samples obtained at E16.5, P4, and P12, respectively. The color of each point indicates the inferred abundance of individual cells from the Marques data set in our bulk RNA-seq samples, ranging from negative (red) to positive (green). Abundance levels are scaled and comparable across samples. The alignment of our E16.5 bulk RNA-seq data not only with OPC but also NP populations suggests that groups previously classified as NP might represent embryonic OPCs, which do not yet bear synapses. This putative group of cells is indicated by the dark-yellow arrowheads (arrowheads do not point at individual cells).

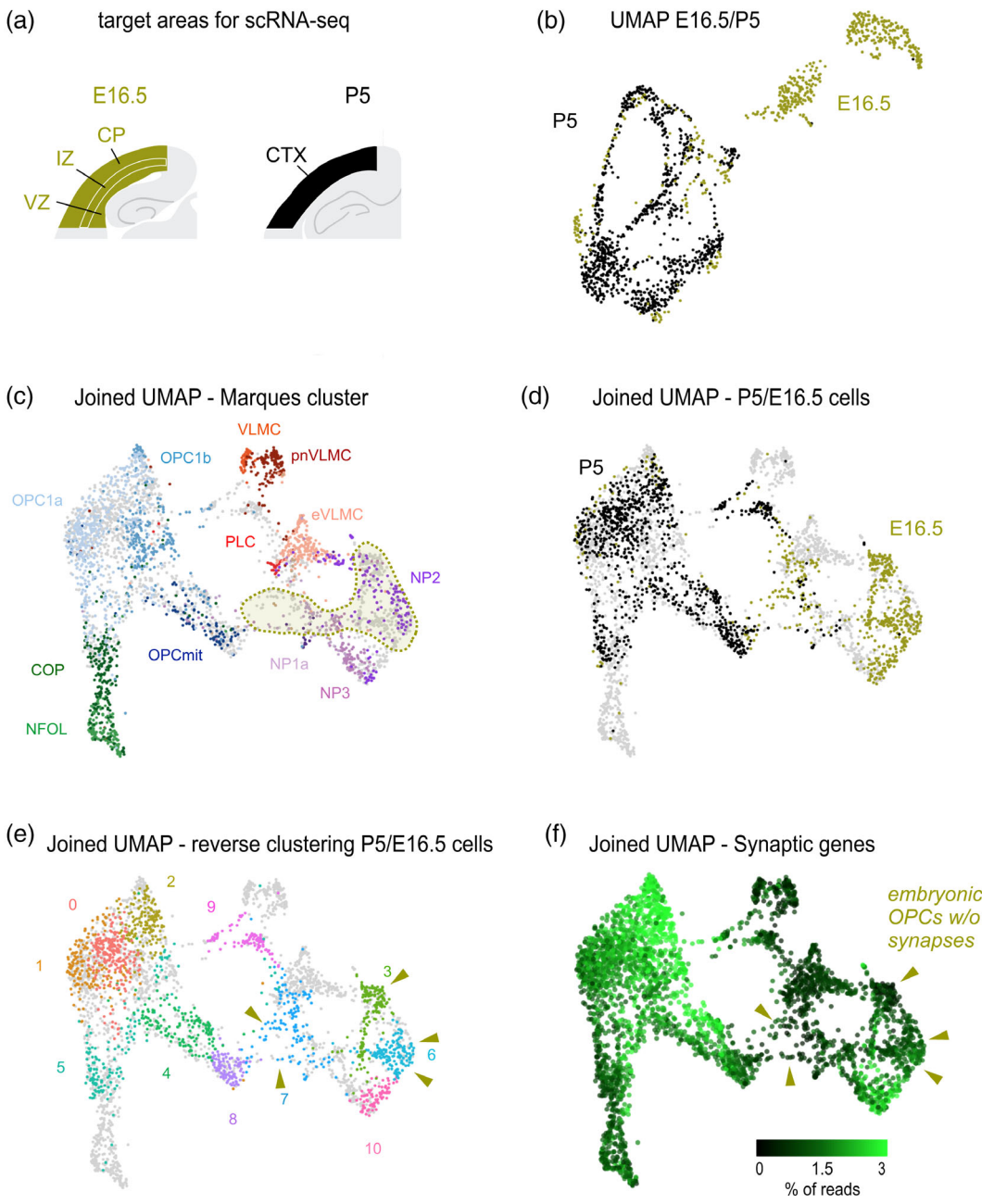

FIGURE 6 Single-cell transcriptomic analysis reveals that embryonic OPCs represent a unique developmental state with similarities to neuronal progenitors. (a) Schemes illustrating the brain areas dissected for collecting OPCs that underwent scRNA-seq. In both age groups OPCs were isolated from the isocortex (CTX), which at E16.5 consists of the cortical plate (CP), intermediate zone (IZ) and ventricular zone (VZ). (b) UMAP plot for the E16.5 (yellow) and P5 (black) PDGFRα^{+} cells harvested from regions shown in a. (c) Joint UMAP plot integrating our E16.5/P5 cells (in gray) and the E14, P7, P20-30, and P60 cells from Marques et al. (2018). Cells analyzed in our study are gray and in the background. Note that the overall architecture of the feature space plot is maintained compared to Figure 5b. (d) Same as in c but illustrating the distribution of our cells in the foreground according to age (E16.5 in yellow, P5 in black, cells from Marques et al. (2018) in gray and in the background). (e) Clusters of our cells reversely defined using E16.5/P5 cellular reductions of the joint UMAP. Note that these clusters demonstrate clear separation on our E16.5/P5 UMAP (d). Yellow arrowheads denote the group of cells likely representing embryonic OPCs without synapses (arrowhead do not point at individual cells). (f) The expression levels of 140 genes coding for synaptic proteins (CAMs, PSD, receptors, channels) ranging from low (black) to high (green) for each cell on the integrated UMAP graph are shown as the percentage of reads mapping to all 140 genes (Supplementary Table 3).

developmental data set. To this end, we deconvolved our bulk RNA-seq data with the previously published scRNA-seq data set (Marques et al., 2018) and labeled those cells green when their gene expression was aligned well with our average bulk sequencing data from E16.5, P4, and P12 (Figure 5a). This analysis confirmed that our cell population was not contaminated by non-oligodendroglial cells (vascular and

leptomeningeal cell ("VLMC"), pericyte lineage cell ("PLC") or newly formed oligodendrocytes ("NFOL") and showed a good alignment of our samples with OPCs harvested from the embryonic and postnatal brain but to a lesser extent with cells isolated from spinal cord (Figure 5a, dashed lines encircle cells of brain origin). Furthermore, this analysis revealed a clear developmental progression (denoted by the green arrowheads): the match of our samples progressed from the left of the tSNE-based feature space plot (E16.5), toward the right for P4 and P12. E16.5 samples shared few features with late OPCs (committed OPCs, "COP") for which an overlap was only seen in P12 samples (Figure 5a). "NFOL" did not show a match with any of our samples. Importantly, we observed for the E16.5 but not for the P4 or P12 samples a pronounced inferred abundance of cells within clusters previously called neural progenitors ("NP1-3") (Figure 5a green arrowhead at E16.5). This inspired us to re-explore cluster relationships by calculating a UMAP-based similarity matrix from the published data. UMAP has been demonstrated to be more reproducible and to better preserve the global structure of scRNA-seq data, making the inference of distances between cells and clusters more meaningful (Becht et al., 2019). When plotting using a UMAP-based feature space, the cell clusters previously defined were well maintained, but the "NP" clusters now were located close to the "OPC" clusters (Figure 5b). In addition, a linear path of putative OPC differentiation starting near the NP2 cluster became apparent and the non-oligodendroglial clusters ("VLMC", "PLC") were better separated from oligodendroglial clusters (Figure 5b, left panel, gray dashed line). The existence of this path was supported by a gradual transition and emergence of well-aligned, "green" cells from right to left in our deconvolved RNA-seq samples from E16.5, P4, and P12, respectively (Figure 5b, right panels). This developmental progression was also observed within the E16.5 group (likely due to some unavoidable variability in the time between conception and sample preparation). Reorganization of these individual samples according to their similarity to the P12 group revealed a gradual conversion toward P4 (Supplementary Figure 6a) and a decreasing enrichment of cells belonging to the NP clusters. Supplementary Figure 6b shows how the large variability in the E16.5 samples converges onto the P4 samples and that the variability within the P4 and the P12 group was much lower, indicating a more homogenous transcriptional profile of cells of the postnatal samples.

This suggested that cells belonging to the "NP" clusters may not be "neural progenitors" but instead represent early OPCs and potentially the starting point for early oligodendroglial development. The finding that cells of "NP" clusters selectively aligned well to our E16.5 samples and that our physiological analysis showed that OPCs without synaptic input also only occurred in the E16.5 group suggested that those "NP" cell clusters corresponded to embryonic OPCs lacking synaptic input (Figure 5b). The cluster "OPC1a, OPC1b" and "OPCmit" were also well aligned with our E16.5 data set and we assumed that those cells represented OPCs from brain regions which at E16.5 contain OPCs which already had developed further and established synapses. For example, in cerebellum and spinal cord, regions at least partially contained in our samples, OPCs start to differentiate around birth whereas differentiation only occurs approximately 1 week later in the rodent cortex (Cristobal & Lee, 2022; Reynolds & Wilkin, 1988; Trapp et al., 1997).

Apart from the regional heterogeneity of the OPCs in our bulk samples, a weakness of the deconvolution approach is that while it shows how a bulk sample can potentially be explained by a certain combination of cells from a SC data set, it cannot prove that the bulk sample indeed contained individual cells which express the set of genes from a given cell of the scRNA-seq data set.

To avoid the regional heterogeneity and overcome the limitations of the deconvolution approach we micro-dissected similar regions used for our electrophysiological analysis (cortical plate/intermediate layer at E16.5 and cortex at P5; Figure 6a, cf Figure 1a), isolated OPCs and subjected them to scRNA-seq (see methods for details). After initial processing, we obtained 562 (E16.5) and 986 (P5) cells, which predominantly separated on a UMAP plot by developmental time (Figure 6b) confirming the transcriptional differences between developmental states reported above.

We next directly integrated our scRNA-seq data with that of Marques et al. (2018) and calculated a UMAP-based cellular feature space to determine the joint cellular neighborhoods of our cells with Marques cells (Figure 6c,d). Although the precise arrangement of cells was expected to deviate from the original Marques UMAP with inclusion of two additional time points (E16.5 and P5), the overall preservation of global cellular locations, and in particular the direction of differentiation from right to left and to the bottom, indicated a high consistency of the two data sets. The vast majority of our E16.5 OPCs were grouped with the NP annotated clusters (Figure 6c,d), previously identified as neural progenitor cells (Marques et al., 2018) and supporting our view derived from the bulk RNA-seq data analysis that many cells of the NP clusters in fact represent early embryonic OPCs. In contrast, OPCs from P5 tissue were solely found within the OPC1a/b, OPCmit and COP clusters. Based on this UMAP (Figure 6d) we performed a reverse clustering of our data (Figure 6e). These clusters superimposed well onto many of the clusters defined by Marques et al. (2018) (Figure 6c,e). To explore which cells might be or have the potential to be engaged in synaptic signaling we quantified the expression levels of synaptic genes across all cells. We curated a list of 140 genes based on the most abundantly expressed synaptic CAMs (50), PSD proteins (40) and receptors/ion channels (50) in the P4 group of our bulk RNA-seq data from above (Figure 4d–k, Supplementary Figures 3–5, see methods for details). The integrated cell space in Figure 6f shows that in cells from both data sets, Marques et al. (2018) and ours, synaptic genes at high levels are predominantly found in the OPC clusters (OPC1a/b, OPCmit largely corresponding to 0, 1, 2, 4, 8). In contrast, clusters from our E16.5 group in proximity to the NP clusters (cluster 3, 6 and 7; Figure 6c–e) demonstrated lower levels of synaptic gene expression. Our E16.5 cluster 10, which partially overlaps with NP2 and NP3, represented a notable exception and displayed high levels of synaptic gene expression. Overall, considering that embryonic OPCs did not, or only very rarely, show functional synaptic currents and that these cells did not cluster with postnatal OPCs but rather group with NP cells, supports a view that they represent a distinct developmental stage of embryonic OPCs without synapses. The

location of cells coding for expression levels of synaptic genes (Figure 6f) not only showed a gradient of increased expression from embryonic to mature OPCs but also a decline in expression when OPCs further differentiate into COPs and NFOL. The latter is in agreement with previous electrophysiological observations showing that differentiating oligodendroglial cells loose synaptic input from neurons (Biase et al., 2010; Kukley et al., 2010).

We did not observe OPCs without synapses in the postnatal period (Kukley et al., 2008, 2010) opening the question whether embryonic OPCs without synapses mostly die before the postnatal period, possibly because synaptic innervation is needed for their survival. Indeed, it was reported that many of the OPCs which were generated in the embryonic brain disappear from the cortex during the first postnatal week (Kessaris et al., 2006). OPCs rapidly disappearing in the early postnatal period are derived from NKx2.1-expressing precursors, whereas surviving OPCs stem from precursors expressing Gsh2 or Emx1 (Kessaris et al., 2006). Emx1 is present in cells of the E16-18 intermediate zone (Briata et al., 1996; Gulisano et al., 1996) and these progenitors generate a large proportion (Kessaris et al., 2006) if not most (Winkler et al., 2018) of the postnatal and embryonic oligodendroglial cells. To check whether our embryonic OPCs may belong to the surviving or disappearing fraction we analyzed the Emx1, Gsh2 and NKx2.1 expression in our embryonic and postnatal OPCs. While none of the markers were expressed in P5 OPCs, expression of Emx1 but not Gsh2 or NKx2.1 was found within clusters 3 and 6 (Supplementary Figure 7) suggesting that embryonic OPCs lacking synapses derive from the NP clusters 3, 6, and 7 or even overlap (cluster 3 and 6) with Emx1 expressing precursors and very likely survive into the postnatal period thereby contributing to the cortical oligodendroglial progeny by further expansion and differentiation.

4 | DISCUSSION

In this study, we found that the synaptic input to embryonic (E18.5) OPCs is at least ~3–10 times weaker compared to P7-14 OPCs. At the molecular level our RNA-seq analyses revealed that the overall abundance of genes coding for the postsynaptic signaling complex/apparatus is much lower at E16.5 than at P4 and P12 (also see Marques et al., 2018). The comparison of our bulk- and scRNA-seq to a previously published scRNA-seq data (Marques et al., 2018) suggests that embryonic OPCs without synaptic input form a transcriptionally distinct group of precursor cells at the beginning of the developmental trajectory of the oligodendroglial lineage. We propose that these cells represent a unique developmental stage that is not yet receptive for synapses from neurons because the required transcriptional programs are not yet activated to the full extent. The data also show that pronounced proliferation and migration of OPCs occur in the absence of synaptic input.

Synaptic input has been reported in almost all hippocampal OPCs examined so far (Biase et al., 2010; Kukley et al., 2008, 2010). However, these measurements were performed only in postnatal OPCs, ranging from P4-5 (Biase et al., 2010; Kukley et al., 2008) up to old age (Passlick et al., 2016; Ziskin et al., 2007). Here, we show for the first time that embryonic OPCs almost completely lack synaptic input. Considering the relatively small size of E18.5 OPCs the question arises whether their smaller surface area could explain the reduced frequency of synaptic currents. However, when correcting for the smaller dendritic arbor as well as the frequency, amplitude and charge of synaptic currents, the synaptic drive of OPCs remains negligible and dramatically smaller than at postnatal stages.

What causes the lower frequency of synaptic currents in embryonic versus postnatal OPCs? One reason for the low frequency of mPSCs detected in embryonic OPCs could be that at this stage of brain development synaptic transmission in general is not sufficiently mature. However, this is not the case as it has been shown that cortical neurons already at E16 receive functional glutamatergic and GABA-ergic synaptic contacts (Kilb et al., 2011). This is consistent with our immunohistochemical analysis of the synaptic vesicle marker protein (SV2B) which we found widely distributed throughout the embryonic brain. Therefore, it appears that there is not a general inability to establish synapses in the embryonic period but that embryonic OPCs do not have the capacity to receive synaptic connections or that embryonic OPCs are not suitable synaptic targets for neurons. Because the mPSCs, which we quantified in the presence of TTX, reflect synaptic vesicle release independent of presynaptic action potentials, the reduced frequency of mPSCs can be considered an indicator of the number of functional synapses (assuming a uniform spontaneous vesicle release rate in Ruthenium Red). Thereby, our functional data indicate that embryonic OPCs have fewer functional synaptic contacts compared to postnatal ones (also when correcting for shorter dendrites).

The mPSCs in embryonic OPCs were not only extremely rare but also showed substantially smaller amplitudes. A potential reason for smaller amplitudes may be a much lower density of postsynaptic glutamate and GABA receptors at this early developmental stage compared to postnatal time points. On the other hand, our transcriptomics analysis showed that several glutamate and GABA receptor subunits are already expressed at E16.5. Furthermore, Spitzer et al. (2019 pharmacologically activated glutamate receptors on E18 OPCs and reported current densities (amplitudes divided by cell capacitance) comparable to a group of postnatal OPCs (P6-P16). This suggests that not the total number of glutamate receptors is the factor limiting the amplitude of synaptic currents but their distribution. If receptors are spread over the entire surface of OPCs they will be activated when applying agonists to the whole membrane but they may not be sufficiently concentrated at those synaptic contact sites where neurons locally release neurotransmitter-filled vesicles. Such apparent lack of clustering of neurotransmitter receptors around synaptic release sites may be a consequence of the immature expression pattern of genes coding for postsynaptic cell adhesion molecules in embryonic OPCs (Supplementary Figure 4, also see Marques et al., 2018). In summary, together with Spritzer et al. (2019) and Marques et al. (2018) our findings indicate an almost complete absence of synaptic connections between neurons and OPCs in the embryonic

brain and suggest that the existing very rare synaptic connections contain very few receptors only.

Could there be a functional relevance of the electrophysiological phenotype of embryonic OPCs which is characterized by a different set of ion channels and almost absent synaptic input? Postnatal OPCs express a large number of voltage-gated ion channels, including Na^+, K^+, and Ca^{2+} channels (Figures 3 and 4; Biase et al., 2010; Haberlandt et al., 2011; Maldonado et al., 2013; Spitzer et al., 2019), and these ion channels could actively participate in the synaptic integration of OPCs (Sun & Dietrich, 2013). It was previously shown that A-type K^+ currents strictly gate synaptic integration and the following Ca^{2+} signaling through the rapid suppression of post-synaptic depolarization (Sun et al., 2016). Here, we showed that embryonic OPCs are resting at a more depolarized potential and this depolarization will partially inactivate A-type K^{+}currents, which are already found at significantly lower levels in embryonic compared to postnatal OPCs (but see Spitzer et al., 2019). Therefore, an A-type K^+-current-induced gating effect will be largely absent in embryonic OPCs and their dendrites could more readily generate calcium signals in response to synaptic input. In fact, we found substantial levels of mRNA encoding the alpha subunits of T-, R- and N-type calcium channels (*Cacna1h*, *b*, *e*) in embryonic OPCs (also see Marques et al., 2018), which mediate synaptically-induced calcium signaling in postnatal OPCs (Sun et al., 2016). However, as synaptic input to embryonic OPCs is so small, it is quite unlikely that those calcium responses will be triggered at E18.5. But once these cells further develop and establish their first synaptic connections, they are set for dendritic calcium signaling.

Dendritic complexity of OPCs strongly increased from E18.5 to P7 as did the area covered by individual OPCs. During this phase of intense dendritic growth OPCs need to map out their space with regard to other OPCs and to neurons, a process that requires the expression of cell adhesion molecules and guidance receptors. Fittingly, our and previous analyses of bulk RNA-seq data comparing embryonic to postnatal OPCs showed an up-regulation of GO terms related to cell adhesion, cell communication as well as synapse and a down-regulation of terms linked to brain development and neuron migration at the postnatal stage (Marques et al., 2018; Spitzer et al., 2019). Our comprehensive analysis of the developmental transcriptional profile of cell adhesion molecules supports the involvement of several proteins which have been reported to play a role in dendritic outgrowth and pathfinding of OPCs, like ephrins and EphA/B receptors (Harboe et al., 2018; Linneberg et al., 2015), NCAM (Harboe et al., 2018; Oumesmar et al., 1995), L1-CAM (Laursen et al., 2009), Cadm/SynCAM/IGSF (Elazar et al., 2019; Hughes & Appel, 2019), FGFR2 (Furusho et al., 2012), Teneurin-4 (Hayashi et al., 2020), plexin-A4/−A3 (Okada et al., 2007; Xiang et al., 2012), contactin-1 (Lamprianou et al., 2011), and Nrg2/3 (Vartanian et al., 1999) as their expression levels strongly differ between embryonic and postnatal OPCs. Our data however goes a step further by identifying differentially expressed genes coding for cell adhesion molecules that have so far not been linked to OPC development, for example Cadherin EGF LAG seven-pass G-type receptor (*Celsr*) and complement C1q Like (*C1ql*), as well as novel isoforms of the above listed protein families (e.g. Ephrins, contactins, protocadherins, plexins). In particular, we for the first time identify cell adhesion molecules whose expression level is strongly up-regulated during the period of neuron—OPC synaptogenesis, suggesting a role in this process, which previously have only been studied in neurons, like *LRRTM3*, *GRID1*/2, and *Cntnap5* (Südhof, 2021). Interestingly, also Neuroligin 3 which has been reported to be up-regulated during brain tumor growth (Venkatesh et al., 2015, 2017) increases in expression during the phase of synaptogenesis supporting its role in normal neuron—OPC function but also indicating that its abundance needs to be tightly controlled. Overall, our systematic analysis provides a resource for further studies into the molecular mechanisms underlying dendritic outgrowth and synapse formation of OPCs.

Our comparative analysis of our bulk RNA-seq and the Marques et al. (2018) scRNA-seq data sets lead us to suggest that some clusters previously classified as neural precursors (part of NP2 and NP1a) represent an early stage of OPC development, a stage of OPCs lacking synapses (cluster 3, 6, 7). This suggestion was based on the following observations: (1) Our E16.5 bulk RNA-seq sample obtained from the whole brain using anti-PDGFRα-based cell isolation showed a pronounced alignment with the NP clusters. (2) Replotting the previously published data set as a UMAP removed the gap previously seen between NP and OPC clusters and brought the NP clusters closer to the OPCmit cluster and this neighborhood indicates transcriptional similarity. (3) PDGFRα-expressing cells in the cortical plate and intermediate zone at E18.5 also express NG2 (Figure 1) and $NG2^+$ cells in that region do not express neural precursors markers (Tognatta et al., 2017) which indicate that those cells represent OPCs. These cells were used for our scRNA-seq sample and they almost exclusively mapped onto the NP clusters. (4) Our patch-clamp analysis of NG2-DsRed+, $NG2^+$ and $PDGFR\alpha^+$ cells in the intermediate zone at E18.5 demonstrated that those cells are morphologically very related to postnatal OPCs (Figure 2) and show a very similar pattern of ion channel expression (Figure 3) which further supports the view that the E16.5 isolated embryonic OPCs which overlap with NP clusters indeed represent early OPCs. On the other hand, it appears likely that not all cells contained in the NP clusters defined by Marques et al. (2018) represent early OPCs. This can best be seen in the NP3 cluster which only showed minimal overlap with our E16.5 cells. Also, our E16.5 data set seems to contain a small number of cells not compatible with embryonic OPCs lacking synapses: cluster 10, overlapping with parts of NP2 and parts of NP3 (Figure 6) showed a strong expression of synaptic genes not expected from OPCs without synapses. Therefore, the composition of the NP clusters likely is heterogeneous and may include both neural precursor cells and early OPCs. Their proximity in all feature space plots (UMAP and t-SNE) strongly indicates that neural precursors and early OPCs exhibit a similar transcriptional profile at least for certain prominent subsets of genes. Further, considering that the early neural and oligodendroglial developments are tightly linked (Bergles & Richardson, 2016), it may well be that either NP cells and early OPCs derive from the same

progenitor or that early OPCs (Emx1^{+}) even directly arise from cells of the NP clusters. The close transcriptional relationship of OPCs, early OPCs and neural or intermediate progenitors has been well documented (Hochgerner et al., 2018; Manno et al., 2021; Weng et al., 2019; Yuzwa et al., 2017).

There are important differences in the approaches taken by the previous and this study to isolate cells for RNA-seq analysis: While we used antibodies fused to magnetic beads to isolate PDGFRα-expressing cells from the dorsal cortical area of E16.5 brains, Marques et al. (2018) relied on the expression of fluorescent marker proteins in two different transgenic mouse lines to isolate cells five days earlier from E13.5 brains. A Pdgfra promoter drove either Cre-Recombinase (Cre) or nuclear GFP-expression and Cre activity was induced at E12. Kessaris et al. (2006), Nishiyama et al. (1996), Winkler et al. (2018) reported that the first PDGFRα-immunoreactive cells in the dorsal forebrain are not found before E16 but neural stem cells express Pdgfra earlier in development (Funa & Sasahara, 2014; Pringle & Richardson, 1993). This may explain a preference for isolating those cells in the NP clusters representing true neural precursor cells versus embryonic OPCs in the Marques and the present study, respectively.

Our electrophysiological recordings were obtained from mice at E18.5, 2 days later than the time of isolation of our cells for the transcriptional analysis (E16.5) opening the question how representative our transcriptomics data is for the stage of the cells when physiologically analyzed. It was previously shown that the transcriptional signatures of glial precursors only slightly changed from E16 to E18 (Manno et al., 2021) and more specifically that OPCs harvested at E17.5 still mapped well to OPC and NP clusters of cells harvested much earlier at E13.5 (Marques et al., 2018). We therefore argue that the results of our transcriptomic analysis can be reasonably well compared to our physiological OPC data recorded 2 days later. Nevertheless, we admit that we do not have direct evidence showing how representative our transcriptomic data is for the time point at which we patch-clamped embryonic OPCs and this represents a weakness of our study.

In summary, our data reveals that the earliest embryonic OPCs are physiologically and morphologically similar to postnatal OPCs but lack the typical synaptic input from neurons. Embryonic OPCs do not sufficiently express genes for postsynaptic signal reception and processing and are therefore not yet receptive for connections from neurons. Furthermore, the data demonstrates that embryonic OPCs do not need synapses to proliferate or migrate in the embryonic brain.

During early development of zebrafish two subgroups of OPCs were identified (Marisca et al., 2020), which share features with postnatal and embryonic OPCs observed in this study. One group defined by their position being in the neuronal somata-rich area displayed a complex dendritic tree, proliferated slowly, expressed synaptic genes and generated stronger calcium signals in response to neural activity and can be viewed to correspond to our postnatal cortical OPCs. Another group being placed in the neurite and dendrite-rich areas showed a simple morphology, enriched genes for mitosis and migration, rapidly divided and only weakly responded to neuronal activity and thus seems to be more comparable to embryonic OPCs lacking synapses. These similarities may be taken to suggest an analogy between the two types of OPCs across species. However, there are a number of important differences. While the two subgroups of OPCs coexist in the larval brain of zebrafish, our embryonic OPCs and classical OPCs in the mouse were almost exclusively observed embryonically and postnatally, respectively. Further, while OPCs in the neurite/dendrite-rich area generated most oligodendrocytes in zebrafish, this is not the case for embryonic OPCs in the mouse because the first oligodendrocytes in rodent cortex and corpus callosum only appear after the first postnatal week (Trapp et al., 1997). Finally, both subgroups of OPCs in zebrafish showed a clear, classical OPC transcriptional signature whereas that was clearly not the case for our group of embryonic OPCs. Future studies are needed to explore to which extent the different subgroups of OPCs correspond across species and whether they have similar roots or functions in the brain.

It should be noted that the lack of synapses does not rule out that ambient neurotransmitters influence the development of embryonic OPCs in a non-synaptic manner nor that synaptic input may guide these processes during later developmental stages. Nevertheless, in our eyes the present data support the view that these synaptic one-to-one connections tune the early and local interaction between processes of OPCs and unmyelinated axons (Call et al., 2020; Paez & Lyons, 2020).

AUTHOR CONTRIBUTIONS

All authors contributed to writing this manuscript.

ACKNOWLEDGMENTS

Our work was supported by the Deutsche Forschungsgemeinschaft (DFG) (SS: SFB1089, SCHO 820/4-7, SPP1757; DD: SFB1089, SPP1757, INST1172 15, DI853/3-5&7, INST 217/785-1) and the BONFOR program of the Faculty of Medicine of Bonn University (SS, DD). We acknowledge the support of PRECISE—Platform for Single-Cell Genomics and Epigenomics (University of Bonn and the German Center for Neurodegenerative Diseases (DZNE) and of the Next Generation Sequencing Core Facility (Medical Faculty at the University of Bonn). Special thanks to Shane McGee McMahon for providing practical support on two-photon microscopy. We would like to thank Jessica Klemmer, Sabine Opitz and Julia Kaspari for their excellent technical assistance. Open Access funding enabled and organized by Projekt DEAL.

CONFLICT OF INTEREST STATEMENT

The authors declare no conflict of interests.

DATA AVAILABILITY STATEMENT

The data that support the findings of this study are available from the corresponding authors upon reasonable request.

ORCID

Wenjing Sun https://orcid.org/0000-0002-0905-7420
Susanne Schoch https://orcid.org/0000-0002-2046-2670

REFERENCES

Babicki, S., Arndt, D., Marcu, A., Liang, Y., Grant, J. R., Maciejewski, A., & Wishart, D. S. (2016). Heatmapper: Web-enabled heat mapping for all. *Nucleic Acids Research*, *44*(W1), W147–W153. https://doi.org/10.1093/nar/gkw419

Becht, E., McInnes, L., Healy, J., Dutertre, C.-A., Kwok, I. W. H., Ng, L. G., Ginhoux, F., & Newell, E. W. (2019). Dimensionality reduction for visualizing single-cell data using UMAP. *Nature Biotechnology*, *37*(1), 38–44. https://doi.org/10.1038/nbt.4314

Bergles, D. E., & Richardson, W. D. (2016). Oligodendrocyte development and plasticity. *Cold Spring Harbor Perspectives in Biology*, *8*(2), a020453. https://doi.org/10.1101/cshperspect.a020453

Bergles, D. E., Roberts, J. D., Somogyi, P., & Jahr, C. E. (2000). Glutamatergic synapses on oligodendrocyte precursor cells in the hippocampus. *Nature*, *405*(6783), 187–191. https://doi.org/10.1038/35012083

Berret, E., Barron, T., Xu, J., Debner, E., Kim, E. J., & Kim, J. H. (2017). Oligodendroglial excitability mediated by glutamatergic inputs and Nav1.2 activation. *Nature Communications*, *8*(1), 557. https://doi.org/10.1038/s41467-017-00688-0

Biase, L. M. D., Biase, L. M. D., Nishiyama, A., Nishiyama, A., Bergles, D. E., & Bergles, D. E. (2010). Excitability and synaptic communication within the oligodendrocyte lineage. *Journal of Neuroscience*, *30*(10), 3600–3611. https://doi.org/10.1523/jneurosci.6000-09.2010

Briata, P., Blas, E. D., Gulisano, M., Mallamaci, A., Iannone, R., Boncinelli, E., & Corte, G. (1996). EMX1 homeoprotein is expressed in cell nuclei of the developing cerebral cortex and in the axons of the olfactory sensory neurons. *Mechanisms of Development*, *57*(2), 169–180. https://doi.org/10.1016/0925-4773(96)00544-8

Call, C. L., Biase, L. M. D., & Bergles, D. E. (2020). Patterning and cell type specification in the developing CNS and PNS. *Comprehensive Developmental Neuroscience*, 891–918. https://doi.org/10.1016/b978-0-12-814405-3.00036-9

Calver, A. R., Hall, A. C., Yu, W.-P., Walsh, F. S., Heath, J. K., Betsholtz, C., & Richardson, W. D. (1998). Oligodendrocyte population dynamics and the role of PDGF In vivo. *Neuron*, *20*(5), 869–882. https://doi.org/10.1016/s0896-6273(00)80469-9

Chen, C., Chen, Y., Wang, J., Huang, Y., & Tai, C. (2017). Postsynaptic Y654 dephosphorylation of β-catenin modulates presynaptic vesicle turnover through increased n-cadherin-mediated transsynaptic signaling. *Developmental Neurobiology*, *77*(1), 61–74. https://doi.org/10.1002/dneu.22411

Chen, V. S., Morrison, J. P., Southwell, M. F., Foley, J. F., Bolon, B., & Elmore, S. A. (2017). Histology atlas of the developing prenatal and postnatal mouse central nervous system, with emphasis on prenatal days E7.5 to E18.5. *Toxicologic Pathology*, *45*(6), 705–744. https://doi.org/10.1177/0192623317728134

Chittajallu, R., Aguirre, A., & Gallo, V. (2004). NG2-positive cells in the mouse white and grey matter display distinct physiological properties. *The Journal of Physiology*, *561*(1), 109–122. https://doi.org/10.1113/jphysiol.2004.074252

Cristobal, C. D., & Lee, H. K. (2022). Development of myelinating glia: An overview. *Glia*, *70*(12), 2237–2259. https://doi.org/10.1002/glia.24238

Draffin, J. E., Sánchez-Castillo, C., Fernández-Rodrigo, A., Sánchez-Sáez, X., Ávila, J., Wagner, F. F., & Esteban, J. A. (2021). GSK3α, not GSK3β, drives hippocampal NMDAR-dependent LTD via tau-mediated spine anchoring. *The EMBO Journal*, *40*(2), e105513. https://doi.org/10.15252/embj.2020105513

Eden, E., Navon, R., Steinfeld, I., Lipson, D., & Yakhini, Z. (2009). GOrilla: A tool for discovery and visualization of enriched GO terms in ranked gene lists. *BMC Bioinformatics*, *10*(1), 48. https://doi.org/10.1186/1471-2105-10-48

Elazar, N., Vainshtein, A., Golan, N., Vijayaragavan, B., Schaeren-Wiemers, N., Eshed-Eisenbach, Y., & Peles, E. (2019). Axoglial adhesion by Cadm4 regulates CNS myelination. *Neuron*, *101*(2), 224–231.e5. https://doi.org/10.1016/j.neuron.2018.11.032

Fields, R. D., Dutta, D. J., Belgrad, J., & Robnett, M. (2017). Cholinergic signaling in myelination. *Glia*, *65*(5), 687–698. https://doi.org/10.1002/glia.23101

Foster, A. Y., Bujalka, H., & Emery, B. (2019). Axoglial interactions in myelin plasticity: Evaluating the relationship between neuronal activity and oligodendrocyte dynamics. *Glia*, *67*(11), 2038–2049. https://doi.org/10.1002/glia.23629

Frishberg, A., Peshes-Yaloz, N., Cohn, O., Rosentul, D., Steuerman, Y., Valadarsky, L., Yankovitz, G., Mandelboim, M., Iraqi, F. A., Amit, I., Mayo, L., Bacharach, E., & Gat-Viks, I. (2019). Cell composition analysis of bulk genomics using single-cell data. *Nature Methods*, *16*(4), 327–332. https://doi.org/10.1038/s41592-019-0355-5

Funa, K., & Sasahara, M. (2014). The roles of PDGF in development and during neurogenesis in the Normal and diseased nervous system. *Journal of Neuroimmune Pharmacology*, *9*(2), 168–181. https://doi.org/10.1007/s11481-013-9479-z

Furusho, M., Dupree, J. L., Nave, K.-A., & Bansal, R. (2012). Fibroblast growth factor receptor signaling in oligodendrocytes regulates myelin sheath thickness. *The Journal of Neuroscience*, *32*(19), 6631–6641. https://doi.org/10.1523/jneurosci.6005-11.2012

Gao, F.-B., & Raff, M. (1997). Cell size control and a cell-intrinsic maturation program in proliferating oligodendrocyte precursor cells. *The Journal of Cell Biology*, *138*(6), 1367–1377. https://doi.org/10.1083/jcb.138.6.1367

Ge, W.-P., Zhou, W., Luo, Q., Jan, L. Y., & Jan, Y. N. (2009). Dividing glial cells maintain differentiated properties including complex morphology and functional synapses. *Proceedings of the National Academy of Sciences*, *106*(1), 328–333. https://doi.org/10.1073/pnas.0811353106

Gibson, E. M., Purger, D., Mount, C. W., Goldstein, A. K., Lin, G. L., Wood, L. S., Inema, I., Miller, S. E., Bieri, G., Zuchero, J. B., Barres, B. A., Woo, P. J., Vogel, H., & Monje, M. (2014). Neuronal activity promotes oligodendrogenesis and adaptive myelination in the mammalian brain. *Science*, *344*(6183), 1252304. https://doi.org/10.1126/science.1252304

Griffiths, J. A., Richard, A. C., Bach, K., Lun, A. T. L., & Marioni, J. C. (2018). Detection and removal of barcode swapping in single-cell RNA-seq data. *Nature Communications*, *9*(1), 2667. https://doi.org/10.1038/s41467-018-05083-x

Gulisano, M., Broccoli, V., Pardini, C., & Boncinelli, E. (1996). Emx1 and Emx2 show different patterns of expression during proliferation and differentiation of the developing cerebral cortex in the mouse. *European Journal of Neuroscience*, *8*(5), 1037–1050. https://doi.org/10.1111/j.1460-9568.1996.tb01590.x

Haberlandt, C., Derouiche, A., Wyczynski, A., Haseleu, J., Pohle, J., Karram, K., Trotter, J., Seifert, G., Frotscher, M., Steinhäuser, C., & Jabs, R. (2011). Gray matter NG2 cells display multiple Ca2+-signaling pathways and highly motile processes. *PLoS One*, *6*(3), e17575. https://doi.org/10.1371/journal.pone.0017575.s006

Hafemeister, C., & Satija, R. (2019). Normalization and variance stabilization of single-cell RNA-seq data using regularized negative binomial regression. *Genome Biology*, *20*(1), 296. https://doi.org/10.1186/s13059-019-1874-1

Hao, Y., Hao, S., Andersen-Nissen, E., Mauck, W. M., Zheng, S., Butler, A., Lee, M. J., Wilk, A. J., Darby, C., Zager, M., Hoffman, P., Stoeckius, M., Papalexi, E., Mimitou, E. P., Jain, J., Srivastava, A., Stuart, T., Fleming, L. M., Yeung, B., … Satija, R. (2021). Integrated analysis of multimodal single-cell data. *Cell*, *184*(13), 3573–3587.e29. https://doi.org/10.1016/j.cell.2021.04.048

Harboe, M., Torvund-Jensen, J., Kjaer-Sorensen, K., & Laursen, L. S. (2018). Ephrin-A1-EphA4 signaling negatively regulates myelination in the central nervous system. *Glia*, *66*(5), 934–950. https://doi.org/10.1002/glia.23293

Hayashi, C., Suzuki, N., Mabuchi, Y., Kikura, N., Hosoda, Y., Vega, S. d., & Akazawa, C. (2020). The extracellular domain of teneurin-4 promotes cell adhesion for oligodendrocyte differentiation. *Biochemical and Biophysical Research Communications*, *523*(1), 171–176. https://doi.org/10.1016/j.bbrc.2019.12.002

Hochgerner, H., Zeisel, A., Lönnerberg, P., & Linnarsson, S. (2018). Conserved properties of dentate gyrus neurogenesis across postnatal development revealed by single-cell RNA sequencing. *Nature Neuroscience*, *21*(2), 290–299. https://doi.org/10.1038/s41593-017-0056-2

Hughes, A. N., & Appel, B. (2019). Oligodendrocytes express synaptic proteins that modulate myelin sheath formation. *Nature Communications*, *10*(1), 4125. https://doi.org/10.1038/s41467-019-12059-y

Káradóttir, R., Hamilton, N. B., Bakiri, Y., & Attwell, D. (2008). Spiking and nonspiking classes of oligodendrocyte precursor glia in CNS white matter. *Nature Neuroscience*, *11*(4), 450–456. https://doi.org/10.1038/nn2060

Káradóttir, R. T., & Kuo, C. T. (2016). Neuronal activity-dependent control of postnatal neurogenesis and gliogenesis. *Annual Review of Neuroscience*, *41*(1), 1–23. https://doi.org/10.1146/annurev-neuro-072116-031054

Kessaris, N., Fogarty, M., Iannarelli, P., Grist, M., Wegner, M., & Richardson, W. D. (2006). Competing waves of oligodendrocytes in the forebrain and postnatal elimination of an embryonic lineage. *Nature Neuroscience*, *9*(2), 173–179. https://doi.org/10.1038/nn1620

Kilb, W., Kirischuk, S., & Luhmann, H. J. (2011). Electrical activity patterns and the functional maturation of the neocortex. *European Journal of Neuroscience*, *34*(10), 1677–1686. https://doi.org/10.1111/j.1460-9568.2011.07878.x

Koopmans, F., Van Nierop, P., Andres-Alonso, M., Byrnes, A., Cijsouw, T., Coba, M. P., Cornelisse, L. N., Farrell, R. J., Goldschmidt, H. L., Howrigan, D. P., Hussain, N. K., Imig, C., de Jong, A. P. H., Jung, H., Kohansalnodehi, M., Kramarz, B., Lipstein, N., Lovering, R. C., MacGillavry, H., … Verhage, M. (2019). SynGO: An evidence-based, expert-curated Knowledge Base for the synapse. *Neuron*, *103*(2), 217–234.e4. https://doi.org/10.1016/j.neuron.2019.05.002

Kukley, M., Capetillo-Zarate, E., & Dietrich, D. (2007). Vesicular glutamate release from axons in white matter. *Nature Neuroscience*, *10*(3), 311–320. https://doi.org/10.1038/nn1850

Kukley, M., Kiladze, M., Tognatta, R., Hans, M., Swandulla, D., Schramm, J., & Dietrich, D. (2008). Glial cells are born with synapses. *The FASEB Journal*, *22*(8), 2957–2969. https://doi.org/10.1096/fj.07-090985

Kukley, M., Nishiyama, A., & Dietrich, D. (2010). The fate of synaptic input to NG2 glial cells: Neurons specifically downregulate transmitter release onto differentiating oligodendroglial cells. *Journal of Neuroscience*, *30*(24), 8320–8331. https://doi.org/10.1523/jneurosci.0854-10.2010

Lamprianou, S., Chatzopoulou, E., Thomas, J.-L., Bouyain, S., & Harroch, S. (2011). A complex between contactin-1 and the protein tyrosine phosphatase PTPRZ controls the development of oligodendrocyte precursor cells. *Proceedings of the National Academy of Sciences*, *108*(42), 17498–17503. https://doi.org/10.1073/pnas.1108774108

Laursen, L. S., Chan, C. W., & French-Constant, C. (2009). An integrin–contactin complex regulates CNS myelination by differential Fyn phosphorylation. *The Journal of Neuroscience*, *29*(29), 9174–9185. https://doi.org/10.1523/jneurosci.5942-08.2009

Lin, S., & Bergles, D. E. (2003). Synaptic signaling between GABAergic interneurons and oligodendrocyte precursor cells in the hippocampus. *Nature Neuroscience*, *7*(1), 24–32. https://doi.org/10.1038/nn1162

Linneberg, C., Harboe, M., & Laursen, L. S. (2015). Axo-glia interaction preceding CNS myelination is regulated by bidirectional Eph-ephrin signaling. *ASN Neuro*, *7*(5), 175909141560285. https://doi.org/10.1177/1759091415602859

Lun, A. T. L., Riesenfeld, S., Andrews, T., Dao, T. P., Gomes, T., & Marioni, J. C. (2019). EmptyDrops: Distinguishing cells from empty droplets in droplet-based single-cell RNA sequencing data. *Genome Biology*, *20*(1), 63. https://doi.org/10.1186/s13059-019-1662-y

Maldonado, P. P., Velez-Fort, M., Levavasseur, F., & Angulo, M. C. (2013). Oligodendrocyte precursor cells are accurate sensors of local K+ in mature gray matter. *Journal of Neuroscience*, *33*(6), 2432–2442. https://doi.org/10.1523/jneurosci.1961-12.2013

Manno, G. L., Siletti, K., Furlan, A., Gyllborg, D., Vinsland, E., Albiach, A. M., Langseth, C. M., Khven, I., Lederer, A. R., Dratva, L. M., Johnsson, A., Nilsson, M., Lönnerberg, P., & Linnarsson, S. (2021). Molecular architecture of the developing mouse brain. *Nature*, *596*(7870), 92–96. https://doi.org/10.1038/s41586-021-03775-x

Marisca, R., Hoche, T., Agirre, E., Hoodless, L. J., Barkey, W., Auer, F., Castelo-Branco, G., & Czopka, T. (2020). Functionally distinct subgroups of oligodendrocyte precursor cells integrate neural activity and execute myelin formation. *Nature Neuroscience*, *23*(3), 363–374. https://doi.org/10.1038/s41593-019-0581-2

Marques, S., van Bruggen, D., Vanichkina, D. P., Floriddia, E. M., Munguba, H., Väremo, L., Giacomello, S., Falcão, A. M., Meijer, M., Björklund, Å. K., Hjerling-Leffler, J., Taft, R. J., & Castelo-Branco, G. (2018). Transcriptional convergence of oligodendrocyte lineage progenitors during development. *Developmental Cell*, *46*(4), 504–517.e7. https://doi.org/10.1016/j.devcel.2018.07.005

McGinnis, C. S., Murrow, L. M., & Gartner, Z. J. (2019). DoubletFinder: Doublet detection in single-cell RNA sequencing data using artificial nearest neighbors. *Cell Systems*, *8*(4), 329–337.e4. https://doi.org/10.1016/j.cels.2019.03.003

Mitew, S., Gobius, I., Fenlon, L. R., McDougall, S. J., Hawkes, D., Xing, Y. L., Bujalka, H., Gundlach, A. L., Richards, L. J., Kilpatrick, T. J., Merson, T. D., & Emery, B. (2018). Pharmacogenetic stimulation of neuronal activity increases myelination in an axon-specific manner. *Nature Communications*, *9*(1), 1–16. https://doi.org/10.1038/s41467-017-02719-2

Nishiyama, A., Lin, X. H., Giese, N., Heldin, C. H., & Stallcup, W. B. (1996). Co-localization of NG2 proteoglycan and PDGF alpha-receptor on O2A progenitor cells in the developing rat brain. *Journal of Neuroscience Research*, *43*(3), 299–314.

Okada, A., Tominaga, M., Horiuchi, M., & Tomooka, Y. (2007). Plexin-A4 is expressed in oligodendrocyte precursor cells and acts as a mediator of semaphorin signals. *Biochemical and Biophysical Research Communications*, *352*(1), 158–163. https://doi.org/10.1016/j.bbrc.2006.10.176

Oumesmar, B. N., Vignais, L., Duhamel-Clerin, E., Avellana-Adalid, V., Rougon, G., & Evercooren, A. B. (1995). Expression of the highly Polysialylated neural cell adhesion molecule during postnatal myelination and following chemically induced demyelination of the adult mouse spinal cord. *European Journal of Neuroscience*, *7*(3), 480–491. https://doi.org/10.1111/j.1460-9568.1995.tb00344.x

Paez, P. M., & Lyons, D. A. (2020). Calcium signaling in the oligodendrocyte lineage: Regulators and consequences. *Annual Review of Neuroscience*, *43*(1), 1–24. https://doi.org/10.1146/annurev-neuro-100719-093305

Passlick, S., Trotter, J., Seifert, G., Steinhäuser, C., & Jabs, R. (2016). The NG2 protein is not required for glutamatergic neuron–NG2 cell synaptic signaling. *Cerebral Cortex*, *26*(1), 51–57. https://doi.org/10.1093/cercor/bhu171

Picelli, S., Faridani, O.R., Björklund, Å.K., Winberg, G., Sagasser, S., and Sandberg, R. (2014). Full-length RNA-seq from single cells using Smart-seq2. *Nature Protoc. 9*, 171–181. https://doi.org/10.1038/nprot.2014.006.

Pitman, K. A., Ricci, R., Gasperini, R., Beasley, S., Pavez, M., Charlesworth, J., Foa, L., & Young, K. M. (2020). The voltage-gated calcium channel CaV1.2 promotes adult oligodendrocyte progenitor cell survival in the mouse corpus callosum but not motor cortex. *Glia*, *68*(2), 376–392. https://doi.org/10.1002/glia.23723

Pringle, N. P., & Richardson, W. D. (1993). A singularity of PDGF alpha-receptor expression in the dorsoventral axis of the neural tube may

define the origin of the oligodendrocyte lineage. *Development*, *117*(2), 525–533. https://doi.org/10.1242/dev.117.2.525

Reynolds, R., & Wilkin, G. P. (1988). Development of macroglial cells in rat cerebellum II. An in situ immunohistochemical study of oligodendroglial lineage from precursor to mature myelinating cell. *Development*, *102*(2), 409–425. https://doi.org/10.1242/dev.102.2.409

Schindelin, J., Arganda-Carreras, I., Frise, E., Kaynig, V., Longair, M., Pietzsch, T., Preibisch, S., Rueden, C., Saalfeld, S., Schmid, B., Tinevez, J.-Y., White, D. J., Hartenstein, V., Eliceiri, K., Tomancak, P., & Cardona, A. (2012). Fiji: An open-source platform for biological-image analysis. *Nature Methods*, *9*(7), 676–682. https://doi.org/10.1038/nmeth.2019

Simon, C., Götz, M., & Dimou, L. (2011). Progenitors in the adult cerebral cortex: Cell cycle properties and regulation by physiological stimuli and injury. *Glia*, *59*(6), 869–881. https://doi.org/10.1002/glia.21156

Spitzer, S. O., Sitnikov, S., Kamen, Y., Evans, K. A., Kronenberg-Versteeg, D., Dietmann, S., de Faria, O., Agathou, S., & Káradóttir, R. T. (2019). Oligodendrocyte progenitor cells become regionally diverse and heterogeneous with age. *Neuron*, *101*(3), 459–471.e5. https://doi.org/10.1016/j.neuron.2018.12.020

Stout, K. A., Dunn, A. R., Hoffman, C., & Miller, G. W. (2019). The synaptic vesicle glycoprotein 2: Structure, function, and disease relevance. *ACS Chemical Neuroscience*, *10*(9), 3927–3938. https://doi.org/10.1021/acschemneuro.9b00351

Stuart, T., Butler, A., Hoffman, P., Hafemeister, C., Papalexi, E., Mauck, W. M., Hao, Y., Stoeckius, M., Smibert, P., & Satija, R. (2019). Comprehensive integration of single-cell data. *Cell*, *177*(7), 1888–1902.e21. https://doi.org/10.1016/j.cell.2019.05.031

Südhof, T. C. (2018). Towards an understanding of synapse formation. *Neuron*, *100*(2), 276–293. https://doi.org/10.1016/j.neuron.2018.09.040

Südhof, T. C. (2021). The cell biology of synapse formation. *Journal of Cell Biology*, *220*(7), e202103052. https://doi.org/10.1083/jcb.202103052

Sun, W., & Dietrich, D. (2013). Synaptic integration by NG2 cells. *Frontiers in Cellular Neuroscience*, *7*, 255. https://doi.org/10.3389/fncel.2013.00255

Sun, W., Matthews, E. A., Nicolas, V., Schoch, S., & Dietrich, D. (2016). NG2 glial cells integrate synaptic input in global and dendritic calcium signals. *eLife*, *5*, 1812. https://doi.org/10.7554/elife.16262

Tognatta, R., Sun, W., Goebbels, S., Nave, K., Nishiyama, A., Schoch, S., Dimou, L., & Dietrich, D. (2017). Transient Cnp expression by early progenitors causes Cre-lox-based reporter lines to map profoundly different fates. *Glia*, *65*(2), 342–359. https://doi.org/10.1002/glia.23095

Toran-Allerand, C. D. (1974). Acetylcholinesterase inhibition and myelinogenesis in vitro. *Experimental Neurology*, *43*(1), 216–226. https://doi.org/10.1016/0014-4886(74)90142-3

Trapp, B. D., Nishiyama, A., Cheng, D., & Macklin, W. (1997). Differentiation and death of Premyelinating oligodendrocytes in developing rodent brain. *The Journal of Cell Biology*, *137*(2), 459–468. https://doi.org/10.1083/jcb.137.2.459

Trudeau, L. E., Doyle, R. T., Emery, D. G., & Haydon, P. G. (1996). Calcium-independent activation of the secretory apparatus by ruthenium red in hippocampal neurons: A new tool to assess modulation of presynaptic function. *The Journal of Neuroscience: The Official Journal of the Society for Neuroscience*, *16*(1), 46–54.

Van Heyningen, P., Calver, A. R., & Richardson, W. D. (2001). Control of progenitor cell number by mitogen supply and demand. *Current Biology*, *11*(4), 232–241. https://doi.org/10.1016/s0960-9822(01)00075-6

Vartanian, T., Fischbach, G., & Miller, R. (1999). Failure of spinal cord oligodendrocyte development in mice lacking neuregulin. *Proceedings of the National Academy of Sciences*, *96*(2), 731–735. https://doi.org/10.1073/pnas.96.2.731

Venkatesh, H. S., Johung, T. B., Caretti, V., Noll, A., Tang, Y., Nagaraja, S., Gibson, E. M., Mount, C. W., Polepalli, J., Mitra, S. S., Woo, P. J., Malenka, R. C., Vogel, H., Bredel, M., Mallick, P., & Monje, M. (2015). Neuronal activity promotes glioma growth through neuroligin-3 secretion. *Cell*, *161*(4), 803–816. https://doi.org/10.1016/j.cell.2015.04.012

Venkatesh, H. S., Tam, L. T., Woo, P. J., Lennon, J., Nagaraja, S., Gillespie, S. M., Ni, J., Duveau, D. Y., Morris, P. J., Zhao, J. J., Thomas, C. J., & Monje, M. (2017). Targeting neuronal activity-regulated neuroligin-3 dependency in high-grade glioma. *Nature*, *549*(7673), 533–537. https://doi.org/10.1038/nature24014

Weng, Q., Wang, J., Wang, J., He, D., Cheng, Z., Zhang, F., Verma, R., Xu, L., Dong, X., Liao, Y., He, X., Potter, A., Zhang, L., Zhao, C., Xin, M., Zhou, Q., Aronow, B. J., Blackshear, P. J., Rich, J. N., … Lu, Q. R. (2019). Single-cell transcriptomics uncovers glial progenitor diversity and cell fate determinants during development and Gliomagenesis. *Cell Stem Cell*, *24*(5), 707–723.e8. https://doi.org/10.1016/j.stem.2019.03.006

Winkler, C. C., Yabut, O. R., Fregoso, S. P., Gomez, H. G., Dwyer, B. E., Pleasure, S. J., & Franco, S. J. (2018). The dorsal wave of neocortical Oligodendrogenesis begins embryonically and requires multiple sources of sonic hedgehog. *The Journal of Neuroscience*, *38*(23), 5237–5250. https://doi.org/10.1523/jneurosci.3392-17.2018

Xiang, X., Zhang, X., & Huang, Q.-L. (2012). Plexin A3 is involved in semaphorin 3F-mediated oligodendrocyte precursor cell migration. *Neuroscience Letters*, *530*(2), 127–132. https://doi.org/10.1016/j.neulet.2012.09.058

Xiao, L., Ohayon, D., McKenzie, I. A., Sinclair-Wilson, A., Wright, J. L., Fudge, A. D., Emery, B., Li, H., & Richardson, W. D. (2016). Rapid production of new oligodendrocytes is required in the earliest stages of motor skill learning. *Nature Neuroscience*, *19*(9), 1210–1217. https://doi.org/10.1038/nn.4351

Xie, M., Lynch, D. T., Schools, G. P., Feustel, P. J., Kimelberg, H. K., & Zhou, M. (2007). Sodium channel currents in rat hippocampal NG2 glia: Characterization and contribution to resting membrane potential. *Neuroscience*, *150*(4), 853–862. https://doi.org/10.1016/j.neuroscience.2007.09.057

Yuan, X., Chittajallu, R., Belachew, S., Anderson, S., McBain, C. J., & Gallo, V. (2002). Expression of the green fluorescent protein in the oligodendrocyte lineage: A transgenic mouse for developmental and physiological studies. *Journal of Neuroscience Research*, *70*(4), 529–545. https://doi.org/10.1002/jnr.10368

Yuzwa, S. A., Borrett, M. J., Innes, B. T., Voronova, A., Ketela, T., Kaplan, D. R., Bader, G. D., & Miller, F. D. (2017). Developmental emergence of adult neural stem cells as revealed by single-cell transcriptional profiling. *Cell Reports*, *21*(13), 3970–3986. https://doi.org/10.1016/j.celrep.2017.12.017

Zhao, N., Huang, W., Cătălin, B., Scheller, A., & Kirchhoff, F. (2021). L-type Ca2+ channels of NG2 glia determine proliferation and NMDA receptor-dependent plasticity. *Frontiers in Cell and Developmental Biology*, *9*, 759477. https://doi.org/10.3389/fcell.2021.759477

Zheng, G. X. Y., Terry, J. M., Belgrader, P., Ryvkin, P., Bent, Z. W., Wilson, R., Ziraldo, S. B., Wheeler, T. D., McDermott, G. P., Zhu, J., Gregory, M. T., Shuga, J., Montesclaros, L., Underwood, J. G., Masquelier, D. A., Nishimura, S. Y., Schnall-Levin, M., Wyatt, P. W., Hindson, C. M., … Bielas, J. H. (2017). Massively parallel digital transcriptional profiling of single cells. *Nature Communications*, *8*(1), 14049. https://doi.org/10.1038/ncomms14049

Zhu, X., Bergles, D. E., & Nishiyama, A. (2008). NG2 cells generate both oligodendrocytes and gray matter astrocytes. *Development*, *135*(1), 145–157. https://doi.org/10.1242/dev.004895

Ziskin, J. L., Nishiyama, A., Rubio, M., Fukaya, M., & Bergles, D. E. (2007). Vesicular release of glutamate from unmyelinated axons in white matter. *Nature Neuroscience*, *10*(3), 321–330. https://doi.org/10.1038/nn1854

Zonouzi, M., Scafidi, J., Li, P., McEllin, B., Edwards, J., Dupree, J. L., Harvey, L., Sun, D., Hübner, C. A., Cull-Candy, S. G., Farrant, M., &

Gallo, V. (2015). GABAergic regulation of cerebellar NG2 cell development is altered in perinatal white matter injury. *Nature Neuroscience*, *18*(5), 674–682. https://doi.org/10.1038/nn.3990

SUPPORTING INFORMATION

Additional supporting information can be found online in the Supporting Information section at the end of this article.

Received: 14 March 2022 | Revised: 11 January 2023 | Accepted: 30 January 2023

DOI: 10.1111/acel.13794

Aging Cell WILEY

RESEARCH ARTICLE

MiR-181a-5p promotes neural stem cell proliferation and enhances the learning and memory of aged mice

Qiaoyi Sun | Li Ma | Jing Qiao | Xing Wang | Jianguo Li | Yuxi Wang | Ailing Tan | Zihui Ye | Yukang Wu | Jiajie Xi | Jiuhong Kang

Clinical and Translational Research Center of Shanghai First Maternity and Infant Hospital, Shanghai Key Laboratory of Maternal Fetal Medicine, Shanghai Key Laboratory of Signaling and Disease Research, Frontier Science Center for Stem Cell Research, National Stem Cell Translational Resource Center, School of Life Sciences and Technology, Tongji University, Shanghai, China

Correspondence
Jiuhong Kang and Jiajie Xi, Clinical and Translational Research Center of Shanghai First Maternity and Infant Hospital, Shanghai Key Laboratory of Maternal Fetal Medicine, Shanghai Key Laboratory of Signaling and Disease Research, Frontier Science Center for Stem Cell Research, National Stem Cell Translational Resource Center, School of Life Sciences and Technology, Tongji University, Shanghai, 200092, China.
Email: jhkang@tongji.edu.cn; jiajiexi_bio@163.com

Funding information
National Natural Science Foundation of China, Grant/Award Number: 82230054, 31721003, 32270591 and 32070617; National Key R&D Program of China, Grant/Award Number: 2021YFA1100400 and 2020YFA0113101

Abstract

Hippocampal neural stem cell (NSC) proliferation is known to decline with age, which is closely linked to learning and memory impairments. In the current study, we found that the expression level of miR-181a-5p was decreased in the hippocampal NSCs of aged mice and that exogenous overexpression of miR-181a-5p promoted NSC proliferation without affecting NSC differentiation into neurons and astrocytes. The mechanistic study revealed that phosphatase and tensin homolog (PTEN), a negative regulator of the AKT signaling pathway, was the target of miR-181a-5p and knockdown of PTEN could rescue the impairment of NSC proliferation caused by low miR-181a-5p levels. Moreover, overexpression of miR-181a-5p in the dentate gyrus enhanced the proliferation of NSCs and ameliorated learning and memory impairments in aged mice. Taken together, our findings indicated that miR-181a-5p played a functional role in NSC proliferation and aging-related, hippocampus-dependent learning and memory impairments.

KEYWORDS
aging, hippocampus, miR-181a-5p, neural stem cells, PTEN

1 | INTRODUCTION

Aging is a progressive degenerative state that is often accompanied by cognitive deterioration and memory deficits. The hippocampus is a brain region closely related to spatial learning and memory. Adult neural stem cells (NSCs), which are located in the subgranular zone (SGZ) of the dentate gyrus (DG) in the hippocampus, play important roles in the function of the hippocampus (Ma et al., 2009). NSCs have the ability to proliferate, either generating two NSCs to maintain NSC pools through symmetric division or generating one NSC and one neural progenitor cell (NPC) through asymmetric division. NPCs then further differentiate into

particular cell types, such as neurons or astrocytes (Bonaguidi et al., 2011; Bond et al., 2015; Temple, 1989). Studies on rodents have shown that proliferation and neurogenesis of NSCs persist throughout the lifespan; however, adult neurogenesis decreases with age (Ben Abdallah et al., 2010; Kuhn et al., 1996), and this decrease is involved in cognitive and memory declines, indicating that abnormalities in hippocampal NSCs are one of the main causes of age-related deterioration in hippocampus-dependent cognition (Berdugo-Vega et al., 2020; Drapeau & Abrous, 2008). Whether adult hippocampal neurogenesis persists in adult and aged humans and whether there is sufficient generation of neurons in adult humans to contribute to brain function remains extensively debated due to the time interval of postmortem sampling and the difference in tissue processing methods (Kempermann et al., 2018; Moreno-Jimenez et al., 2019; Sorrells et al., 2018). Therefore, understanding the molecular mechanisms underlying aging-related hippocampal NSC abnormalities is important for developing therapeutic strategies to overcome aging-related cognitive deterioration and memory deficits.

Proliferation and neurogenesis of NSCs are exquisitely regulated by extrinsic and intrinsic factors (Bond et al., 2015; Navarro Negredo et al., 2020), including secreted molecules, neurotransmitters, transcription factors (Ahmad et al., 2019), and epigenetic regulators (Wang et al., 2018). Among these, miRNAs, which are enriched in the brain, have been shown to be widely involved in the regulation of NSC proliferation and differentiation (Lopez-Ramirez & Nicoli, 2014; Walgrave et al., 2021). MiR-218-2 targets complement component 3 (C3) to regulate presynaptic glutamate release and synaptic plasticity in mouse hippocampal neurons and then bidirectionally regulates learning and memory in mice (Lu, Fu, et al., 2021). Increased expression of miRNA let-7b during aging could repress Hmga2 expression and contribute to declining self-renewal of NSCs (Tzatsos & Bardeesy, 2008). Our previous study also found that MiR-153 promoted neurogenesis and increased the cognitive ability of aged mice by directly targeting the Notch signaling pathway key factors Jag1 and Hey2 (Qiao et al., 2020). Together, these studies clearly indicate that miRNAs play important roles in NSC proliferation and differentiation, whereas the function of many miRNAs that are highly expressed in NSCs is still unclear.

Phosphatase and tensin homolog (PTEN) is a lipid and protein phosphatase that acts as a negative regulator of the phosphatidylinositol-3 kinase (PI3K)-AKT pathway. Previous studies have shown that PTEN plays critical roles in regulating tumor cell proliferation, migration, and death (Cristofano et al., 1998; He et al., 2007). PTEN also regulates the neural system. Mice lacking PTEN exhibited increased cell proliferation, decreased cell death, and enlarged cell sizes, resulting in enlarged, histoarchitecturally abnormal brains (Groszer et al., 2001). Loss of PTEN enhances the self-renewal capacity of NSCs while maintaining multilineage cell differentiation potential (Groszer et al., 2001, 2006). Although PTEN plays important roles in NSC self-renewal and proliferation, whether it influences NSC proliferation and learning and memory deficits in the aged hippocampus is still unclear.

In this study, we found that miR-181a-5p is downregulated in the hippocampal NSCs of aging mice and mediates the aging-related, hippocampus-dependent impairments of learning and memory. Moreover, overexpression of miR-181a-5p in the aged mouse hippocampus could ameliorate its impaired cognitive abilities.

2 | RESULTS

2.1 | MiR-181a-5p decreases with aging in the mouse hippocampus

To evaluate the learning and memory abilities of aged mice, we conducted behavioral tests: the novel object recognition (NOR) test and the Morris water maze (MWM) test (Figure S1a). In the NOR test, no obvious differences in recognition of the two objects were observed between young and aged mice (Figure S1b), but the discrimination index and the discrimination ratio of novel objects were reduced in the aged mice (Figure S1c,d). In the MWM test, compared with young mice, aged mice took longer to locate the hidden platform, crossed the hidden platform fewer times, and spent less time in the goal quadrant (Figure S1e–h), although there was no significant difference in swimming speed or distance between the two groups (Figure S1i,j). When we detected the proliferation abilities of NSCs in the mouse hippocampus, we found that the expression of Ki67 and the number of $Ki67^+/Sox2^+$ NSCs decreased in aged mice (Figure S1k, Figure 1a,b). In BrdU incorporation analysis, the number of $BrdU^+/Sox2^+$ cells, which indicates the number of proliferating NSCs during the period of BrdU administration (Figure S1a), also decreased in aged mice (Figure 1c,d). These results demonstrate that the proliferation ability of hippocampal NSCs decreased with aging.

As miRNAs play key roles in the regulation of NSC proliferation, we analyzed differentially expressed miRNAs in the whole brains of young and aged mice (GSE34393) with the top 20 highly expressed miRNAs in the hippocampus of mice (GSE107496) and identified 4 miRNAs, let-7f-5p, miR-101a-3p, miR-181a-5p, and miR-127-3p, as the candidates (Figure S1l). Among these 4 miRNAs, only miR-181a-5p was decreased in the hippocampus of aged mice (Figure 1e and S1m), and its expression level was positively correlated with the extent of Ki67 expression (Figure 1f). These data indicate that miR-181a-5p deficiency may be associated with the decreased proliferation ability of aged hippocampal NSCs.

We next assessed miR-181a-5p localization in the dentate gyrus. We employed in situ hybridization in conjunction with cell-specific markers to label NSCs, neurons, and astrocytes, hybridization with RNU6 and scramble probes were used as positive and negative controls, respectively (Figure S1n). The results showed that miR-181a-5p is mainly expressed in $SOX2^+$ NSCs and $NEUN^+$ neurons (Figure 1g). To evaluate the age-related changes of miR-181a-5p in NSCs and neurons, we injected rAAVs containing Nestin promoter-driven green fluorescent protein (Nestin-GFP) or Synapsin promoter-driven green fluorescent protein (Syn-GFP) into the hippocampus and used FACS to isolate GFP-positive cells

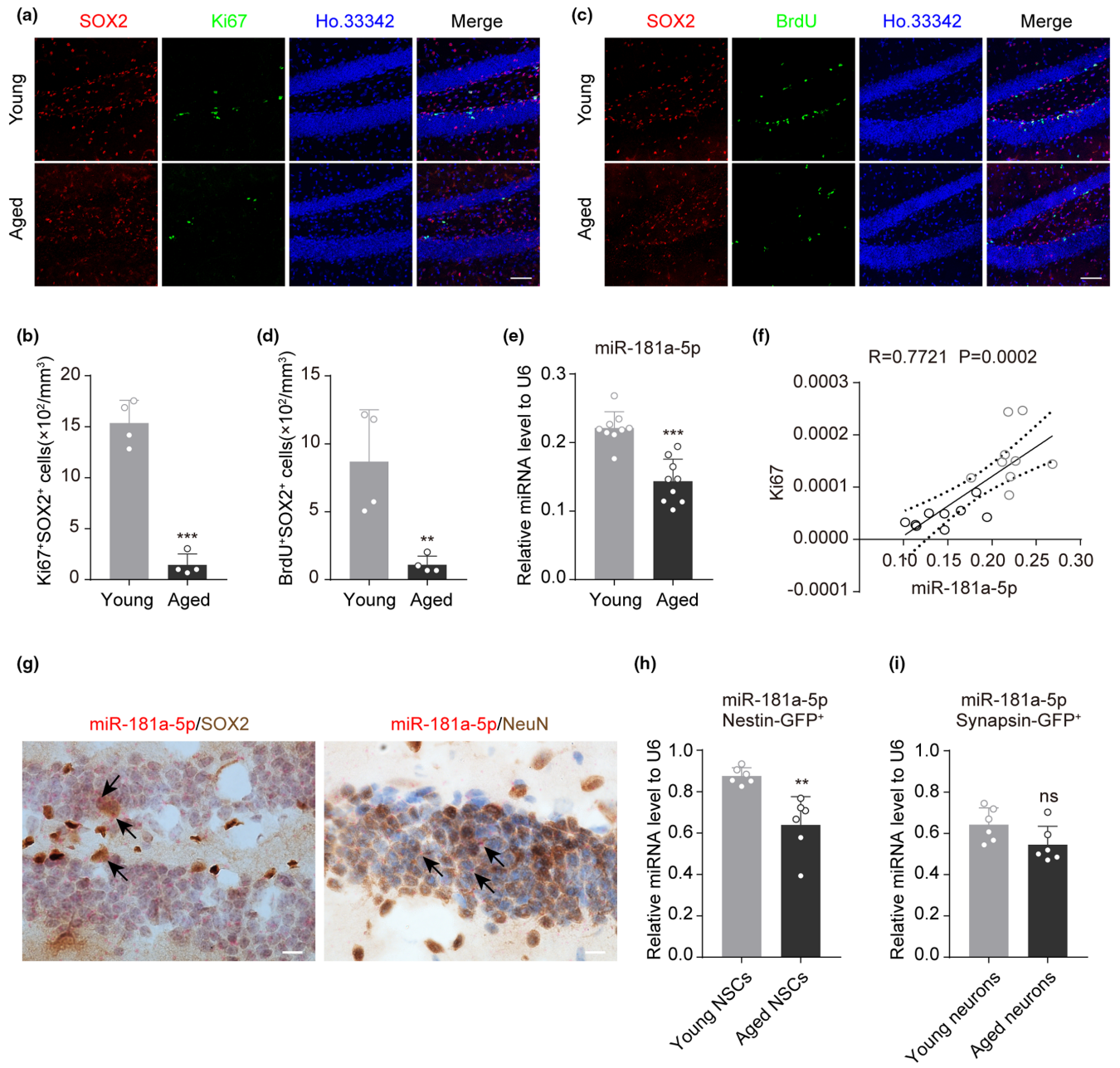

FIGURE 1 MiR-181a-5p decreases in the hippocampi of aged mice. (a,b) Representative images of Ki67 (green), SOX2 (red), and Ho.33342 (blue) in the DG of young and aged mice (a) and quantification of the number of $Ki67^+SOX2^+Ho.33342^+$ cells in the DG (b). Scale bars, 50 μm ($n = 4$ per group). (c,d) Representative images of BrdU (green), SOX2 (red), and Ho.33342 (blue) in the DG of young and aged mice (c) and quantification of the number of $BrdU^+SOX2^+Ho.33342^+$ cells in the DG (d). Scale bars, 50 μm ($n = 4$ per group). (e) qRT–PCR analysis of the expression of miR-181a-5p in the hippocampus of young and aged mice. U6 was used as the internal control ($n = 9$ per group). (f) The correlation analysis for miR-181a-5p and Ki67. (g) Representative images of miR-181a-5p in situ hybridization coupled to SOX2 or NeuN immunohistochemical staining in the dentate gyrus of 3-month-old WT mice. Black arrows show miR-181a-5p positive dots. Scale bars: 5 μm. (h) qRT–PCR analysis of the expression of miR-181a-5p in Nestin-GFP^+ populations sorted from the dentate gyrus of young and aged mice ($n = 6$ per group). (i) qRT–PCR analysis of the expression of miR-181a-5p in Syn-GFP^+ populations sorted from the dentate gyrus of young and aged mice ($n = 6$ per group). $^*p < 0.05$, $^{**}p < 0.01$, $^{***}p < 0.001$, ns: not significant. Values are presented as mean ± SD. Student's t test was used in (b), (d), (e), (h), and (i). Pearson correlation test was used in (f). See also Figure S1.

from the dentate gyrus of young and aged mice. The qRT–PCR assay showed that miR-181a-5p was decreased in the Nestin-GFP^+ NSCs of aged mice (Figure 1h) but unchanged in Syn-GFP^+ neurons (Figure 1i), indicating that miR-181a-5p may mainly play its regulatory role in NSCs.

2.2 | MiR-181a-5p promotes NSC proliferation without affecting its differentiation potential

To determine the role of miR-181a-5p in NSCs, we isolated NSCs from the forebrains of E13.5 mice for in vitro experiments. Following

culture, the percentage of Ki67/Sox2 double-positive cells decreased in late-passage NSCs compared with early-passage NSCs (Figure S2a). The BrdU incorporation analysis showed similar results (Figure S2b). These experiments indicate that the proliferation ability of NSCs decreased following passage. In addition, the expression of miR-181a-5p in NSCs was also decreased following passage (Figure S2c). We then constructed a ubiquitin promoter-miR-181a-5p sponge-WPRE lentivirus (181a sp) and infected early-passage NSCs. The infect effect was validated by flow cytometry (Figure S2d). The expression level of miR-181a-5p was validated by qRT–PCR (Figure 2a). The expression of the miR-181a-5p sponge in early-passage NSCs resulted in smaller neurospheres and a low cell proliferation rate (Figure 2b,c). The percentage of Ki67/Sox2 or BrdU/Sox2 double-positive cells was also decreased in the 181a sp group (Figure 2d,e). To further confirm the inhibitory effect of miR-181a-5p on NSC proliferation, we transfected early-passage NSCs with a miR-181a-5p inhibitor. The transfected effect was validated by flow cytometry (Figure S2e), and the inhibitory efficiency of miR-181a-5p inhibitor was validated by qRT–PCR (Figure S2f). Similar results to those of the 181a sp group in the neurosphere diameters and the cell proliferation curve, as well as the percentages of BrdU/Sox2 and Ki67/Sox2 double-positive cells were observed in miR-181a-5p inhibitor group (Figure S2g–j).

Then, we constructed an overexpression lentivirus (181a OE) and infected late-passage NSCs. The expression level of miR-181a-5p increased in the 181a OE group (Figure 2f), and this expression resulted in larger neurospheres and a higher proliferation rate in late-passage NSCs (Figure 2g,h). The percentage of Ki67/Sox2 or BrdU/Sox2 double-positive cells was also increased in the 181a OE group (Figure 2i,j). Similar results were obtained when late-passage NSCs were transfected with miR-181a-5p mimics (Figure S2k–o). In addition, annexin/PI staining analysis showed that neither overexpression nor inhibition of miR-181a-5p induced NSC apoptosis (Figure S3a–d).

To further confirm the effect of miR-181a-5p on NSC proliferation, we isolated adult hippocampal NSCs. The expression level of miR-181a-5p was lower in the adult hippocampal NSCs than in the E13.5 NSCs (Figure 2k). Similar as in E13.5 NSCs, transfecting adult hippocampal NSCs with miR-181a-5p mimics resulted in larger neurospheres and a higher percentage of Ki67/Sox2 or BrdU/Sox2 double-positive cells (Figure 2l–o).

Previous studies have shown that a few miRNAs, such as miR-195 and miR-184, can promote NSC proliferation but inhibit its differentiation potential (Liu et al., 2010, 2013). To determine whether miR-181a-5p affects the differentiation of NSCs, the neurospheres were dissociated into single cells and attached to glass coverslips for 48 h. qRT–PCR showed that neither overexpression of the miR-181a-5p sponge nor overexpression of miR-181a-5p affected the mRNA levels of the neuron-related genes Map2 and Tubb3 or the astrocyte-related genes GFAP and S100β (Figure 3a,b). Immunofluorescence staining also showed that it had no difference in the percentage of $MAP2^+$ or $GFAP^+$ cells in the control, 181a sp group (Figure 3c–e) and 181a OE group (Figure 3f–h). These data indicate that miR-181a-5p can promote NSC proliferation and does not affect its differentiation potential.

2.3 | PTEN is the functional target of miR-181a-5p in NSC proliferation

To study how miR-181a-5p regulates NSC proliferation, we used the miRDB and miRWalk databases to predict the potential target genes of miR-181a-5p and then compared those target genes with aging-related genes from Aging Atlas (AA) gene set (Aging Atlas, 2021).

FIGURE 2 MiR-181a-5p is important for NSC proliferation. (a) qRT–PCR analysis the expression of miR-181a-5p in early-passage NSCs infected with control (ctrl) or miR-181a-5p sponge (181 sp) viruses. U6 was used as the internal control. (b) Representative images of early-passage neurospheres infected with ctrl or 181a sp viruses (left) and quantification of neurosphere diameters (right). Scale bars, 100 μm. (c) Number of cells at 24 h, 48 h, and 72 h after early-passage NSCs were infected with ctrl or 181a sp viruses. (d) Representative images of Ki67 (green) and SOX2 (red) after early-passage NSCs were infected with ctrl or 181a sp viruses (left) and the proportion of $Ki67^+SOX2^+$ cells among all $SOX2^+$ cells (right). Scale bars, 100 μm. (e) Representative images of BrdU (green) and SOX2 (red) after early-passage NSCs were infected with ctrl or 181a sp viruses (left) and the proportion of $BrdU^+SOX2^+$ cells among all $SOX2^+$ cells (right). Scale bars, 100 μm. (f) qRT–PCR analysis of the overexpression efficiency of miR-181a-5p after late-passage NSCs were infected with control (ctrl) or miR-181a-5p overexpression (181a OE) viruses. U6 was used as the internal control. (g) Representative images of late-passage neurospheres infected with ctrl or 181a OE viruses (left) and quantification of neurosphere diameters (right). Scale bars, 100 μm. (h) Number of cells at 24 h, 48 h, and 72 h after late-passage NSCs were infected with ctrl or 181a OE viruses. (i) Representative images of Ki67 (green) and SOX2 (red) after late-passage NSCs were infected with ctrl or 181a OE viruses (left) and the proportion of $Ki67^+SOX2^+$ cells among all $SOX2^+$ cells (right). Scale bars, 100 μm. (j) Representative images of BrdU (green) and SOX2 (red) after late-passage NSCs were infected with ctrl or 181a OE viruses (left) and the proportion of $BrdU^+SOX2^+$ cells among all $SOX2^+$ cells (right). Scale bars, 100 μm. (k) qRT–PCR analysis the expression of miR-181a-5p in E13.5 NSCs and adult hippocampal NSCs. U6 was used as the internal control. (l) qRT–PCR analysis the expression of miR-181a-5p after adult hippocampal NSCs were transfected with control mimics (mc) or miR-181a-5p mimics (m181a). U6 was used as the internal control. (m) Representative images of adult hippocampal neurospheres transfected with mc or m181a (left) and quantification of neurosphere diameters (right). Scale bars, 100 μm. (n) Representative images of Ki67 (green) and SOX2 (red) after adult hippocampal NSCs were transfected with mc or m181a (left), and the proportion of $Ki67^+SOX2^+$ cells among all $SOX2^+$ cells (right). Scale bars, 100 μm. (o) Representative images of BrdU (green) and SOX2 (red) after adult hippocampal NSCs were transfected with mc or m181a (left), and the proportion of $BrdU^+SOX2^+$ cells among all $SOX2^+$ cells (right). Scale bars, 100 μm. (a–e) were tested in early-passage NSCs; (f–j) were tested in late-passage NSCs; (l–o) were tested in adult hippocampal NSCs. Nuclei were stained with Hoechst 33342 (blue), and "merge" images indicate the merging of images acquired with distinct channels (green, red, and blue). $^*p<0.05$, $^{**}p<0.01$, $^{***}p<0.001$. Values are presented as mean ± SD. Student's t test was used in (a), (b), (d–g), and (i–o), while two-way ANOVA with Tukey's post hoc test for multiple comparisons was applied in (c) and (h). See also Figures S2 and S3.

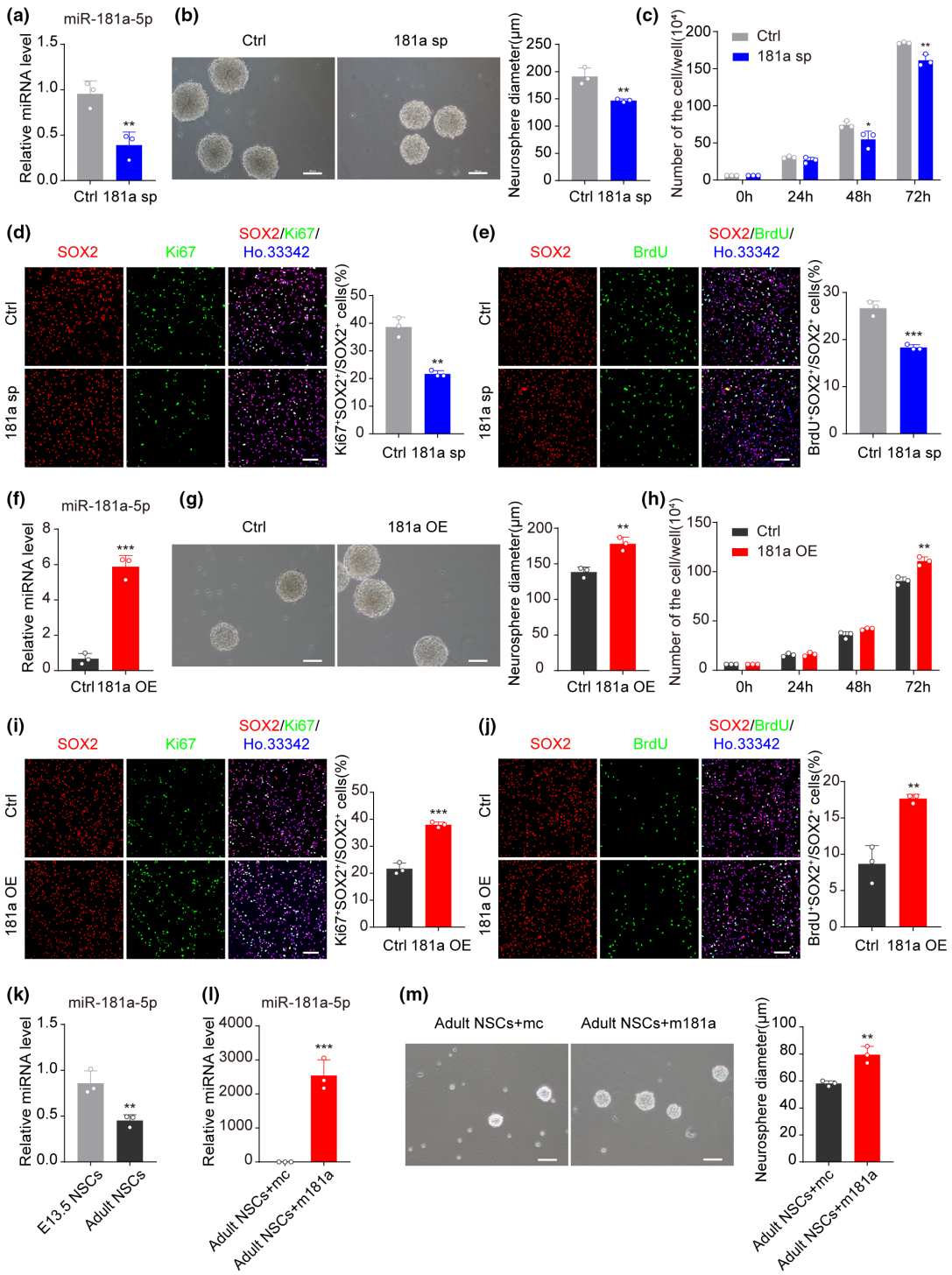
(a)
miR-181a-5p
Relative miRNA level
Ctrl 181a sp
(b)
Ctrl
181a sp
Neurosphere diameter(μm)
Ctrl 181a sp
(c)
Ctrl
181a sp
Number of the cell/well(10⁴)
0h 24h 48h 72h
(d)
SOX2
Ki67
SOX2/Ki67/ Ho.33342
Ctrl
181a sp
Ki67⁺SOX2⁺/SOX2⁺ cells(%)
Ctrl 181a sp
(e)
SOX2
BrdU
SOX2/BrdU/ Ho.33342
Ctrl
181a sp
BrdU⁺SOX2⁺/SOX2⁺ cells(%)
Ctrl 181a sp
(f)
miR-181a-5p
Relative miRNA level
Ctrl 181a OE
(g)
Ctrl
181a OE
Neurosphere diameter(μm)
Ctrl 181a OE
(h)
Ctrl
181a OE
Number of the cell/well(10⁴)
0h 24h 48h 72h
(i)
SOX2
Ki67
SOX2/Ki67/ Ho.33342
Ctrl
181a OE
Ki67⁺SOX2⁺/SOX2⁺ cells(%)
Ctrl 181a OE
(j)
SOX2
BrdU
SOX2/BrdU/ Ho.33342
Ctrl
181a OE
BrdU⁺SOX2⁺/SOX2⁺ cells(%)
Ctrl 181a OE
(k)
miR-181a-5p
Relative miRNA level
E13.5 NSCs
Adult NSCs
(l)
miR-181a-5p
Relative miRNA level
Adult NSCs+mc
Adult NSCs+m181a
(m)
Adult NSCs+mc
Adult NSCs+m181a
Neurosphere diameter(μm)
Adult NSCs+mc
Adult NSCs+m181a
(n)
SOX2
Ki67
SOX2/Ki67/ Ho.33342
Adult NSCs+mc
Adult NSCs+m181a
Ki67⁺SOX2⁺/SOX2⁺ cells(%)
Adult NSCs+mc
Adult NSCs+m181a
(o)
SOX2
BrdU
SOX2/BrdU/ Ho.33342
Adult NSCs+mc
Adult NSCs+m181a
BrdU⁺SOX2⁺/SOX2⁺ cells(%)
Adult NSCs+mc
Adult NSCs+m181a

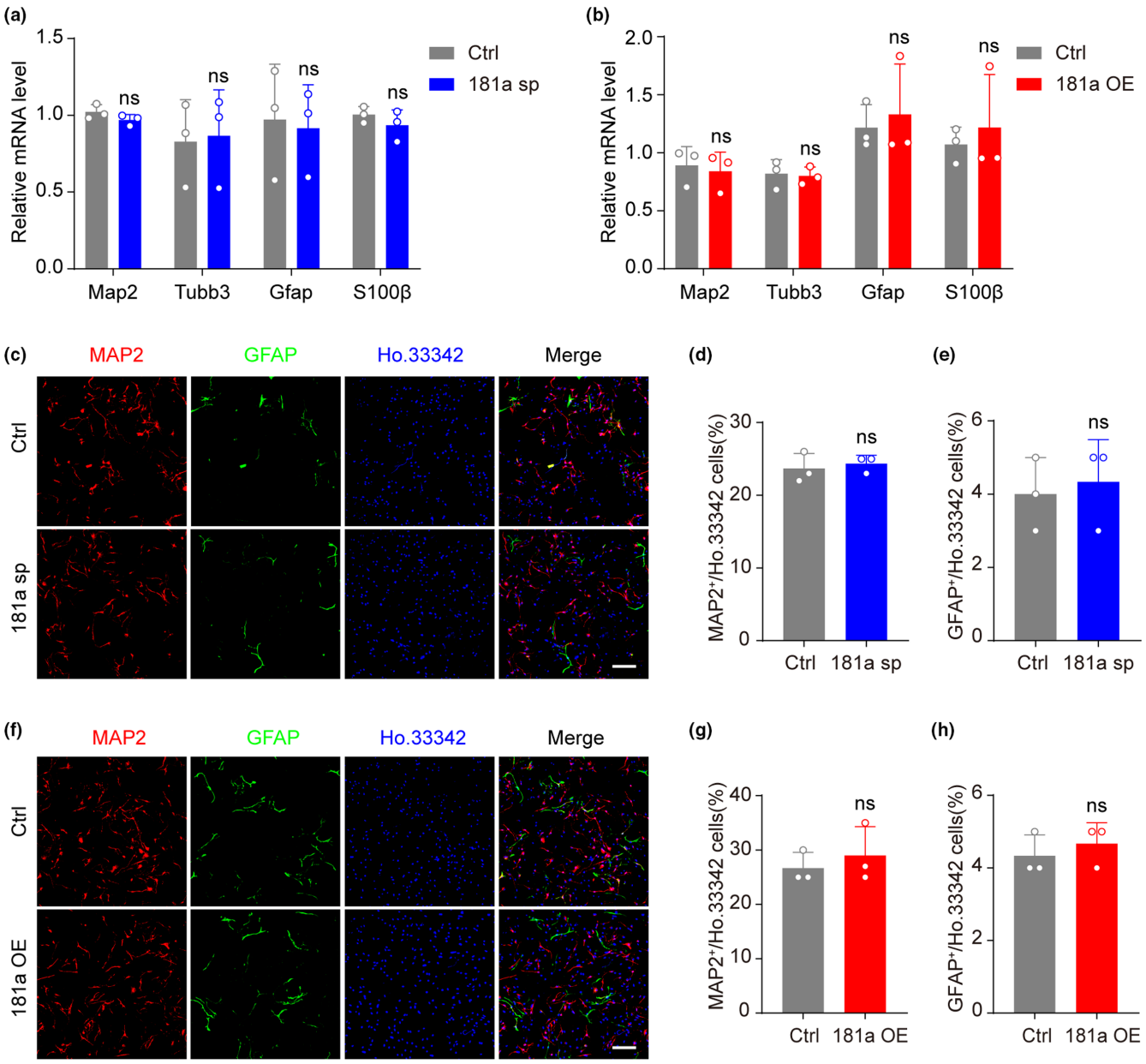

FIGURE 3 MiR-181a-5p does not affect NSC differentiation potential. (a) qRT–PCR analysis of the expression of neuron-related genes (Map2 and Tubb3) and astrocyte-related genes (Gfap and S100β) in NSCs infected with control (ctrl) or miR-181a-5p sponge (181a sp) viruses after differentiation. GAPDH was used as the internal control. (b) qRT–PCR analysis of the expression of neuron-related genes (Map2 and Tubb3) and astrocyte-related genes (Gfap and S100β) in NSCs infected with control (ctrl) or miR-181a-5p overexpression (181a OE) viruses after differentiation. GAPDH was used as the internal control. (c–e) Representative images of GFAP (green) and MAP2 (red) in NSCs infected with ctrl or 181a sp viruses after differentiation (c) and quantification of $MAP2^+$ cells (d) and $GFAP^+$ cells (e). Scale bars, 100 μm. (f–h) Representative images of GFAP (green) and MAP2 (red) in NSCs infected with ctrl or 181a OE viruses after differentiation (f) and quantification of $MAP2^+$ cells (g) and $GFAP^+$ cells (h). Scale bars, 100 μm. The 9th to 12th passages were used for experiments. ns: not significant. Values are presented as mean ± SD. Two-way ANOVA with Tukey's post hoc test for multiple comparisons was used in (a) and (b), while Student's t test was used in (d), (e), (g), and (h).

We found that PTEN, a negative regulator of AKT signaling, was the potential target of miR-181a-5p under this condition (Figure 4a). As there are three miR-181a-5p binding sites in the 3′UTR of PTEN (Figure 4b), to confirm the binding between miR-181a-5p and PTEN, we cloned the wild-type (WT) and mutated 3′UTR of PTEN into a pGL3 vector and performed a luciferase assay. The results showed that miR-181a-5p suppressed luciferase activity in the WT but not the mutated reporter. Furthermore, we found that site 1 and site 2 were important for miR-181a-5p binding, as miR-181a-5p could not suppress luciferase activity when site 1 and site 2 were mutated (Figure 4c), and the miR-181a-5p sponge or inhibitors could abolish the inhibitory effect of miR-181a-5p on luciferase activity, further confirmed the binding between miR-181a-5p and PTEN (Figure S4a,b). As the protein level of PTEN in the late-passage NSCs was higher than that in the early-passage NSCs (Figure 4d), we overexpressed miR-181a-5p in late-passage NSCs and found a

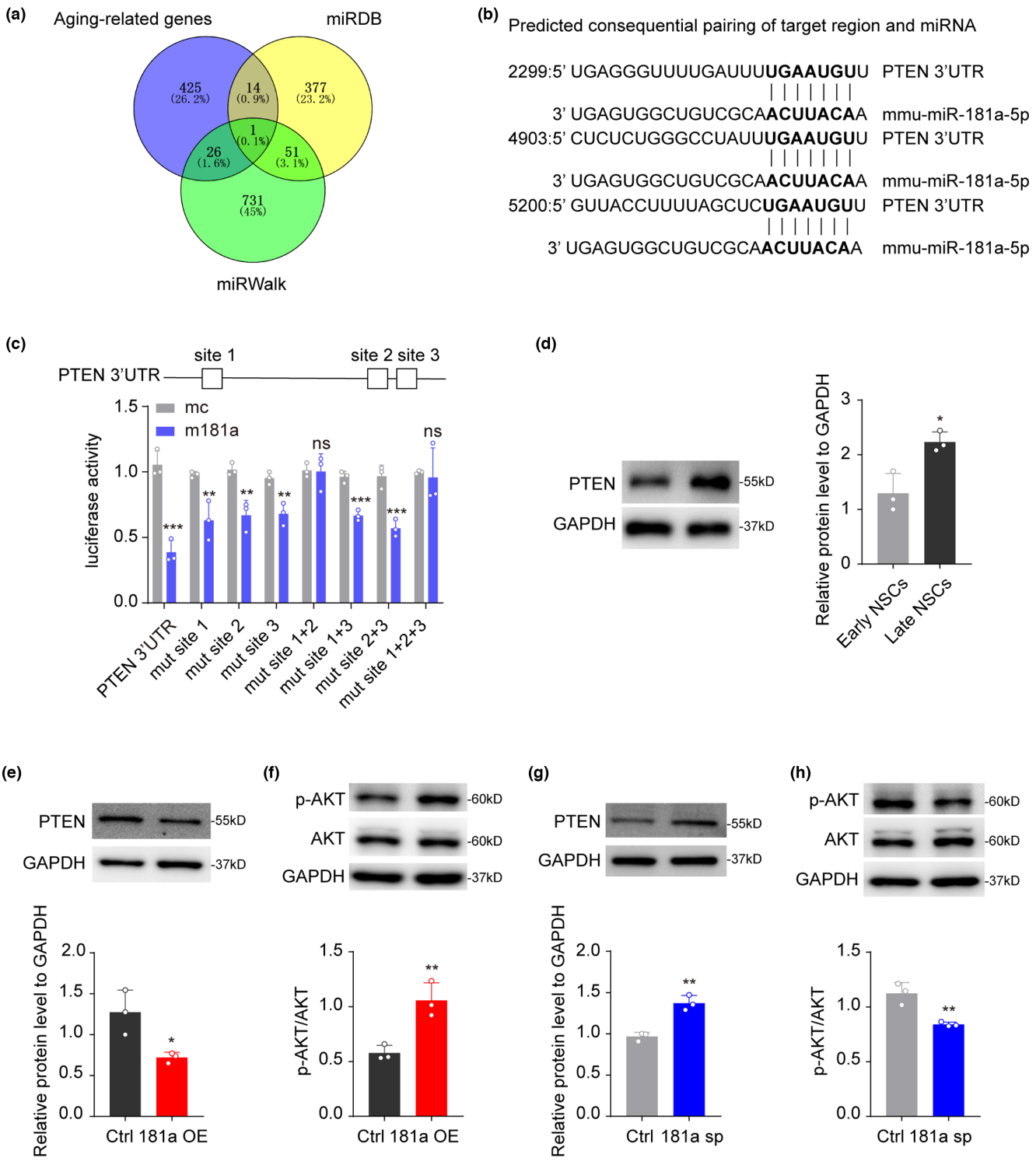

FIGURE 4 PTEN is a target of miR-181a-5p. (a) Venn diagrams showing the overlap of genes associated with aging and candidate miR-181a-5p target genes from miRDB and miRWalk. (b) The binding sequences of miR-181a-5p and the 3'UTR of Pten. (c) Luciferase reporter assays for miR-181a-5p and the full-length Pten 3'UTR with native or mutant binding sites. (d) Western blot analysis of PTEN expression in early-passage NSCs (early NSCs) and late-passage NSCs (late NSCs). (e,f) Western blot analysis of PTEN (e), phospho-AKT (p-AKT) and AKT (f) expression in late-passage NSCs infected with control (ctrl) or miR-181a-5p overexpression (181a OE) viruses. (g,h) Western blot analysis of PTEN (g), p-AKT and AKT (h) expression in early-passage NSCs infected with control (ctrl) or miR-181a-5p sponge (181a sp) viruses. (e,f) were tested in late-passage NSCs; (g,h) were tested in early-passage NSCs. $^{*}p<0.05$, $^{**}p<0.01$, $^{***}p<0.001$, ns: not significant. Values are presented as mean ± SD. Two-way ANOVA with Tukey's post hoc test for multiple comparisons was applied in (c), while Student's t test was used in (d–h). See also Figure S4.

corresponding reduction in the PTEN protein level and an increase in the phospho-AKT (p-AKT) level (Figure 4e,f). In contrast, inhibition of miR-181a-5p in early-passage NSCs upregulated the protein level of PTEN and downregulated the level of p-AKT (Figure 4g,h). These results confirmed that the PTEN-AKT pathway can be regulated by miR-181a-5p. Furthermore, we established PTEN knockdown and overexpression NSCs, respectively, and the expression of PTEN was validated by Western blotting (Figure S4c). Immunofluorescence staining analysis showed that knockdown of PTEN in late-passage NSCs increased the percentage of Ki67/Sox2 or BrdU/Sox2 double-positive cells (Figure S4d,e), while overexpression of PTEN in early-passage NSCs reduced the percentage of Ki67/Sox2 or BrdU/Sox2 double-positive cells (Figure S4f,g). Taken together, the above data show that PTEN suppresses NSC proliferation, which is contrary to the function of miR-181a-5p; thus, we speculated that PTEN may act as a target of miR-181a-5p in NSC proliferation.

To confirm this, PTEN was knocked down with shPTEN lentivirus in 181a sp NSCs (Figure 5a). The PTEN knockdown significantly rescued the inhibitory effect of 181a sp on the size of neurospheres, as well as the percentage of Ki67/Sox2 or BrdU/Sox2 double-positive cells (Figure 5b–f). Next, we overexpressed PTEN in 181a-overexpressing NSCs (Figure 5g) and found that the overexpression of PTEN in 181a OE NSCs also significantly reduced the influence of miR-181a-5p on the size of neurospheres as well as the percentage of Ki67/Sox2 or BrdU/Sox2 double-positive cells (Figure 5h–l). In conclusion, these studies revealed that PTEN is the functional target of miR-181a-5p in NSC proliferation.

2.4 | Inhibition of miR-181a-5p decreases the proliferation of NSCs and impairs the learning and memory abilities of young mice

We then explored whether miR-181a-5p is required for the proliferation of NSCs and the learning and memory abilities of young mice. rAAVs containing Nestin promoter-driven miR-181a-5p sponge and GFP (Nes-181a sp) were injected into the hippocampi of young mice (Figure S5a). GFP^+ NSCs in the dentate gyrus of young mice were isolated by FACS, and the expression level of the miR-181a-5p sponge was measured by qRT–PCR (Figure S5b). The number of GFP^+Ki67^+, GFP^+BrdU^+ NSCs, and $BrdU^+DCX^+$ newborn neurons was decreased in the dentate gyrus of young mice in Nes-181a sp group (Figure S5c–f), while the percentage of $BrdU^+DCX^+$ in total $BrdU^+$ cells was not altered (Figure S5g). These data indicate that inhibition of miR-181a-5p decreases NSC proliferation but does not affect neuronal differentiation. In addition, in the NOR test, the discrimination index and the discrimination ratio of novel objects were lower in miR-181a-5p inhibition mice (Figure S5h–j), and in the MWM test, the miR-181a-5p inhibition mice located the hidden platform more slowly, crossed the platform fewer times, and spent less time in the goal quadrant than control mice (Figure S5k–p). These results suggest that miR-181a-5p is critical for the proliferation of NSCs and the learning and memory abilities of young mice.

2.5 | MiR-181a-5p promotes the proliferation of NSCs and ameliorates learning and memory deficits in aged mice

As we observed decreased expression of miR-181a-5p (Figure 1e), increased PTEN protein levels and decreased p-AKT levels in the hippocampi of aged mice (Figure S6a), we further investigated whether miR-181a-5p regulated the proliferation of hippocampal NSCs in aged mice. For this purpose, adeno-associated viruses (AAVs) overexpressing miR-181a-5p were injected into the hippocampi of 14-month-old mice (Figure 6a and S6b). The expression of miR-181a-5p increased in the hippocampus after 2 weeks of injection (Figure 6b). Western blotting showed decreased PTEN protein levels and increased p-AKT levels in the miR-181a-5p overexpression group (Figure 6c). The mRNA level of Ki67 and the number

FIGURE 5 PTEN rescues NSC proliferation deficits induced by miR-181a-5p. (a) Western blot analysis of PTEN expression in early-passage NSCs infected with control (ctrl), miR-181a-5p sponge (181a sp) only or miR-181a-5p sponge together with shPTENs (181a sp + shPTEN-1; 181a sp + shPTEN-2) viruses. (b) Representative images of early-passage neurospheres infected with ctrl, 181a sp only or 181a sp together with shPTENs viruses (left), and quantification of neurosphere diameters (right). Scale bars, 100 μm. (c,d) Representative images of Ki67 (green) and SOX2 (red) after early-passage NSCs were infected with ctrl, 181a sp only or 181a sp together with shPTENs viruses (c) and the proportion of $Ki67^+SOX2^+$ cells among all $SOX2^+$ cells (d). Scale bars, 100 μm. (e and f) Representative images of BrdU (green) and SOX2 (red) after early-passage NSCs were infected with ctrl, 181a sp only or 181a sp together with shPTENs viruses (e) and the proportion of $BrdU^+SOX2^+$ cells among all $SOX2^+$ cells (f). Scale bars, 100 μm. (g) Western blot analysis of PTEN expression in late-passage NSCs infected with control (ctrl), miR-181a-5p overexpression (181a OE) only or miR-181a-5p together with PTEN overexpression (181a OE + PTEN OE) viruses. (h) Representative images of late-passage neurospheres infected with ctrl, 181a OE only or 181a OE together with PTEN OE viruses (left) and quantification of neurosphere diameters (right). Scale bars, 100 μm. (i,j) Representative images of Ki67 (green) and SOX2 (red) after late-passage NSCs were infected with ctrl, 181a OE only or 181a OE together with PTEN OE viruses (i), and the proportion of $Ki67^+SOX2^+$ cells among all $SOX2^+$ cells (j). Scale bars, 100 μm. (k,l) Representative images of BrdU (green) and SOX2 (red) after late-passage NSCs were infected with ctrl, 181a OE only or 181a OE together with PTEN OE viruses (k), and the proportion of $BrdU^+SOX2^+$ cells among all $SOX2^+$ cells (l). Scale bars, 100 μm. (a–f) were tested in early-passage NSCs; (g–l) were tested in late-passage NSCs. Nuclei were stained with Hoechst 33342 (blue), and "merge" images indicate the merging of images acquired with distinct channels (green, red and blue). $^*p < 0.05$, $^{**}p < 0.01$, $^{***}p < 0.001$ versus ctrl (b, d, f, h, j and l); $^{\#}p < 0.05$, $^{\#\#}p < 0.01$, $^{\#\#\#}p < 0.001$ versus 181a sp (b, d and f), or versus 181a OE (h, j and l). Values are presented as mean ± SD. One-way ANOVA with Tukey's post hoc test for multiple comparisons was applied in (b), (d), (f), (h), (j), and (l).

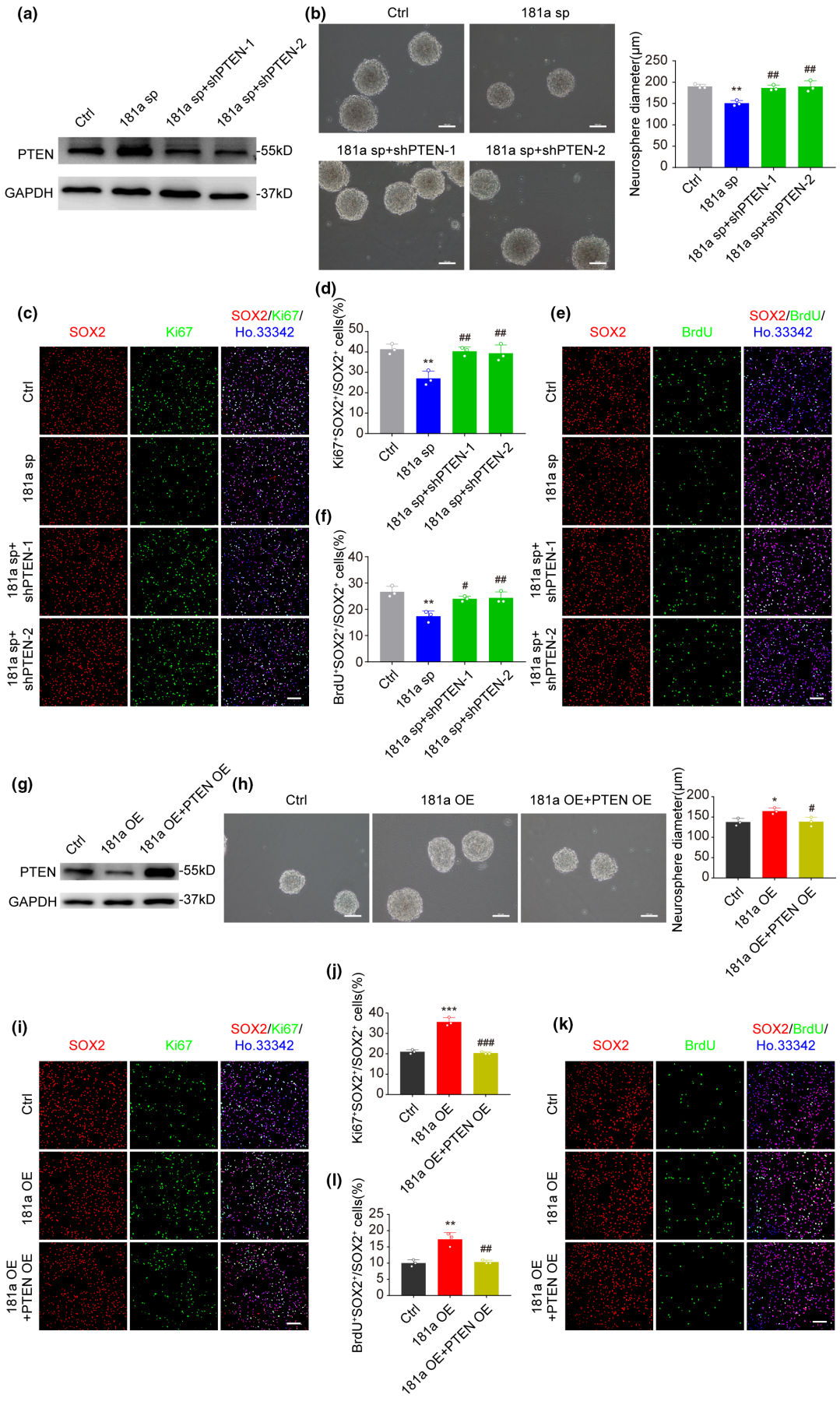
(a)
Ctrl
181a sp
181a sp+shPTEN-1
181a sp+shPTEN-2
PTEN
-55kD
GAPDH
-37kD
(b)
Ctrl
181a sp
181a sp+shPTEN-1
181a sp+shPTEN-2
Neurosphere diameter(μm)
(c)
SOX2
Ki67
SOX2/Ki67/ Ho.33342
(d)
Ki67+SOX2+/SOX2+ cells(%)
(e)
SOX2
BrdU
SOX2/BrdU/ Ho.33342
(f)
BrdU+SOX2+/SOX2+ cells(%)
(g)
Ctrl
181a OE
181a OE+PTEN OE
PTEN
-55kD
GAPDH
-37kD
(h)
Ctrl
181a OE
181a OE+PTEN OE
Neurosphere diameter(μm)
(i)
SOX2
Ki67
SOX2/Ki67/ Ho.33342
(j)
Ki67+SOX2+/SOX2+ cells(%)
(k)
SOX2
BrdU
SOX2/BrdU/ Ho.33342
(l)
BrdU+SOX2+/SOX2+ cells(%)

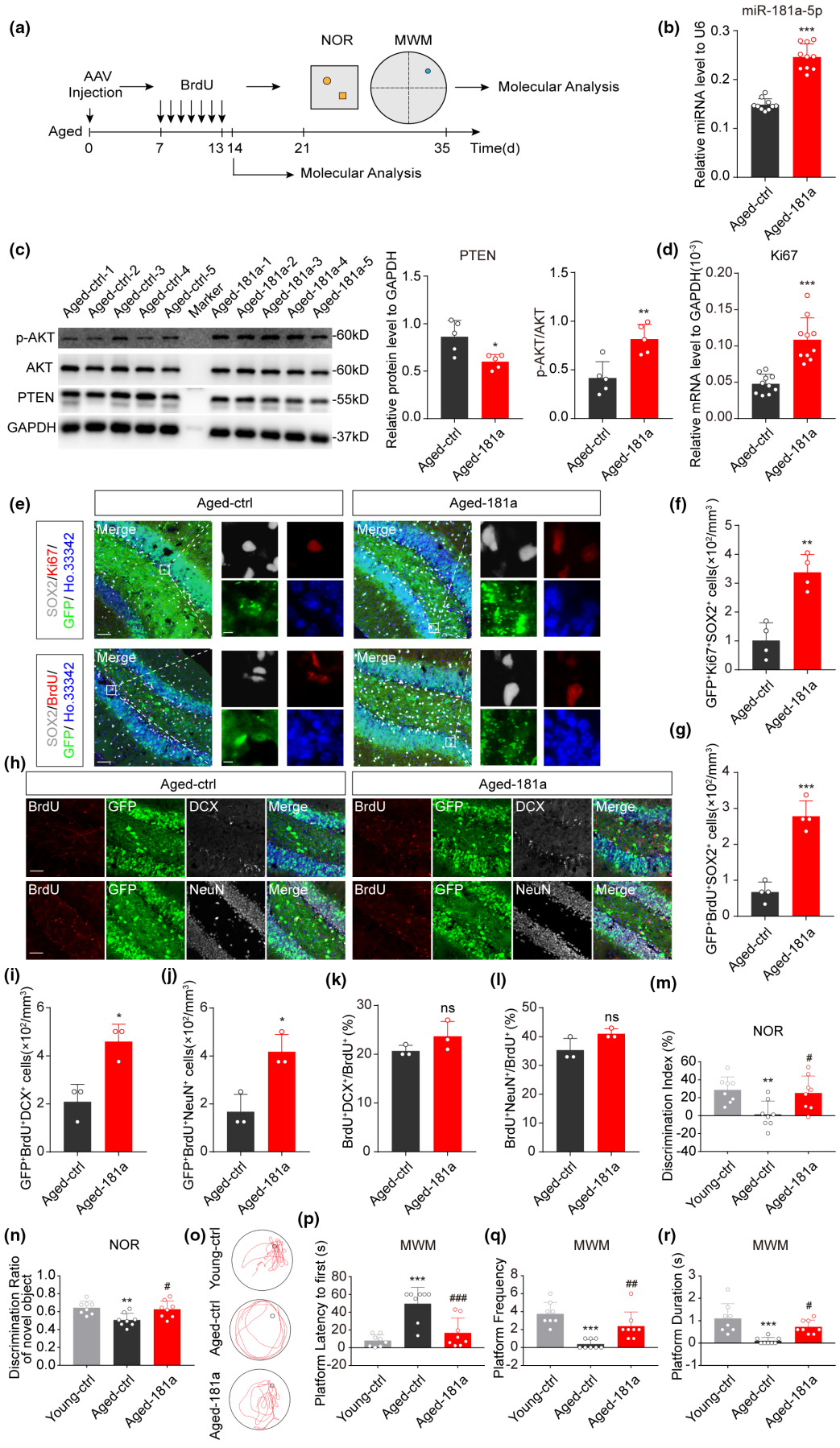
(a)
NOR
MWM
AAV Injection
BrdU
Molecular Analysis
Aged
0
7
13 14
21
35
Time(d)
Molecular Analysis
(b)
miR-181a-5p
Relative miRNA level to U6
Aged-ctrl
Aged-181a
(c)
Aged-ctrl-1
Aged-ctrl-2
Aged-ctrl-3
Aged-ctrl-4
Aged-ctrl-5
Marker
Aged-181a-1
Aged-181a-2
Aged-181a-3
Aged-181a-4
Aged-181a-5
p-AKT
AKT
PTEN
GAPDH
-60kD
-60kD
-55kD
-37kD
PTEN
Relative protein level to GAPDH
p-AKT/AKT
(d)
Ki67
Relative mRNA level to GAPDH(10⁻³)
(e)
Aged-ctrl
Aged-181a
SOX2/Ki67/ GFP/ Ho.33342
SOX2/BrdU/ GFP/ Ho.33342
Merge
(f)
GFP⁺Ki67⁺SOX2⁺ cells(×10²/mm³)
(g)
GFP⁺BrdU⁺SOX2⁺ cells(×10²/mm³)
(h)
Aged-ctrl
Aged-181a
BrdU
GFP
DCX
NeuN
Merge
(i)
GFP⁺BrdU⁺DCX⁺ cells(×10²/mm³)
(j)
GFP⁺BrdU⁺NeuN⁺ cells(×10²/mm³)
(k)
BrdU⁺DCX⁺/BrdU⁺ (%)
ns
(l)
BrdU⁺NeuN⁺/BrdU⁺ (%)
ns
(m)
NOR
Discrimination Index (%)
Young-ctrl
Aged-ctrl
Aged-181a
(n)
NOR
Discrimination Ratio of novel object
(o)
Young-ctrl
Aged-ctrl
Aged-181a
(p)
MWM
Platform Latency to first (s)
(q)
MWM
Platform Frequency
(r)
MWM
Platform Duration (s)

FIGURE 6 MiR-181a-5p promotes NSC proliferation in the hippocampus and ameliorates learning and memory deficits in aged mice. (a) Schematic diagram of the experimental design. (b) qRT–PCR analysis of the expression of miR-181a-5p in the hippocampi of aged-ctrl and aged-181a mice after intrahippocampal injection. U6 was used as the internal control ($n = 10$ per group). (c) Western blot analysis of PTEN, phospho-AKT (p-AKT), and AKT expression in the hippocampi of aged-ctrl and aged-181a mice. Shown are sample Western blot images and quantifications ($n = 5$ per group). (d) qRT–PCR analysis of the expression of Ki67 in the hippocampi of aged-ctrl and aged-181a mice. GAPDH was used as the internal control ($n = 10$ per group). (e–g) Representative images of GFP (green), Ki67 (red), BrdU (red), SOX2 (white), and Ho.33342 (blue) in the DG of aged-ctrl and aged-181a mice (e) and quantification of the number of $GFP^+Ki67^+SOX2^+Ho.33342^+$ cells (f) and $GFP^+BrdU^+SOX2^+Ho.33342^+$ cells (g) in the DG. Scale bars, 50 μm (left) and 5 μm (right) ($n = 4$ per group). (h) Representative images of GFP (green), BrdU (red), DCX (white), NeuN (white), and Ho.33342 (blue) in the DG of aged-ctrl and aged-181a mice. Scale bars, 50 μm. (i–l) Quantification of the number of $BrdU^+DCX^+$ (i) and $BrdU^+NeuN^+$ cells (j) in the DG and the proportion of $BrdU^+DCX^+$ (k) and $BrdU^+NeuN^+$ cells (l) among all $BrdU^+$ cells ($n = 3$ per group). (m,n) Analysis of the NOR test. Discrimination index (m) and discrimination ratio of novel objects (n) ($n = 8$ per group). (o–r) Analysis of the MWM test. Representative traces were recorded with a video-tracking system (o). Latencies to first reach the platform region (p), frequencies of crossing (q), and duration in the goal quadrant (r) were analyzed ($n = 8$ per group). $^*p < 0.05$, $^{**}p < 0.01$, $^{***}p < 0.001$ versus aged-ctrl (b, c, d, f, g, and i–l), or versus young-ctrl (m, n, and p–r); $^{\#}p < 0.05$, $^{\#\#}p < 0.01$ versus aged-ctrl (m, n and p–r); ns: not significant. Values are presented as mean ± SD. Student's t test was used in (b–d), (f), (g), and (i–l), while one-way ANOVA with Tukey's post hoc test for multiple comparisons was applied in (m), (n), and (p–r). AAV, adeno-associated virus; DG, dentate gyrus; MWM, Morris water maze; NOR, novel object recognition. See also Figures S5, S6 and S7.

of $Ki67^+Sox2^+GFP^+$ or $BrdU^+Sox2^+GFP^+$ NSCs were significantly higher in the dentate gyrus of aged mice overexpressing miR-181a-5p (Figure 6d–g), while the volume of the hippocampus was unchanged (Figure S3c), suggesting that miR-181a-5p can promote the proliferation of NSCs in aged mice by repressing PTEN signaling. Further, we found that the numbers of $GFP^+BrdU^+DCX^+$ and $GFP^+BrdU^+NeuN^+$ cells increased in the miR-181a-5p overexpression group (Figure 6h–j). However, the percentages of $BrdU^+DCX^+$ and $BrdU^+NeuN^+$ in total $BrdU^+$ cells were not altered (Figure 6k,l), suggesting that overexpression of miR-181a-5p did not affect neuronal differentiation. Together, these results show that miR-181a-5p can increase the number of newborn neurons by increasing the number of NSCs but not directly promoting neuronal differentiation.

Furthermore, we performed behavior tests to assess the contribution of miR-181a-5p to the learning and memory abilities of aged mice. In the NOR test, the discrimination index and the discrimination ratio of novel objects were higher in miR-181a-5p-overexpressing mice than those of aged-control mice (Figure 6m,n and S6d), and in the MWM test, the miR-181a-5p overexpression mice located the hidden platform more quickly, crossed the platform more times, and spent more time in the goal quadrant than aged-control mice (Figure 6o–r, Figure S6e,f). These results indicate that miR-181a-5p can ameliorate learning and memory deficits of aged mice.

In order to further confirm the specific regulatory role of miR-181a-5p in NSCs, the rAAVs containing Nestin promoter-driven miR-181a-5p and GFP, which specifically infect NSCs, were injected into the dentate gyrus of aged mice (Figure S6g). GFP^+ NSCs in the dentate gyrus of aged mice were isolated by FACS, and the overexpression efficiency of miR-181a-5p in GFP^+ NSCs was validated by qRT–PCR (Figure S6h). Furthermore, the numbers of GFP^+Ki67^+ NSCs, GFP^+BrdU^+ NSCs, and $BrdU^+DCX^+$ newborn neurons was increased in the dentate gyrus of aged mice overexpressing miR-181a-5p (Figure S6i–l), but the percentage of $BrdU^+DCX^+$ in total $BrdU^+$ cells was unchanged (Figure S6m), indicating that miR-181a-5p can increase the number of NSCs but does not affect neuronal differentiation. In addition, consistent with the learning and memory improvements observed earlier, the discrimination index and the discrimination ratio of novel objects were higher in Nestin-miR-181a-5p-overexpressing mice than in control mice in the NOR test (Figure S6n–p), and the Nestin-miR-181a-5p overexpression mice located the hidden platform more quickly, crossed the platform more times, and spent more time in the goal quadrant than control mice in the MWM test (Figure S6q–v). As a recent study showed that AAV may ablate hippocampal neurogenesis (Johnston et al., 2021), a virus-free miRNA agomir was injected into the hippocampi of aged mice to overexpress miR-181a-5p (Figure S7a). Similar phenotypes were observed with previous ones with regard to NSCs proliferation and learning and memory abilities (Figure S7b–p). Thus, miR-181a-5p can ameliorate learning and memory deficits in aged mice by promoting NSC proliferation. To further examine the effect of miR-181a-5p on neurons, we also injected rAAVs containing Synapsin promoter-GFP (Syn-GFP) to specifically infect neurons in the dentate gyrus of aged mice. Behavioural results showed no significant difference between the syn-ctrl and syn-181a group mice by the NOR test and MWM test, indicating that overexpression of miR-181a-5p in neurons did not affect the learning and memory ability of aged mice (Figure S7q–z).

3 | DISCUSSION

Neurogenesis in the hippocampus persists throughout life but undergoes an age-related decline (Kuhn et al., 1996). Neurogenesis is one of the major factors affecting aging-related cognitive abilities, and promoting NSC neurogenesis has been considered as a potential strategy for the treatment of age-related cognitive decline (Berdugo-Vega et al., 2020; Drapeau & Abrous, 2008; Sasaki et al., 2021). However, prematurely promoting neurogenesis may cause NSCs to precociously differentiate into neurons and become depleted, which may diminish neurogenesis over time (Zhang et al., 2019; Zhou et al., 2018). A previous study found that deleting milk fat globule-epidermal growth factor (EGF) 8 (Mfge8) in early postnatal NSCs

could lead to premature NSC activation and reduce the adult NSC pool, which in turn led to a reduced number of proliferating NSCs and a decreased level of adult dentate neurogenesis (Zhou et al., 2018), indicating that maintenance of NSC proliferation without diminishing neurogenesis may be an effective means to expand NSC pool. Our present study showed that miR-181a-5p could promote the proliferation of NSCs and that overexpression of miR-181a-5p in the hippocampal NSCs could ameliorate learning and memory impairments in aged mice, suggesting that miR-181a-5p has potential applications for treating learning disabilities in elderly individuals.

NSCs have the capacity to self-renew and are multipotent. In some cases, promoting NSC proliferation may decrease the differentiation potential and vice versa. For example, overexpression of miR-219 promotes NSC differentiation into neurons but reduces NSC proliferation substantially (Murai et al., 2016). In contrast, overexpression of miR-184 or miR-195 enhanced NSC proliferation but repressed differentiation by targeting Numblike (Numbl) and MBD1, respectively (Liu et al., 2010, 2013). Previous studies showed that inactivation of Numbl in the cortex impaired neuronal differentiation (Li et al., 2003), and absence of MBD1 caused deficits in adult neurogenesis and hippocampal function (Zhao et al., 2003), which may be the reason why these miRNAs repress neuronal differentiation. In this study, we found that miR-181a-5p targets PTEN to promote the proliferation of NSCs but miR-181a-5p did not affect their differentiation into neurons and astrocytes, implying that miR-181a-5p serves as an important modulator of NSC proliferation in the hippocampus.

Pten is a well-known tumor suppressor gene, and recent studies have shown that Pten also has important roles in brain development. Conditional deletion of PTEN in embryonic CNS stem/progenitor cells significantly increased cell proliferation, decreased cell death, and enlarged cell size without disturbing neuronal differentiation potential (Groszer et al., 2001). In adult neural stem cells, conditional deletion of PTEN enhanced self-renewal, resulting in increased olfactory bulb mass and enhanced olfactory function (Gregorian et al., 2009). Direct deletion of PTEN may cause progressive enlargement and an enlarged, histoarchitecturally abnormal brain (Groszer et al., 2001). Coincidentally, a recent study found markedly increased expression of PTEN in a family with hereditary primary microcephaly; mild PTEN overexpression in brain organoids led to reduced neural precursor proliferation and the formation of significantly smaller brain organoids with microcephaly like phenotypes (Dhaliwal et al., 2021; Oliveira et al., 2019). These studies indicate that PTEN is a dosage-sensitive gene in the regulation of brain development. In our study, we found that inhibiting PTEN increased the proliferation of NSCs and that overexpressing miR-181a-5p promoted the proliferation of NSCs in the aged hippocampus by reducing the protein level of PTEN but did not increase the volume of the hippocampus (Figure S6c), showing the potential value of miR-181a-5p and PTEN in the treatment of NSC proliferation defects.

Previous studies have shown that reduced miR-181a-5p expression is associated with a series of age-related disorders, including immune dysfunction (Kim et al., 2019; Lu, Li, et al., 2021), sarcopenia (Soriano-Arroquia et al., 2016), and hearing loss (Zhang et al., 2013). For example, miR-181a-5p was downregulated in aged NK cells, which inhibited NK cell development by reducing the production of IFN-γ and the cytotoxicity of NK cells (Lu, Li, et al., 2021). MiR-181a was also downregulated in sarcopenia, an age-related loss of skeletal muscle mass and function, and negatively regulated myotube size (Soriano-Arroquia et al., 2016). Moreover, miR-181a was also decreased in the brain of Alzheimer's disease mice (Wu et al., 2019), implying that miR-181a plays an important, yet undiscovered role in age-related disorders. Here, we found that the expression level of miR-181a-5p was decreased in the hippocampi of aged mice and that overexpression of miR-181a-5p contributed to the proliferation of NSCs by targeting PTEN, both in vitro and in vivo. These findings first confirmed the crucial role of miR-181a-5p in NSC proliferation and differentiation, and further verified the importance of miR-181a-5p in the process of aging.

Collectively, our findings demonstrated the roles of miR-181a-5p in NSC proliferation. Considering the high drug potential of miRNAs, miR-181a-5p may provide the basis for the development of drugs to treat the aging-related neurological disorders.

4 | MATERIALS AND METHODS

4.1 | Mice

C57BL/6J mice were purchased from the B&K Universal Group Limited and housed in standard, pathogen-free conditions at the Laboratory Animal Research Center of Tongji University. All procedures involving animals were approved by the Institutional Animal Care and Use Committee of Tongji University in accordance with the Guide for the Care and Use of Laboratory Animals (NIH). Young mice (male, 12–14 weeks old) and aged mice (male, 14–16 months old) were used for experiments.

4.2 | Behavioral tests

Novel object recognition (NOR) test and Morris water maze (MWM) test were used to evaluate the learning and memory abilities. See the Supplementary methods and materials for details.

4.3 | 5-bromo-2′-deoxyuridine (BrdU) injections

Mice were given a daily single intraperitoneal injection of BrdU (50 mg/kg of body weight) for 7 or 10 consecutive days. For NSC proliferation studies, brains were perfused 24 h after the last BrdU injection. For differentiation studies, brains were perfused 3 weeks after the last BrdU injection.

4.4 | Virus

For adeno-associated virus serotype 2 preparation (AAV2), AAV control or AAV miR-181a-5p OE plasmids, pAAV-RC and pHelper (ratio

of vectors at 1:1:1) were cotransfected into 293A cells. All the cells were harvested and resuspended in 2.5 mL of serum-free DMEM after transfection for 72 h. Then, the cells were treated with 4 freeze/thaw cycles in a liquid nitrogen bath and 37°C water bath. The viral supernatant was collected after centrifugation at 10,000*g* for 10 min. The virus was purified by a ViraBind™ AAV Purification Kit according to the manufacturer's protocol. Viral titers were 10^9 v.g./ml. The recombinant adeno-associated virus serotype 2/9 (rAAV2/9) contained Nestin promoter and Synapsin promoter were provided by OBiO Company (https://www.obiosh.com/). Viral titers were 10^{10} v.g./ml.

4.5 | Stereotactic injections

C57BL/6J mice were anesthetized by intraperitoneal injection of AVER and fixed in a stereotaxic frame. Then, the coordinates relative to the bregma were located as X = ±1.75 mm, Y = -1.75 mm, and Z = -2.06 mm by using an ultra-precise stereotactic injector. The AAV (2 μL) was injected into the DG by a Hamilton syringe at a rate of 0.2 μL/min. 10 min after injection, the syringe was slowly pulled out to reduce the loss of virus. After injection of the bilateral DG, the skin was closed by medical suture, and then, the animal was placed on a heating pad until it regained consciousness. Proliferation-related studies were performed 2 weeks post stereotaxic injections, behavioral tests were performed 3 weeks post stereotaxic injections, and neurogenesis-related studies were performed 5 weeks post stereotaxic injections.

4.6 | In situ hybridization

Fixed Frozen brains of 12-week-old mice were cut into 10 μm thickness and examined using the miRNAscope technique according to the manufacturer's protocol (Advanced Cell Diagnostics, https://acdbio.com/).

4.7 | Fluorescence-activated cell sorting (FACS)

The hippocampi were isolated after Nestin-GFP or Synapsin-GFP rAAVs injected and dissociated with the Neural Tissue Dissociation Kit P (Miltenyi Biotec). GFP^+ cells were sorted directly into RNAiso (Takara). Flow cytometry was performed on a BD FACS AriaII instrument. The data were analyzed using FlowJo software.

4.8 | Cell culture and differentiation

Embryonic NSCs were isolated from the forebrain of E13.5 C57BL/6J mouse embryos as previously described (Ahlenius & Kokaia, 2010). Adult hippocampal NSCs were isolated from the male C57BL/6J mice at 8-week-old with the Neural Tissue Dissociation Kit P according to the manufacturer's protocol (Miltenyi Biotec). NSCs were cultured as neurospheres in growth medium composed of DMEM/F12 (Gibco), 2% B27 without vitamin A (Invitrogen), 1% GlutaMAX (Invitrogen), 1% NEAA (Invitrogen), 1% sodium pyruvate (Invitrogen), 20 ng/mL EGF (Sino Biological), and 20 ng/mL FGF-2 (Sino Biological).

NSCs were passaged every 4 days. Early-passage NSCs refer to passages 5–8, and late-passage NSCs refer to passages 19–22. To assess neurosphere diameter, NSCs were seeded in ultralow-adhesion 6 cm dishes at a density of 6×10^5 cells per dish. The neurospheres were captured on the fourth day, and their diameters were quantified with ImageJ software. To assess cell proliferation, NSCs were dissociated into single cells with Accutase (Gibco) and seeded in coverslips pretreated with polyornithine (Gibco) and lamimin (Sigma); BrdU was added for the last 2 h prior to cell fixation. To assess differentiation, NSCs were dissociated into single cells and seeded on coverslips or 6-well plates (Corning) pretreated with polyornithine and laminin. The next day, EGF and FGF-2 were removed. After 48 h, follow-up experiments were conducted to evaluate differentiation into neurons and astrocytes.

4.9 | Vector

For the miR-181a-5p sponge vector, 9 copies of the miR-181a-5p sponge sequence and WPRE were cloned into the Fuw vector (Addgene). For the shPTEN vector, short hairpin RNAs (shRNAs) targeting PTEN were cloned into the pLKO.1 vector (Addgene). For the luciferase reporter vector, full-length Pten 3'UTR or 3'UTR with 1–3 mutant miR-181a-5p binding sites were cloned into the pGL3 vector (Addgene). Mutant vectors changed the miR-181a-5p target site in the PTEN 3'UTR from 5′-TGAATGT- 3′ to 5'-ACATTCA-3′. For the AAV miR-181a-5p OE vector, the miR-181a-5p sequence, WPRE, ubiquitin promoter sequence, and a GFP fluorescent reporter were cloned into the AAV vector (VPK-410, Cell Biolabs). All vectors were verified by DNA sequencing. Detailed primer sequences are listed in Table S1.

4.10 | Lentiviral packaging, concentration, and infection

The lentiviral plasmids with Pax2 and VSVG (ratio of plasmids at 4:3:2) were cotransfected into 293FT cells. The medium containing the virus was filtered with a 0.45 μm filter and purified with Lenti-concentin (5×) (Excell Bio) according to the manufacturer's protocol to remove the effect of serum on NSCs.

4.11 | NSC proliferation curve

The neurospheres were dissociated and aliquoted into 24-well plates pretreated with polyornithine and lamimin at a density of 6×10^4 cells per well. The NSCs were infected with different viruses and counted by a cytometer (CountStar) at 24 h, 48 h, 72 h.

4.12 | Dual-luciferase reporter assay

Control Renilla luciferase plasmids, pGL3-luciferase reporter plasmids, control, or miR-181a-5p mimics were cotransfected into NIH3T3 cells. Luciferase activity was measured by the Dual-luciferase reporter assay system (Promega) after transfection for 48 h.

4.13 | Quantitative RT–PCR

Brain tissues and cultured cells were lysed by RNAiso (Takara), total RNA was extracted by chloroform and isopropanol, and the quality of RNA was measured by the 260/280 ratio. Five hundred nanograms of total RNA was used to synthesize cDNA with the PrimeScript™ RT reagent Kit (Takara). qRT–PCR was performed using SYBR Green qRT–PCR Master Mix (Bio–Rad) on an Mx3000 instrument (Agilent). Relative expression levels were calculated by the $2^{-\Delta\Delta Ct}$ method with GAPDH expression as an internal control. MiRNA expression levels were measured using the Bulge-Loop™ miRNA qRT–PCR Primer Set (RiboBio) according to the manufacturer's instructions. Relative expression levels were calculated with U6 expression as an internal control. Detailed primer sequences are listed in Table S1.

4.14 | Western blotting

For the cultured cells, the same number of cells was collected and lysed in sodium dodecyl sulfate (SDS, Amersham) buffer with 1× protease inhibitor (PI, Roche). For brain tissues, the tissues were lysed with RIPA for 30 min on ice. The protein concentrations were calculated using a bicinchoninic acid assay (BCA). Equal amounts of proteins were separated by SDS–PAGE and transferred onto PVDF membranes. The membranes were blocked with 3% BSA at room temperature for 1 h and then incubated with primary antibodies diluted in TBST overnight at 4°C and the corresponding secondary antibodies for 1 h at room temperature. Blots were visualized by enhanced chemiluminescence (ECL). GAPDH was used as an internal control. ImageJ was used for Western blot grayscale analysis. The antibodies are listed in Table S2.

4.15 | Statistical analysis

The data are presented as the means ± SD from three independent biological replicates. Student's *t* tests were used for two-group comparisons; one-way ANOVA and two-way ANOVA followed by Tukey's post hoc test were used for multiple comparisons. $p < 0.05$ was considered statistically significant. $^{*,\#}p < 0.05$; $^{**,\#\#}p < 0.01$; $^{***,\#\#\#}p < 0.001$. ns: not significant.

AUTHOR CONTRIBUTIONS

Q.Y.S., J.J.X, and J.H.K conceptualized and designed the project. Q.Y.S. performed the experiments, collected data, analyzed data, and prepared figures. L.M., Y.X.W., A.L.T, and Z.H.Y assisted in animal experiments. J.Q., X.W., and J.G.L. assisted in molecular biology experiments. Q.Y.S., J.J.X, J.H.K, and Y.K.W wrote the manuscript. J.H.K involved in funding acquisition and project administration, provided the resources, and supervised the study.

ACKNOWLEDGMENTS

This work was supported by the National Key R&D Program of China (2021YFA1100400, 2020YFA0113101), the National Natural Science Foundation of China (82230054, 31721003, 32270591, 32070617).

CONFLICT OF INTEREST STATEMENT

The authors declare that they have no conflict of interest.

DATA AVAILABILITY STATEMENT

This manuscript does not include large datasets.

ORCID

Jiuhong Kang https://orcid.org/0000-0001-7538-1889

REFERENCES

Aging Atlas, C. (2021). Aging Atlas: A multi-omics database for aging biology. *Nucleic Acids Research*, *49*(D1), D825–D830. https://doi.org/10.1093/nar/gkaa894

Ahlenius, H., & Kokaia, Z. (2010). Isolation and generation of neurosphere cultures from embryonic and adult mouse brain. *Methods in Molecular Biology*, *633*, 241–252. https://doi.org/10.1007/978-1-59745-019-5_18

Ahmad, S. T., Rogers, A. D., Chen, M. J., Dixit, R., Adnani, L., Frankiw, L. S., Lawn, S. O., Blough, M. D., Alshehri, M., Wu, W., Marra, M. A., Robbins, S. M., Cairncross, J. G., Schuurmans, C., & Chan, J. A. (2019). Capicua regulates neural stem cell proliferation and lineage specification through control of Ets factors. *Nature Communications*, *10*(1), 1–17. https://doi.org/10.1038/s41467-019-09949-6

Ben Abdallah, N. M. B., Slomianka, L., Vyssotski, A. L., & Lipp, H. P. (2010). Early age-related changes in adult hippocampal neurogenesis in C57 mice. *Neurobiology of Aging*, *31*(1), 151–161. https://doi.org/10.1016/j.neurobiolaging.2008.03.002

Berdugo-Vega, G., Arias-Gil, G., López-Fernández, A., Artegiani, B., Wasielewska, J. M., Lee, C. C., Lippert, M. T., Kempermann, G., Takagaki, K., & Calegari, F. (2020). Increasing neurogenesis refines hippocampal activity rejuvenating navigational learning strategies and contextual memory throughout life. *Nature Communications*, *11*(1), 1–12. https://doi.org/10.1038/s41467-019-14026-z

Bonaguidi, M. A., Wheeler, M. A., Shapiro, J. S., Stadel, R. P., Sun, G. J., Ming, G. L., & Song, H. (2011). In vivo clonal analysis reveals self-renewing and multipotent adult neural stem cell characteristics. *Cell*, *145*(7), 1142–1155. https://doi.org/10.1016/j.cell.2011.05.024

Bond, A. M., Ming, G. L., & Song, H. (2015). Adult mammalian neural stem cells and neurogenesis: Five decades later. *Cell Stem Cell*, *17*(4), 385–395. https://doi.org/10.1016/j.stem.2015.09.003

Cristofano, A. D., Pesce, B., Cordon-Cardo, C., & Pandolfi, P. P. (1998). Pten is essential for embryonic development and tumour suppression. *Nature Genetics*, *19*(4), 348–355. https://doi.org/10.1038/1235

Dhaliwal, N., Choi, W. W. Y., Muffat, J., & Li, Y. (2021). Modeling PTEN overexpression-induced microcephaly in human brain organoids. *Molecular Brain*, *14*(1), 131. https://doi.org/10.1186/s13041-021-00841-3

Drapeau, E., & Abrous, D. N. (2008). Stem cell review series: Role of neurogenesis in age-related memory disorders. *Aging Cell*, *7*(4), 569–589. https://doi.org/10.1111/j.1474-9726.2008.00369.x

Gregorian, C., Nakashima, J., Le Belle, J., Ohab, J., Kim, R., Liu, A., Smith, K. B., Groszer, M., Garcia, A. D., Sofroniew, M. V., Carmichael, S. T., Kornblum, H. I., Liu, X., & Wu, H. (2009). Pten deletion in adult neural stem/progenitor cells enhances constitutive neurogenesis. *The Journal of Neuroscience*, *29*(6), 1874–1886. https://doi.org/10.1523/JNEUROSCI.3095-08.2009

Groszer, M., Erickson, R., Scripture-Adams, D. D., Dougherty, J. D., Le Belle, J., Zack, J. A., Geschwind, D. H., Liu, X., Kornblum, H. I., & Wu, H. (2006). PTEN negatively regulates neural stem cell self-renewal by modulating G0-G1 cell cycle entry. *Proceedings of the National Academy of Sciences of the United States of America*, *103*(1), 111–116. https://doi.org/10.1073/pnas.0509939103

Groszer, M., Erickson, R., Scripture-Adams, D. D., Lesche, R., Trumpp, A., Zack, J. A., Kornblum, H. I., Liu, X., & Wu, H. (2001). Negative regulation of neural stem/progenitor cell proliferation by the Pten tumor suppressor gene in vivo. *Science*, *294*(5549), 2186–2189. https://doi.org/10.1126/science.1065518

He, X. C., Yin, T., Grindley, J. C., Tian, Q., Sato, T., Tao, W. A., Dirisina, R., Porter-Westpfahl, K. S., Hembree, M., Johnson, T., Wiedemann, L. M., Barrett, T. A., Hood, L., Wu, H., & Li, L. H. (2007). PTEN-deficient intestinal stem cells initiate intestinal polyposis. *Nature Genetics*, *39*(2), 189–198. https://doi.org/10.1038/ng1928

Johnston, S., Parylak, S. L., Kim, S., Mac, N., Lim, C., Gallina, I., Bloyd, C., Newberry, A., Saavedra, C. D., Novak, O., Gonçalves, J. T., Gage, F. H., & Shtrahman, M. (2021). AAV ablates neurogenesis in the adult murine hippocampus. *eLife*, *10*, e59291. https://doi.org/10.7554/eLife.59291

Kempermann, G., Gage, F. H., Aigner, L., Song, H., Curtis, M. A., Thuret, S., Kuhn, H. G., Jessberger, S., Frankland, P. W., Cameron, H. A., Gould, E., Hen, R., Abrous, D. N., Toni, N., Schinder, A. F., Zhao, X., Lucassen, P. J., & Frisén, J. (2018). Human adult neurogenesis: Evidence and remaining questions. *Cell Stem Cell*, *23*(1), 25–30. https://doi.org/10.1016/j.stem.2018.04.004

Kim, C., Jadhav, R. R., Gustafson, C. E., Smithey, M. J., Hirsch, A. J., Uhrlaub, J. L., Hildebrand, W. H., Nikolich-Žugich, J., Weyand, C. M., & Goronzy, J. J. (2019). Defects in antiviral T cell responses inflicted by Aging-associated miR-181a deficiency. *Cell Reports*, *29*(8), 2202–2216. https://doi.org/10.1016/j.celrep.2019.10.044

Kuhn, H. G., Dickinson-Anson, H., & Gage, F. H. (1996). Neurogenesis in the dentate gyrus of the adult rat: Age-related decrease of neuronal progenitor proliferation. *The Journal of Neuroscience*, *16*(6), 2027–2033. https://doi.org/10.1523/JNEUROSCI.16-06-02027.1996

Li, H. S., Wang, D., Shen, Q., Schonemann, M. D., Gorski, J. A., Jones, K. R., Temple, S., Jan, L. Y., & Jan, Y. N. (2003). Inactivation of numb and Numblike in embryonic dorsal forebrain impairs neurogenesis and disrupts cortical morphogenesis. *Neuron*, *40*(6), 1105–1118. https://doi.org/10.1016/S0896-6273(03)00755-4

Liu, C., Teng, Z. Q., McQuate, A. L., Jobe, E. M., Christ, C. C., von Hoyningen-Huene, S. J., Reyes, M. D., Polich, E. D., Xing, Y., Li, Y., Guo, W., & Zhao, X. (2013). An epigenetic feedback regulatory loop involving microRNA-195 and MBD1 governs neural stem cell differentiation. *PLoS One*, *8*(1), e51436. https://doi.org/10.1371/journal.pone.0051436

Liu, C., Teng, Z. Q., Santistevan, N. J., Szulwach, K. E., Guo, W., Jin, P., & Zhao, X. (2010). Epigenetic regulation of miR-184 by MBD1 governs neural stem cell proliferation and differentiation. *Cell Stem Cell*, *6*(5), 433–444. https://doi.org/10.1016/j.stem.2010.02.017

Lopez-Ramirez, M. A., & Nicoli, S. (2014). Role of miRNAs and epigenetics in neural stem cell fate determination. *Epigenetics*, *9*(1), 90–100. https://doi.org/10.4161/epi.27536

Lu, S. Y., Fu, C. L., Liang, L., Yang, B., Shen, W., Wang, Q. W., Chen, Y., Chen, Y. F., Liu, Y. N., Zhu, L., Zhao, J., Shi, W., Mi, S., & Yao, J. (2021). miR-218-2 regulates cognitive functions in the hippocampus through complement component 3–dependent modulation of synaptic vesicle release. *Proceedings of the National Academy of Sciences of the United States of America*, *118*(14), e2021770118. https://doi.org/10.1073/pnas.2021770118

Lu, J., Li, S., Li, X., Zhao, W., Duan, X., Gu, X., Xu, J., Yu, B., Sigal, L. J., Dong, Z., Xie, L., & Fang, M. (2021). Declined miR-181a-5p expression is associated with impaired natural killer cell development and function with aging. *Aging Cell*, *20*(5), e13353. https://doi.org/10.1111/acel.13353

Ma, D. K., Bonaguidi, M. A., Ming, G. L., & Song, H. (2009). Adult neural stem cells in the mammalian central nervous system. *Cell Res*, *19*(6), 672–682. https://doi.org/10.1038/cr.2009.56

Moreno-Jiménez, E. P., Flor-García, M., Terreros-Roncal, J., Rábano, A., Cafini, F., Pallas-Bazarra, N., Ávila, J., & Llorens-Martín, M. (2019). Adult hippocampal neurogenesis is abundant in neurologically healthy subjects and drops sharply in patients with Alzheimer's disease. *Nature Medicine*, *25*(4), 554–560. https://doi.org/10.1038/s41591-019-0375-9

Murai, K., Sun, G., Ye, P., Tian, E., Yang, S., Cui, Q., Sun, G., Trinh, D., Sun, O., Hong, T., Wen, Z., Kalkum, M., Riggs, A. D., Song, H., Ming, G. L., & Shi, Y. (2016). The TLX-miR-219 cascade regulates neural stem cell proliferation in neurodevelopment and schizophrenia iPSC model. *Nature Communications*, *7*, 10965. https://doi.org/10.1038/ncomms10965

Navarro Negredo, P., Yeo, R. W., & Brunet, A. (2020). Aging and rejuvenation of neural stem cells and their niches. *Cell Stem Cell*, *27*(2), 202–223. https://doi.org/10.1016/j.stem.2020.07.002

Oliveira, D., Leal, G. F., Sertié, A. L., Caires, L. C., Jr., Goulart, E., Musso, C. M., de Oliveira, J. R. M., Krepischi, A. C. V., Vianna-Morgante, A. M., & Zatz, M. (2019). 10q23.31 microduplication encompassing PTEN decreases mTOR signalling activity and is associated with autosomal dominant primary microcephaly. *Journal of Medical Genetics*, *56*(8), 543–547. https://doi.org/10.1136/jmedgenet-2018-105471

Qiao, J., Zhao, J., Chang, S., Sun, Q., Liu, N., Dong, J., Chen, Y., Yang, D., Ye, D., Liu, X., Yu, Y., Chen, W., Zhu, S., Wang, G., Jia, W., Xi, J., & Kang, J. (2020). MicroRNA-153 improves the neurogenesis of neural stem cells and enhances the cognitive ability of aged mice through the notch signaling pathway. *Cell Death & Differentiation*, *27*(2), 808–825. https://doi.org/10.1038/s41418-019-0388-4

Sasaki, K., Geribaldi-Doldan, N., Szele, F. G., & Isoda, H. (2021). Grape skin extract modulates neuronal stem cell proliferation and improves spatial learning in senescence-accelerated prone 8 mice. *Aging (Albany NY)*, *13*(14), 18131–18149. https://doi.org/10.18632/aging.203373

Soriano-Arroquia, A., House, L., Tregilgas, L., Canty-Laird, E., & Goljanek-Whysall, K. (2016). The functional consequences of age-related changes in microRNA expression in skeletal muscle. *Biogerontology*, *17*, 641–654. https://doi.org/10.1007/s10522-016-9638-8

Sorrells, S. F., Paredes, M. F., Cebrian-Silla, A., Sandoval, K., Qi, D., Kelley, K. W., James, D., Mayer, S., Chang, J., Auguste, K. I., Chang, E. F., Gutierrez, A. J., Kriegstein, A. R., Mathern, G. W., Oldham, M. C., Huang, E. J., Garcia-Verdugo, J. M., Yang, Z., & Alvarez-Buylla, A. (2018). Human hippocampal neurogenesis drops sharply in children to undetectable levels in adults. *Nature*, *555*(7696), 377–381. https://doi.org/10.1038/nature25975

Temple, S. (1989). Division and differentiation of isolated CNS blast cells in microculture. *Nature*, *340*(6233), 471–473.

Tzatsos, A., & Bardeesy, N. (2008). Ink4a/Arf regulation by let-7b and Hmga2: A genetic pathway governing stem cell aging. *Cell Stem Cell*, *3*(5), 469–470. https://doi.org/10.1016/j.stem.2008.10.008

Walgrave, H., Balusu, S., Snoeck, S., Eynden, E. V., Craessaerts, K., Thrupp, N., Wolfs, L., Horré, K., Fourne, Y., Ronisz, A., Silajdžić, E., Penning, A., Tosoni, G., Callaerts-Vegh, Z., D'Hooge, R., Thal, D. R., Zetterberg, H., Thuret, S., Fiers, M., … Salta, E. (2021). Restoring miR-132 expression rescues adult hippocampal neurogenesis and memory deficits in Alzheimer's disease. *Cell Stem Cell*, *28*(10), 1805–1821. https://doi.org/10.1016/j.stem.2021.05.001

Wang, Y., Li, Y., Yue, M., Wang, J., Kumar, S., Wechsler-Reya, R. J., Zhang, Z., Ogawa, Y., Kellis, M., Duester, G., & Zhao, J. C. (2018). N^6-methyladenosine RNA modification regulates embryonic neural stem cell self-renewal through histone modifications. *Nature Neuroscience*, *21*(2), 195–206. https://doi.org/10.1038/s41593-017-0057-1

Wu, Q., Yuan, X., Bai, J., Han, R., Li, Z., Zhang, H., & Xiu, R. (2019). MicroRNA-181a protects against pericyte apoptosis via directly targeting FOXO1: Implication for ameliorated cognitive deficits in APP/PS1 mice. *Aging (Albany NY)*, *11*(16), 6120–6133. https://doi.org/10.18632/aging.102171

Zhang, R., Boareto, M., Engler, A., Louvi, A., Giachino, C., Iber, D., & Taylor, V. (2019). Id4 downstream of Notch2 maintains neural stem cell quiescence in the adult hippocampus. *Cell Reports*, *28*(6), 1485–1498. https://doi.org/10.1016/j.celrep.2019.07.014

Zhang, Q., Liu, H., McGee, J., Walsh, E. J., Soukup, G. A., & He, D. Z. (2013). Identifying microRNAs involved in degeneration of the organ of corti during age-related hearing loss. *PLoS One*, *8*(4), e62786. https://doi.org/10.1371/journal.pone.0062786

Zhao, X., Ueba, T., Christie, B. R., Barkho, B., McConnell, M. J., Nakashima, K., Lein, E. S., Eadie, B. D., Willhoite, A. R., Muotri, A. R., Summers, R. G., Chun, J., Lee, K. F., & Gage, F. H. (2003). Mice lacking methyl-CpG binding protein 1 have deficits in adult neurogenesis and hippocampal function. *Proceedings of the National Academy of Sciences of the United States of America*, *100*(11), 6777–6782. https://doi.org/10.1073/pnas.1131928100

Zhou, Y., Bond, A. M., Shade, J. E., Zhu, Y., Davis, C. O., Wang, X., Su, Y., Yoon, K. J., Phan, A. T., Chen, W. J., Oh, J. H., Marsh-Armstrong, N., Atabai, K., Ming, G. L., & Song, H. (2018). Autocrine Mfge8 signaling prevents developmental exhaustion of the adult neural stem cell Pool. *Cell Stem Cell*, *23*(3), 444–452. https://doi.org/10.1016/j.stem.2018.08.005

SUPPORTING INFORMATION

Additional supporting information can be found online in the Supporting Information section at the end of this article.